Structure and dynamics of fluids in quenched-random potential energy landscapes

Thomas Koincks

Numéro National de Thèse : 2017LYSEN076

THÈSE DE DOCTORAT DE L'UNIVERSITÉ DE LYON

opérée au sein de

L'École Normale Supérieure de Lyon

École Doctorale N° 206

École Doctorale Chimie (Chimie, Procédés, Environnement)

Spécialité de doctorat : Chimie

Soutenue publiquement le 10/11/2017, par :

Thomas Konincks

Structure and dynamics of fluids in quenched-random potential energy landscapes

Structure et dynamique de fluides dans des paysages d'énergie potentielle désordonnés

---

Devant le jury composé de :

Saïd Amokrane	Professeur des universités, Université Paris-Est Val de Marne	Rapporteur
Daniele Coslovich	Maître de conférences, Université de Montpellier	Rapporteur
Thierry Biben	Professeur des universités, Université Lyon 1	Examinateur
Marie Jardat	Professeure des universités, Université Pierre et Marie Curie	Examinatrice
Vincent Krakoviack	Maître de conférences, ENS de Lyon	Directeur de thèse

Remerciements

Pour m'avoir aidé et guidé durant la réalisation de ce long travail, je remercie Vincent Krakoviack. Il m'a appris la rigueur et le souci du détail. Si la thèse est le travail du doctorant, le doctorant est le travail du directeur de thèse. Une grande partie de ce travail n'aurait également pas pu être réalisé sans le dévouement de Christian Melkonian, Loïs Tautelle et d'Emmanuel Quemener, qui ont su dompter le PSMN dans ses moments les plus capricieux, merci à eux. Je me dois aussi de remercier le PSMN lui-même, qui a tant réfléchi à ma place, cette thèse est aussi la sienne. Je remercie le laboratoire de Chimie Théorique qui m'a accueilli pendant les trois ans de ma thèse, et des quelques mois d'un précédent stage. Merci donc à Chantal Andraud, Carine Michel et Vincent Krakoviack encore une fois, et à tout le laboratoire, que je ne peux pas citer entièrement. Je remercie également Jörg Bewerunge et Stefan Egelhaaf, qui grâce aux longs échanges que nous avons eu, m'ont fait appréhender la réalité de mon sujet d'étude.

Merci à Kévin et à Paul, mes amis les plus chers. Merci à Riccardo, Anna et Juan, qui partagent mon parcours et beaucoup de mes souvenirs. Merci Yohann, Orianne, Olivier, Thomas et Jessica, pour les moments passés que je n'oublierai pas, et pour toutes les pizzas avalées ensemble. Merci à Manue, Mathilde, Alex, Chris et Kévin pour avoir égayé ma vie, ma thèse c'est aussi eux. Merci aussi à Yoann, Landry, Mickaël, que je vois moins souvent mais sans qui le tableau ne serait pas complet. Merci à Théo, Ulysse, Léa, Jean-Loup, Sonia, Marylou, Manon, Rémi, Romain, et tous les membres de DéMesures pour m'avoir appris la vulgarisation, et pour tous les bons moments. Merci à Karima, Denis et tous les membres de Pint of Science, pour la super expérience et les centaines de yeux émerveillés. Merci à Nyunyi, Pötyi, Müesli, Bukowski et Howard, pour leur douceur, et leur ingénue amitié. Et merci finalement à Manon, pour sa gentillesse, sa compréhension, son humour et son amour, elle est une belle conclusion.

Je dédie cette thèse à ma famille. Mes parents, Peter et Zita, mon frère Miki et ma soeur Évi. Rien de ce que je pourrais écrire ici ne saurait exprimer ce que ressent. Simplement, merci pour tout.

Il n'y a de frontières que dans les yeux des hommes.

La raison est un dieu jaloux.

Souvent, m'éveillant de mon corps à moi-même, devenu alors extérieur à tout le reste et intérieur à moi-même, contemplant alors une beauté merveilleuse, sûr alors d'appartenir au plus haut point au monde supérieur, ayant vécu la vie la plus noble, étant devenu identique au divin, m'étant fixé en lui, étant parvenu à cette activité suprême, et m'étant établi au dessus de toute autre activité spirituelle. Quand, après ce repos dans le divin, je retombe de l'Intellect au raisonnement, je me demande comment j'ai pu jamais, et cette fois encore, descendre ainsi. Comment mon âme a pu jamais venir à l'inérieur d'un corps, si déjà, lorqu'elle est dans un corps, elle est telle qu'elle m'est apparue.

Plotin, Ennéades, traité 6 (IV,8) Sur la descente de l'âme vers les corps, (traduction de Pierre Hadot)

Contents

Chapter 1

Introduction

The topic of dynamics in the presence of quenched randomness is one of long-standing interest in the field of nonequilibrium statistical mechanics, as demonstrated by a number of extensive and monumental reviews (Havlin and Ben-Avraham, 1987; Bouchaud and Georges, 1990; Dean *et al.*, 2007; Höfling and Franosch, 2013). The reason is obvious: disorder is present and unavoidable in many systems of practical interest, such as natural or synthetic porous solids (Gelb *et al.*, 1999; Alcoutlabi and McKenna, 2005; Alba-Simionesco *et al.*, 2006; Havlin and Ben-Avraham, 1987). In these instances, however, the nature and strength of the disorder is not easily controlled, so that the development of systematic studies is seriously impeded. Recently, a novel class of experimental systems has been put forward, which is based on the interaction of colloids with light and clears up many of these difficulties. It provided the motivation for the present work.

1.1 Experimental studies of colloids in random light fields

At the core of the present work lies an experimental concern, well summarized by Evers *et al.* (2013a). In the studies described in this paper, a complex system of mirrors, filters and lenses has been used to generate, control and measure the properties of a random coherent light pattern, also called a *laser speckle pattern*. In practice, this patern can be realized in many different ways: as a linear superposition of random sinusoidal waves, Kraichnan (1976) as a sum of interactions with randomly placed impurities, Lifshits *et al.* (1988) or through coarse-graining of a random field, not necessarily Gaussian in nature, over large enough regions Chudnovsky and Dickman (1998). The latter scheme is directly relevant to polarizable colloids in speckle patterns, which is the case to be treated here (Hanes *et al.*, 2012; Hanes and Egelhaaf, 2012; Evers *et al.*, 2013b; Hanes *et al.*, 2013; Bewerunge and Egelhaaf, 2016; Bewerunge *et al.*, 2016a,b).

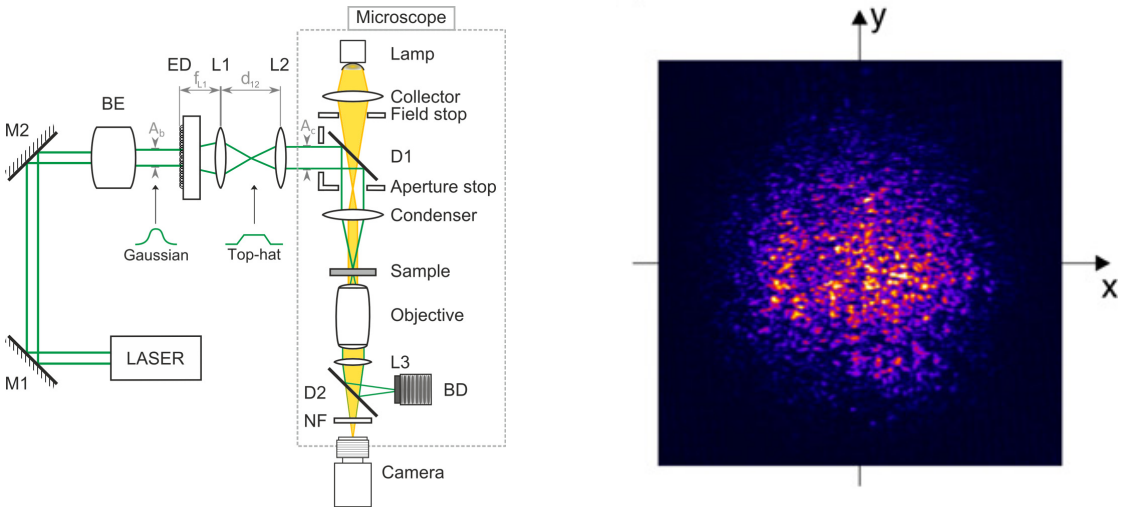

Figure 1.1: Schematic representation of the setup used to create a speckle pattern. **(left)** A laser beam is shone through a diffusive plate and the resulting speckle pattern is then imaged. Reproduced from Bewerunge and Egelhaaf (2016). **(right)** Intensity distribution of a typical speckle pattern recorded with a CCD camera. Reproduced from Fallani *et al.* (2008).

Figure 1.1 schematically shows a way of producing such a light pattern using coarse-graining of a random field, and a visual representation of an actual speckle.

A laser speckle typically consists of light spots randomly dispatched on a surface and can be easily obtained by beaming coherent light on or through a rough surface. Controlling and measuring it however requires a much more complex setup, as explained by Evers *et al.* (2013a). The aim of the experimental work however is not the study of the speckle pattern in itself, but rather its effect on a fluid of Brownian particles, which can interact with light under certain conditions. In this context, the nature of the particles is important, because it conditions the nature of their interactions with the speckle pattern. The particles were chosen to be surfactant-free sulfonated polystyrene spheres, and were plunged in a heavy water solution, before being beamed with the said speckle. Due to their composition, the particles have a higher refractive index compared to the solvent. Furthermore, they are surrounded by solvent molecules, which allows them to experience Brownian motion. These two facts lead us to consider the two different forces felt by the particles and coming from the laser speckle, as shown in figure 1.2.

The first force is the radiative pressure force, that particles with a refractive index higher than that of their solvent may experience in the presence of a light beam. This force has the effect of pulling the particles towards the high intensity regions, and keeping them in place, in the same way an optical tweezer would. The second force is related to the immediate environment of the particles: heating of the solvent particles by light

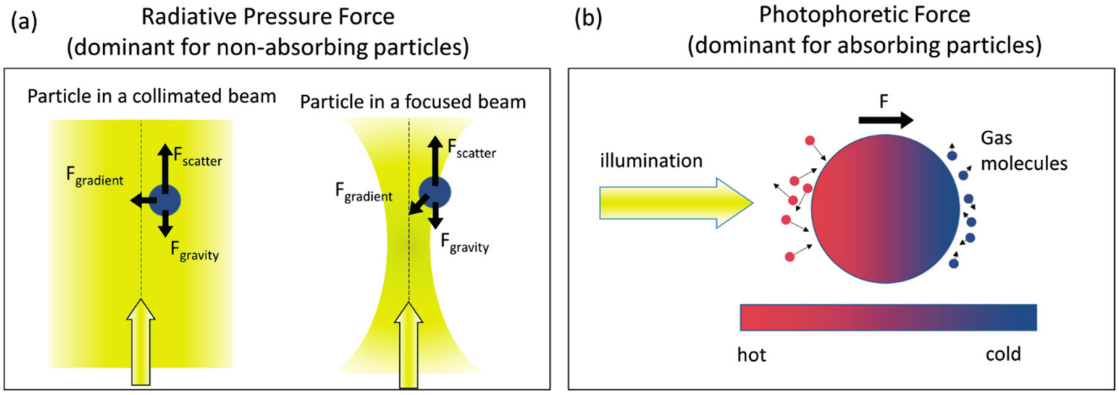

Figure 1.2: Forces exerted by light on a colloidal particle. **(a)** The radiative pressure force, which is the dominant force experienced by non-absorbing particles, results from the transfer of momentum from photons scattered by a particle. The radiative pressure force can be divided into a scattering force, which tends to push the particle along the direction of light propagation, and a gradient force, which tends to pull the particle toward the highest intensity region. The gradient force enables trapping in a focused laser beam. **(b)** The photophoretic force, which is the dominant force experienced by strongly absorbing particles, results from the transfer of heat to surrounding fluid molecules from a non-uniformly heated and/or non-uniformly heat-emitting particle. Reproduced from Redding *et al.* (2015).

absorption creates a pushing force on the illuminated side of the particle. This force has the effect of pushing the particle in the direction of the light beam (Ashkin, 1997; Molloy and Padgett, 2002; Bowman and Padgett, 2013). Therefore, a bunch of particles of a size of the same order of magnitude as the light spots and presenting the properties above mentioned will interact with the speckle, and the latter is to be considered as generating a random energy landscape.

One effect the speckle can have on a fluid of such particles, as studied by Evers *et al.* (2013a), is a dynamical slowing down. Figure 1.3 shows in the left panel a schematic figure taken from the experiments of this group, that presents the dynamics of particles inside a laser speckle in a very intuitive way. In the right panel, a corresponding mean squared displacement (MSD) shows in more details the way dynamics are changing when the power used to generate the laser speckle increases.
Looking at the left panel in figure 1.3, one can already start to imagine some dynamical scenarios. Circled in red is represented the trajectory of what is probably a single particle. That particle seems to spend some time in one limited area in the bottom left of the highlighted zone, before eventually exiting it and wandering around. We can postulate that the particle is first located inside a light spot of the speckle, i.e., a minimum of the potential, before finding a saddle point or reaching enough thermal

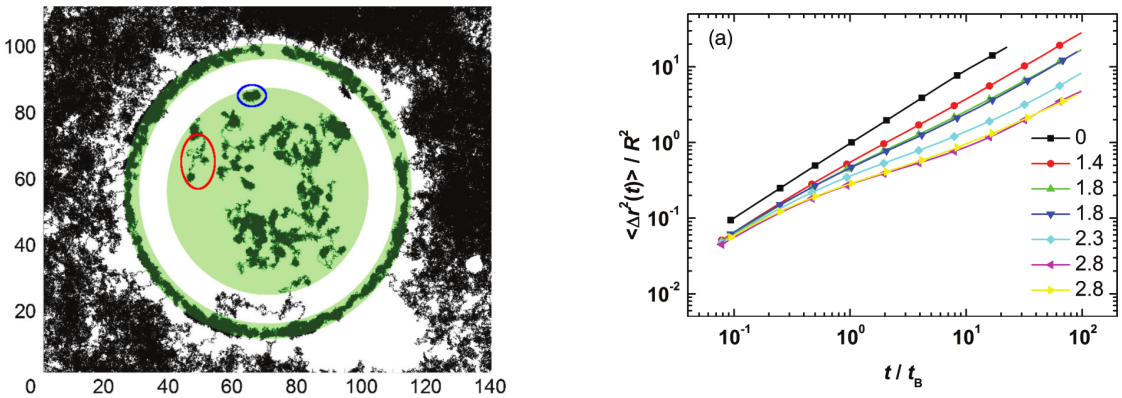

Figure 1.3: Colloidal motion in a speckle pattern. **(left)** Trajectories of particles undergoing diffusion in a two-dimensional plane, part of which contains a random potential (green disk). **(right)** Normalized mean squared displacements. Curves from top to bottom are drawn for increasing laser power. Adapted from Evers *et al.* (2013a).

energy to exit that area, and start to explore more space. A second scenario can be seen highlighted in blue, where one or more particles are spending the whole time of the experiment in one localized area of the experimental setup, which ought to be a very deep minimum those particles cannot get out of. In summary, the laser speckle, by trapping the particles for more or less time, has the property of slowing down the dynamics of the fluid. Furthermore, as it can be seen in the right panel of figure 1.3, the shape of the MSD changes when the laser power is increased. The MSD being a measure of the amount of space explored by the particles, a slope of one for this function means a diffusive motion, and conversely a slope lower than one means a subdiffusive motion. We can see in the right panel that with an increase of the laser power, comes a decrease of the slope of the MSD for intermediate to long times, hinting to an increase of the dynamical slowing down.

A similar scenario can be seen in figure 1.4 by Volpe *et al.* (2014), where a single Brownian particle is allowed to undergo its dynamics in a speckle pattern. From left to right, the power used to generate a same laser speckle is increased. The trajectory of the particle, represented by the green line, shows that at first the dynamics are diffusive in the common sense of the term: the particle undergoes a random walk, almost undisturbed by the presence of the weak speckle. Then, as the intensity of light increases, the particle finds itself more and more constrained to the regions of high intensity, only passing through low intensity regions as crossing saddle points to reach the more stable regions. At high light intensity, the particle is totally localized inside a light spot, unable to cross the high barriers created by the optical potential.

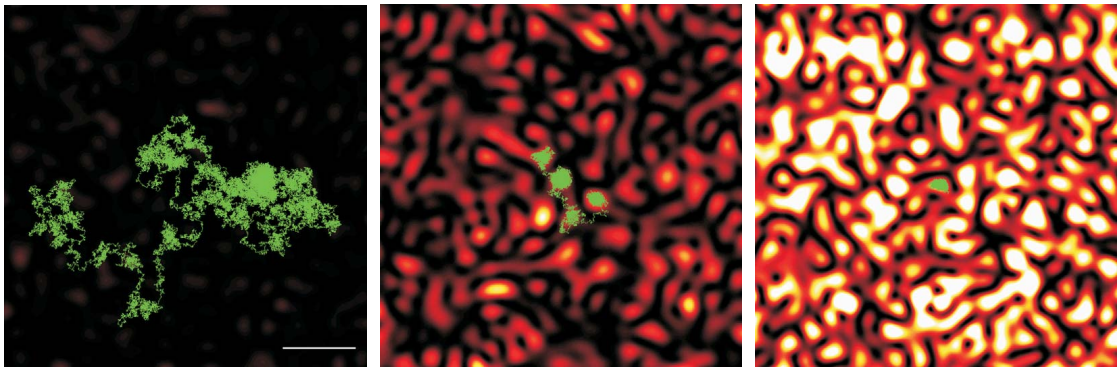

Figure 1.4: Particle diffusion in a speckle pattern. The background represents a speckle pattern generated by a circular aperture. From left to right, the trajectories (green solid lines) show progressive confinement of a polystyrene bead in water as a function of the increasing speckle intensity. Reproduced from Volpe *et al.* (2014).

Another experimental approach comes from Shvedov *et al.* (2010). This experimental setup is at first glance very similar: a laser speckle is generated, and particles are allowed to undergo their dynamics in the optical potential created by that speckle. One difference however is the dimensionality: the experimental setup accounts for a three dimensional laser speckle, and the particles have one more dimension at their disposal as well. This, as it will become obvious a bit later, may be the root of a lot of discrepancies when comparing systems that present different dimensionalities. The goal of the experiment is different in this case as well. While for Evers *et al.* (2013a), the goal is the study of the dynamical slowing down of the particles in the presence of an external disorder, and to analyze the different scenarios responsible for this, the work of Shvedov *et al.* (2010) is aimed as a proof of concept of the ability to trap particles with a laser speckle. Thus, a three-dimensional laser speckle is generated, and carbon nanofoam particles floating freely in air are allowed to interact with it, while being recorded. In figure 1.5 one can see different views of particles being trapped in the random light pattern.
The different pictures in the bottom panels are taken at different times, and it is obvious that the more time passes, the higher the number of particles that are trapped inside the laser speckle. In this experiment, the particles have been shown to remain trapped for more than 24 hours, which is a very long time for Brownian particles. Thus, one can imagine that with enough laser power, particles that exhibit subdiffusive behavior like in the work of Evers *et al.* (2013a), can eventually be trapped *ad infinitum*. The particles trapped in this way are actually experiencing a dynamical arrest due to the presence of the potential.

This is however an uncommon way to induce such a dynamical phenomenon in a colloidal system. A more common way a fluid can experience a dynamical arrest is by an increase

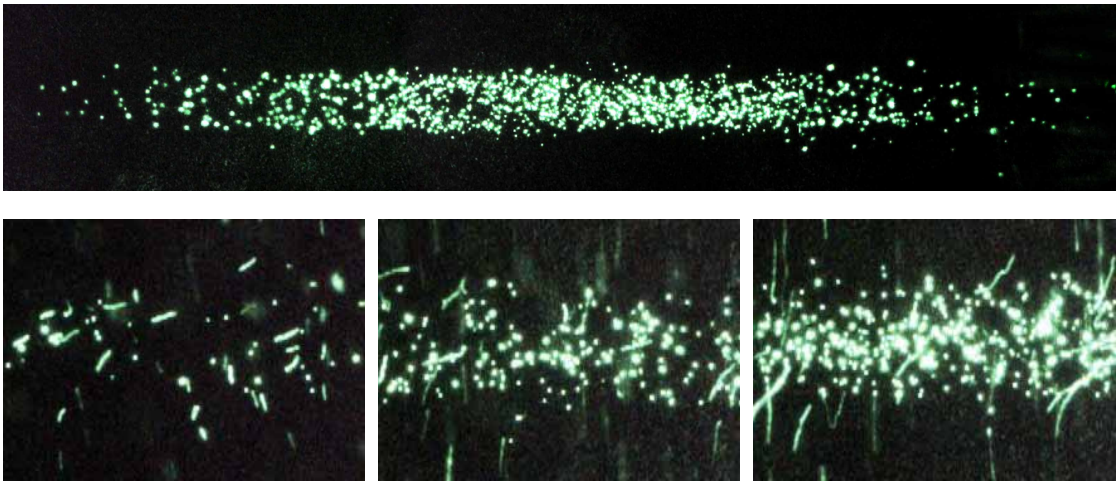

Figure 1.5: Geometry and dynamics of particle trapping in a three-dimensional speckle pattern. **(top)** Image of the laser light scattered from the particles trapped in a speckled bottle beam. **(bottom)** Snapshots showing the progressive filling of the optical trap (time increases from left to right). Reproduced from Shvedov *et al.* (2010).

of its density, leading through overcrowding to the phenomenon called density driven glass transition. In the case of the work of Shvedov *et al.* (2010), the dynamical arrest is driven by the presence of the external potential, leading the fluid, through sub-diffusion phenomena similar to those described by Evers *et al.* (2013a), to a case where the particles are trapped in the energy landscape created by the spots of the laser speckle. Obviously, such a simple scenario is not able to render the full picture of what may happen when the laser power is increased. If more than one particle is present, interplay between density driven and potential driven dynamical slowing down exists and makes the whole problem a lot more complicated.

One possible application of the above-mentioned phenomena is given by Volpe *et al.* (2014). Figure 1.6 shows simulation results of Brownian particles of two species (small and big particles) passing through a speckle-like random potential. The speckle is static in the left panels and ratcheting perpendicular to the flow in the right panels. In both cases, the random potential is used to discriminate the bigger from the smaller particles. These examples have the purpose of convincing the reader that these kinds of systems, though not very well studied yet, have many potential applications. The process of dynamical slowing down through interaction with disorder, until a possible localization or arrest, gives rise to many interesting and probably complex dynamical phenomena that could be exploited if well enough understood.

Concerning the experimental works, two last studies have to be mentionned. The work

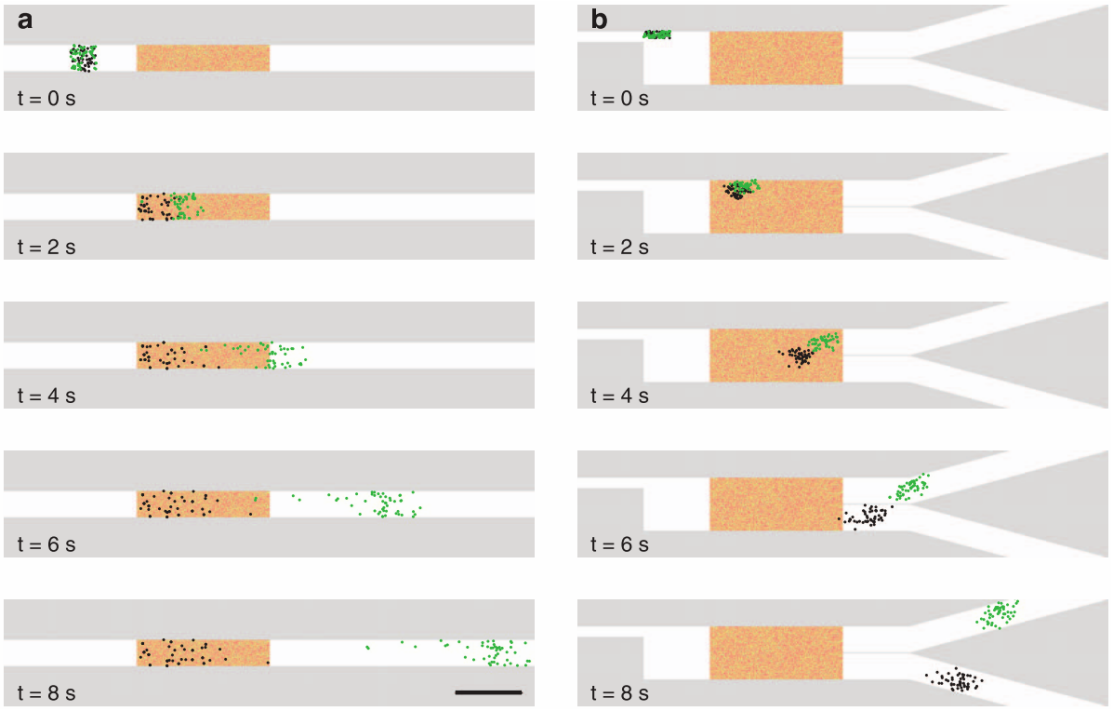

Figure 1.6: Separation of colloidal mixtures with speckle patterns. **(a)** Lapse-time snapshots of the motion of polystyrene particles with small (green dots) and large (black dots) radii in a microfluidic speckle sieve, where a static speckle pattern (shaded area) traps the smaller particles while it lets the larger ones go away with the flow. **(b)** Same as **(a)**, but with the speckle pattern ratcheting in the direction orthogonal to the flow. Reproduced from Volpe *et al.* (2014).

of Pinçe *et al.* (2016) and Paoluzzi *et al.* (2014) cover the dyamics of two-dimensional respectively active particles and run-and-tumble crowds in speckle patterns. These studies aim to understand the behaviour of more natural systems such as bacterias in the smooth biological environment, or the dynamics of human crowds.

1.2 Theoretical studies of tracers in random potential energy landscapes

As much as the experimental setups may be difficult to put together due to practical concerns, this is not the case for theoretical studies, for when computer power is not the problem, only human brain is. Therefore, theoretical studies have been undergone on the subject, starting with the early work of Zallen and Scher (1971) on the percolation transition. In this paper, the authors describe a thought experiment presented as an approximation for a "real (i.e., quantum mechanical) system". In this picture, a random potential $V(\mathbf{r})$ is defined, as well as a density $\phi(E)$ that specifies the fraction of space available to particles of energy E. The system consists of a single particle following Newtonian dynamics, the energy is therefore conserved, meaning that a particle with a strictly lower energy than E will not be able to pass a potential barrier of height E.
To a low value of the energy E of the system corresponds a low value of $\phi(E)$, which means that the space available to the particle is very low, as one can see in the first panel of figure 1.7. In panel (a), indeed, the gray available regions are all separated one from another, and surely, a particle located in one of them will not be able to reach another gray region, being as it is, not able to cross the barriers. This case can be compared to the third picture of figure 1.4, where the particles are isolated in high-intensity spots of light.
On the other hand, panel (c) of figure 1.7 shows a case where $\phi(E)$ has been increased to the point where the particles have an infinite ocean of space available to them, and can therefore diffuse in any direction, which can be compared to the first panel of figure 1.4.
Between these two extremes lies an intermediate state, where the infinite available space just starts forming. This intermediate state happens at a critical energy E_c, corresponding to a density of available space $\phi_c = \phi(E_c)$, and is called the percolation transition.
In two dimensions, as it is the case for example in the experiments of Evers *et al.* (2013a) and Volpe *et al.* (2014), the emergence of the infinite ocean of available space coincides exactly with the vanishing of the infinite ocean of unavailable space. This is a very important point to keep in mind, since this fact changes dramatically with the dimensionality, as can be seen in figure 1.8.
Two things can be readily seen from this figure. First, looking at the $\phi(E)$ curve, the critical volume density decreases dramatically with the dimensionality, which means that the threshold for the existence of an infinite available region is much lower in three

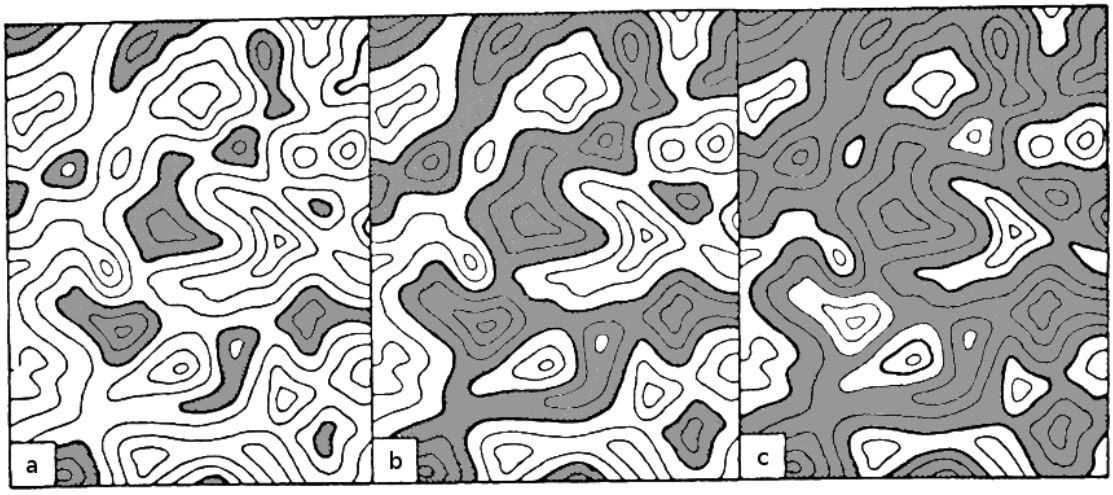

Figure 1.7: Percolation in a two-dimensional potential. The contour lines represent equipotentials of $V(\mathbf{r})$. The gray regions in **(a)**,**(b)** and **(c)** indicate allowed regions ($V(\mathbf{r}) < E$) for three successively increasing values of E. Adapted from Zallen and Scher (1971).

dimensions than in two dimensions (we will not be concerned with the one-dimensional case, which is more a toy system than anything close to a real one).
Second, looking at the $R(E)$ curves, one can clearly see that in the case of a two-dimensional system, the emergence of an infinite available space (the beginning of the full line) exactly coincides with the disappearance of an infinite unavailable space (the end of the dashed line). In the case of a three-dimensional system however, the two curves overlap in one small region of $R(E)$. This means that there is a certain energy span where both the infinite regions of available and unavailable space exist together. One more dimension (and especially one more than two dimensions) allows the system to have two infinite objects existing side to side without interpenetration, by simply avoiding and circumventing each other. Aditionnal theoretical studies about the percolation model can be found in (Ziman, 1968; Isichenko, 1992).

Concerning numerical experiments, we must cite the work of Pezzé *et al.* (2011), who have undertaken a simulation study of the diffusion of Newtonian tracers in an anisotropic disordered two-dimensional potential. In figure 1.9, pictures of the generated potential, with corresponding MSD, are shown for three different available/unavailable space ratios. The MSD have been traced by simulating the diffusion of a single tracer in the disordered environment.
The three pictures and MSD correspond to the same system and the same potential, but with different ratios of available/unavailable space (quantified by the parameter E/V_R). From left to right, this ratio is increasing.

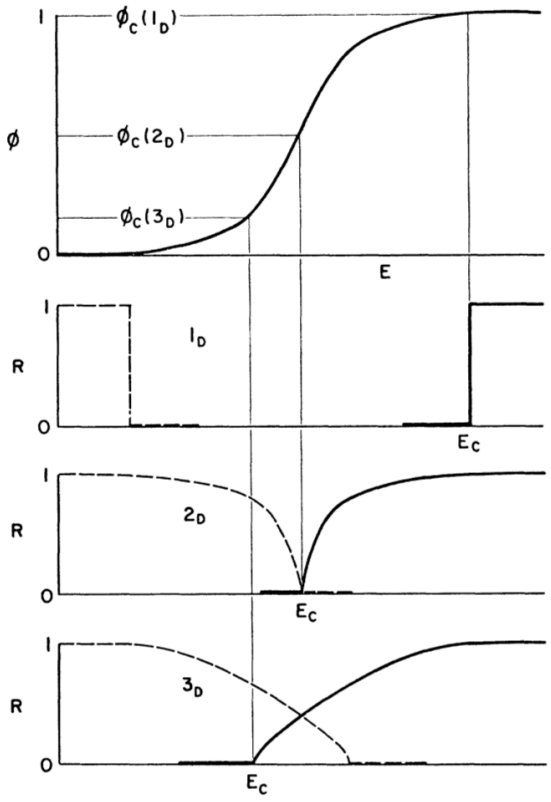

Figure 1.8: Dimensionality dependence of continuum percolation processes. $\phi(E)$ is the fraction of allowed ($V(\mathbf{r}) < E$) space and $R(E)$ is the fraction of space contained in infinitely extended allowed regions. The dashed curves represent functions opposite to $R(E)$, specifying the fraction of space contained in infinitely extended forbidden regions. Reproduced from Zallen and Scher (1971).

For high ratios of available/unavailable space, and at short times, the MSD exhibits what is called a *ballistic regime*, characterized by a slope of the MSD equal to two. This regime occurs when the particle, starting from its initial position, moves but has not yet had the time to experience its immediate surroundings (i.e., the random potential), and is therefore diffusing very rapidly. After some time, the particle starts to experience scattering by the disorder, and the motion slows down to what is called the *diffusive regime*, characterized by a slope of the MSD equal to one. Because the particle has an infinite amount of space available, it does not get stuck in some limited region of space, and therefore the diffusive state lasts for an infinite amount of time.

When the amount of unavailable space increases, the MSD starts to change shape. By looking closely, we can see that, on the middle panel which shows the system closer to the percolation transition, between the initial ballistic regime and the long time diffusive regime, an intermediate regime starts to develop. This regime is characterized by a slope

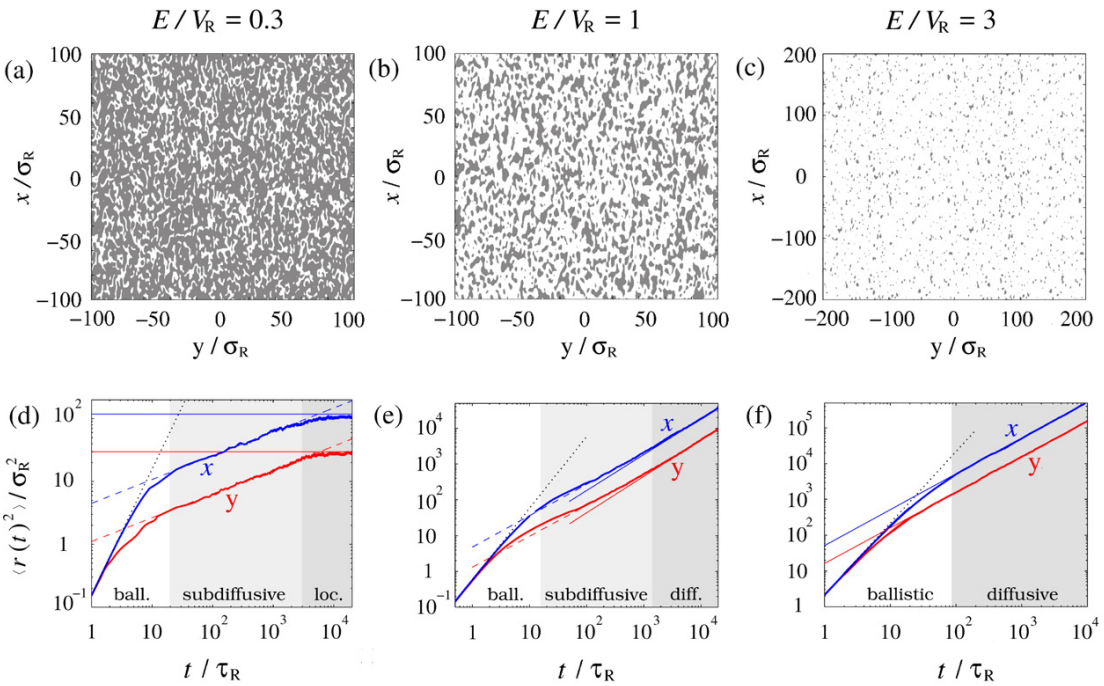

Figure 1.9: Topography and transport regimes of classical particles in a 2D anisotropic speckle potential (anisotropy factor $\sigma_x/\sigma_y = 2$). Panels **(a)**–**(c)** show the allowed (white; $V(\mathbf{r}) < E$) and forbidden (gray; $V(\mathbf{r}) > E$) regions for a classical particle of energy E in the disordered potential $V(\mathbf{r})$. Different columns correspond to the same realization of the disordered potential and different energies. V_R is the average amplitude of the disordered potential. Panels **(d)**–**(f)** show the mean square displacements along the directions x and y (respectively the blue and red lines) as a function of time. Reproduced from Pezzé *et al.* (2011).

of the MSD lower than one, as already seen in figure 1.3, and is called a subdiffusive regime. As the amount of unavailable space increases further, the subdiffusive regime gives rise, at very long times, to another dynamical state of the tracer: the localized state, where the particles, after having explored and experienced collisions with their surroundings, get stuck in some region of space they cannot escape. This state is characterized by a plateau of the MSD at long times.

This very last study can be seen as a confirmation of the percolation model in the case of a system in which the Newtonian model of the dynamics is considered. Furthermore, Yang and Zhao (2010); Skinner *et al.* (2013); Schnyder *et al.* (2015, 2017) show that the percolation model also applies to the case of a fluid that interacts with its potetial with smooth interactions, as it is the cas in the system developped by Evers *et al.* (2013a).

The preceding results were derived considering that the fluid under study follows Newtonian dynamics, i.e., a system whose energy is conserved, leading to the phenomenon called localization, where a particle, or a group of particles are trapped in a localized region of space, due to the fact that they do not have enough energy to climb up the wells created by the potential. However, in the experimental systems discussed above, the natural framework to be used to study the dynamics is the one of the Brownian motion, in which the energy of the system is not conserved. Therefore, in a system like that of Zallen and Scher (1971) but set in a Brownian motion framework, a particle stuck in a localized region of space might eventually be able to escape it, thanks to thermal energy fluctuations due to the bath. This last fact makes the Browian framework much more difficult to tackle, as it generaly requires more sophisticated approaches to understand (De Gennes, 1975; Zwanzig, 1988; De Masi *et al.*, 1989; Chakraborty *et al.*, 1994; Deem and Chandler, 1994; Dean *et al.*, 2007; Touya and Dean, 2007; Dean and Touya, 2008). This mçodel can lead to a great variety of scenarios depending on the dimensionality, and the disorder configuration.

The work of De Masi *et al.* (1989) on the diffusion coefficient sets this last statement in a rigorous way. The main result of this paper is the following :

$$D^{\mathrm{s}}_{\text{1-dim}}(\beta\varepsilon) \leq D^{\mathrm{s}}_{\text{2-dim}}(\beta\varepsilon) \leq \cdots \leq D^{\mathrm{s}}_{(D-1)\text{-dim}}(\beta\varepsilon) \leq D^{\mathrm{s}}_{D\text{-dim}}(\beta\varepsilon) \leq D^{\mathrm{s}}(0), \tag{1.1}$$

where $D^{\mathrm{s}}_{d\text{-dim}}(\beta\epsilon)$ is the diffusion coefficient of a tracer in a d-dimensional disordered potential. $\beta\varepsilon$ is a measure of the amplitude of the random potential relative to the thermal energy $k_BT = \beta^{-1}$, as defined in chapter 2, for instance. It translates experimentally to the power of the laser used to generate the speckle. $D^{\mathrm{s}}(0)$ is the diffusion coefficient of a tracer without the presence of an external disordered potential and is invariant with respect to the dimensionality of the system. Equation 1.1 states that the diffusion coefficient of a tracer only goes up with the dimensionality, and that there is an upper limit to that parameter, which is the value for an undisturbed system.

Another result, discussed in the review of Dean *et al.* (2007), is to be combined with this one to gain crucial insight. It consists of analytic expressions for the diffusion coefficients of tracers in Gaussian random potentials in one and two dimensions:

$$D^{\mathrm{s}}_{\text{1-dim}}(\beta\varepsilon) = D^{\mathrm{s}}(0)e^{-(\beta\varepsilon)^2}, \qquad D^{\mathrm{s}}_{\text{2-dim}}(\beta\varepsilon) = D^{\mathrm{s}}(0)e^{-(\beta\varepsilon)^2/2}. \tag{1.2}$$

With these results, equation (1.1) not only gives an upper bound $[D^{\mathrm{s}}(0)]$ to the diffusion coefficient, but also a lower bound with the term $D^{\mathrm{s}}_{\text{1-dim}}(\beta\varepsilon)$ as defined in equation (1.2). Therefore, due to the inequalities of equation (1.1), $D^{\mathrm{s}}_{d\text{-dim}}(\beta\epsilon)$ is always strictly positive for a system following Brownian dynamics in a Gaussian random potential, which means that a localization of the particles as discussed before cannot exist in this framework.

However, as one will see in chapter 5, not only a localization transition is to be found using the mode-coupling theory (MCT), but a liquid-glass transition also occurs at higher amplitudes of the potential. When the system is in a glass state, the particles experience a complete dynamical arrest, and this occurs at low densities if the amplitude of the potential is increased higher above the localization transition. The overestimation of the localization is a known issue of the MCT, but the actual existence of the localization and the liquid-glass transition is still to be proved, since it has not yet been observed experimentally. Some hints to the existence of a dynamical arrest can be found, for example in the work of Shvedov *et al.* (2010) mentioned above, where particles can be trapped for more than 24 hours in a three-dimensional laser speckle. However, this study is more a proof of concept than an extensive review of the dynamics, as done by Evers *et al.* (2013a). A more in-depth experimental study of the trapping of particles in a laser speckle would give us the tools to decide whether or not an actual localization or transition exists in nature, despite what the Newtonian and the Brownian theoretical frameworks have to say.

1.3 Description of the model studied in this work

Now that the state of the art in studies of particles in random potentials has been introduced, it is time to detail the specificities of the present work, and present the system in more depth. One novelty of the system we aim to study is that the number of particles constituting the fluid is very large, compared to other theoretical studies where mostly, a single tracer has been considered. These particles having to interact with an optical potential in a very specific way, we ought to define the potential rigorously, as well as the fluid itself.
From the work of Evers *et al.* (2013b), which has been the basis of this work, it is known that the distribution of the light intensity follows a Γ law. However, in that study, a typical particle is larger than the size of a light spot in the speckle. Therefore, the effective potential felt by that particle does not exactly follow that distribution. To get the effective potential, one must convolute the potential over the volume of the particle. The result of such a process is shown in figure 1.10. It can be seen that the effective potential felt by that particle takes the form of a Gaussian-distributed variable. This process, by convoluting the volume of the particle, also removes the extended character of its interaction with light, leaving only a point-wise interaction with a Gaussian random potential. This point of view greatly simplifies the problem, both by giving an easier way to look at it, and by allowing the use of an easy-to-manipulate Gaussian model for the potential. Therefore, this will be the basis of the development of our model.

In order to model the fluid of colloids, we choose a system of N hard spheres whose interactions will only be excluded-volume ones, that effectively prevent the distance between two particles to be less than the sum of their radii. The interaction is thus fully

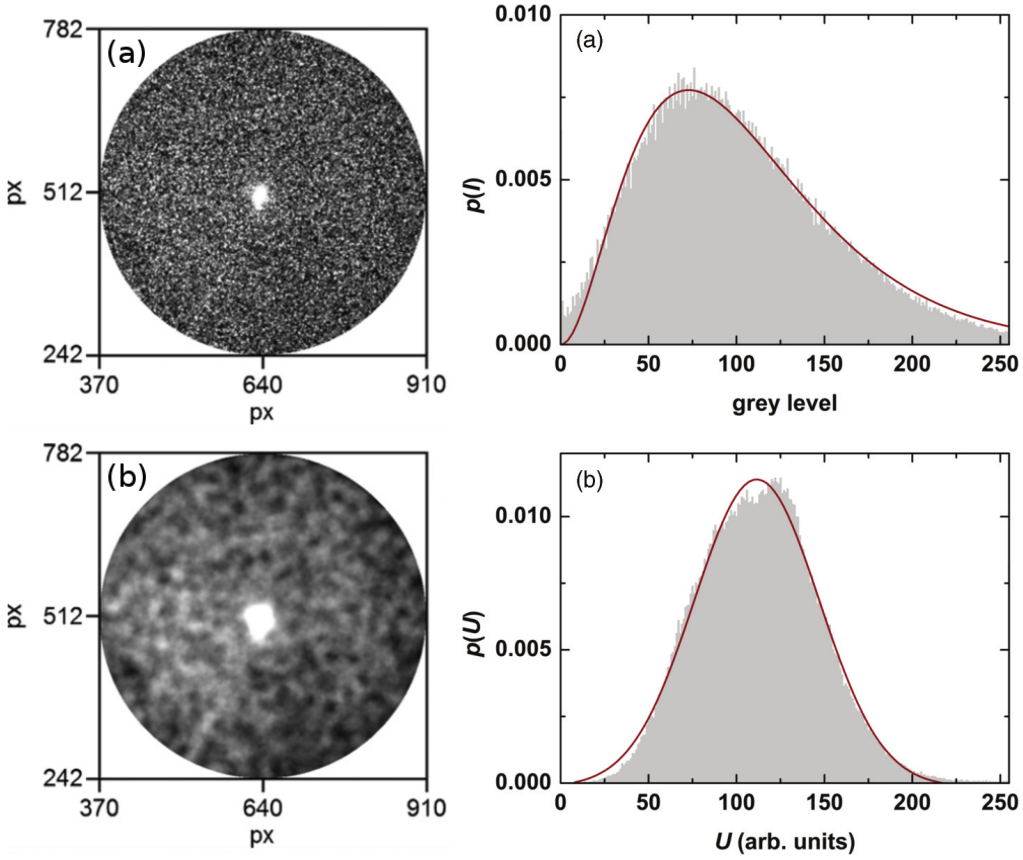

Figure 1.10: Statistics of the random potential in a speckle pattern. **(a)** Micrograph of the observed intensity $I(x, y)$ on a disk taken at very low laser power, and corresponding distribution of values of the intensity of the light field, $p(I)$. **(b)** Potential $U(x, y)$ as experienced by a pointlike test particle obtained by convoluting $I(x, y)$ with the volume of a spherical particle, and distribution of values of the potential as felt by a pointlike test particle, $p(U)$. Full lines are fits based on Γ and Gaussian distributions, respectively. Adapted from Evers *et al.* (2013b).

a hard core one, with no extra potential originating from the particles. The hard spheres are all of the same size, no polydispersity has been introduced in the model.

Furthermore, the interaction of the particle with the potential only takes place at the center of the former, meaning that the only effect the bulk of the particle has is to prevent the approach of another particle at a distance smaller than a diameter. This echoes well with the fact that in the experiments of Evers *et al.* (2013b), the whole system can be thought of as point-like particles interacting with a Gaussian random potential.

One of the most critical parts when modeling this kind of systems is to get a correct

picture of the external potential. Using what has previously been said concerning the effective interaction, we choose to model the speckle-induced potential as a Gaussian random potential. This kind of potential seems the simplest way to model a speckle pattern (Menon and Dasgupta, 1994; Thalmann *et al.*, 2000).

Since this potential is not simply a white noise, a certain correlation function has to be included in order to account for the alternating light and dark spots. For simplicity, this correlation function is chosen to be Gaussian as well. A quick overview of other correlation functions, such as an exponential, a Lorentzian squared, an exponential of a Gaussian minus one, and a hyperbolic secant showed that the difference is not significant as long as the correlation function is smooth, which seems to be the case in the system that we aim to model.

The Hamiltonian of such a system can be written as follows:

$$H[u_{\text{dis}}](\mathbf{r}^N) = \sum_{i=1}^{N-1} \sum_{j=i+1}^{N} w(|\mathbf{r}_i - \mathbf{r}_j|) + \sum_{i=1}^{N} u_{\text{dis}}(\mathbf{r}_i), \tag{1.3}$$

where $w(|\mathbf{r}_i - \mathbf{r}_j|)$ is the pair interaction between two hard spheres i and j, and u_{dis} is a Gaussian random field, i.e., for any integer $k \geq 1$ and positions $\mathbf{x}_1, ..., \mathbf{x}_k$, $u_{\text{dis}}(\mathbf{x}_1), ..., u_{\text{dis}}(\mathbf{x}_k)$ is a collection of k random variables that obey a Gaussian distribution with zero average:

$$\overline{u_{\text{dis}}(\mathbf{x}_i)} = 0, \tag{1.4}$$

where $\overline{\cdots}$ represents the average over disorder. The correlation function of the potential is a Gaussian of the form:

$$\overline{u_{\text{dis}}(\mathbf{x}_i) u_{\text{dis}}(\mathbf{x}_j)} = k(|\mathbf{x}_i - \mathbf{x}_j|), \qquad k(r) = \varepsilon^2 e^{-(r/\sigma)^2}. \tag{1.5}$$

In the latter expression, the two variables ε^2 and σ can be considered as full descriptors of the statistics of the potential. ε gives the amplitude of the fluctuations of the potential, i.e., the typical depth and height of the minima and the maxima. Or to make the link with the precedent experimental work, ε represents the power of the laser used to generate the speckle. σ is the correlation length of the random field, or the typical size of the potential wells in the experimental picture. Two other variables are to be taken into account, that describe the fluid plunged in the disordered potential, i.e., the number density of the fluid ρ, and its temperature T. Taking into account the hard-core diameter of the particules d, we end up with the following set of parameters to fully describe the system:

$$(d, \varepsilon, \sigma, \rho, T). \tag{1.6}$$

We might then define three dimensionless parameters fully characterizing the system,

$$(\rho d^3, \sigma/d, \delta = (\varepsilon/k_B T)^2). \tag{1.7}$$

The formation of the parameter δ reflects some simple physical facts. As ε increases, the depth of the minima of the potential increases, and a particle trapped inside one of them will need more and more energy to escape, or said otherwise: a higher and higher temperature is needed. Therefore, decreasing the temperature has the same effect as increasing the amplitude of the potential. Both cases being tackled by an increase of δ, the use of this parameter in the theory is justified.

This work is presented as follows. Chapter 2 contains developments of quantities and relations needed to calculate the structural properties of simple fluids. The main quantities and theories will be presented, with varying degrees of development. In chapter 3, some major results are presented concerning the structural properties, comprising a quick overview of the effect of different parameters on the density correlations of the fluid. Chapter 4 contains a fully detailed derivation of the Mode Coupling Theory, the theoretical framework used to calculate different dynamical descriptors of the fluid, presented in chapter 5. In that chapter, a "dive into complexity and specificity" of the variables described is made, with the first results concerning phase diagrams, followed by simple dynamical descriptors such as the MSD and the intermediate scattering function (ISF), followed by more specific variables such as the non-Gaussian parameter and the local exponent, and more complex scenarios. Next, an annex-like section, chapter 6, presents the main algorithms and some tricks used during the implementation and the resolution of the relations presented in chapters 2 and 4. Practical details about the size of the variables and the arrays are also given, as keys to fully reproduce the results. Finally, chapter 7 is about a Monte Carlo simulation project that has been undertaken by the end of the PhD work. This chapter is rather short, but has the purpose to outline future developments of the project, that can be looked forward to very soon, since the main tools have already been implemented and validated.

Chapter 2

Structure of simple fluids in randomness: Theory

The structural properties of simple fluids in randomness have an obvious interest of their own. They are also required as input in dynamical studies within the framework of the Mode Coupling Theory, for instance. They are therefore discussed in the present chapter devoted to their general theory, and in the next one reporting actual quantitative results.

2.1 A few words about averages

The beginning of this chapter is dedicated to properly defining the concept of averaging, which allows one to manipulate complex quantities involving many objects in the forms of averages. Let us take the example of a system of particles without external potential at first, to keep the simplicity of the picture. A microstate of such a system is defined as a particular set of positions the particles occupy. Different microstates can be generated by creating different configurations of particles, and in a continuous space, there exists virtually an infinite amount of them. A physical quantity, say, A is usually not defined for a particular microstate, but rather as an average $\langle A \rangle$ of many quantities a_i where i denotes a specific microstate. This allows one to characterize the system in a way that covers the different microstates the system can have. An ensemble average is therefore mathematically expressed as

$$\langle A \rangle = \int A(\mathbf{r}^N)\mathcal{P}(\mathbf{r}^N)d\mathbf{r}^N, \tag{2.1}$$

where $\mathcal{P}(\mathbf{r}^N)$ is the probability density of the realizations, expressed as

$$\mathcal{P}(\mathbf{r}^N) = \frac{e^{-\beta H(\mathbf{r}^N)}}{Z}. \tag{2.2}$$

Z is the partition function of the system :

$$Z = \int e^{-\beta H(\mathbf{r}^N)} d\mathbf{r}^N. \tag{2.3}$$

This concept is closely linked to that of ergodicity, which states that an ergodic process follows the rule

$$\langle A \rangle = \int A(\mathbf{r}^N)\mathcal{P}(\mathbf{r}^N)d\mathbf{r}^N = \lim_{T\to\infty} \frac{1}{T}\int_0^T A(\mathbf{r}^N(t))dt. \tag{2.4}$$

An ergodic process is therefore defined as a process in which the average over an ensemble of static configurations is equivalent to the average over time in a single dynamically evolving system. If we consider ensembles of particular configurations of particles in the system, and we assume that the system evolves with time, i.e., the particles move, if one waits an infinite time, each configuration of the system will be eventually created by the motion of the particles. Therefore, assuming that both the number of microstates and the time tend towards infinity, doing an average over the former is equivalent to doing an average over the latter. This condition is the very one that is ruled out when a system undergoes a liquid-glass transition. A glass phase is characterized by the dynamics of the system being so slow that they reach arrest. In those conditions, iteration of time does not lead to all configurations of the system, and the equality (2.4) does not hold anymore. Thus, a glass transition is often called an ergodicity breaking.

When working with systems that present any kind of frozen disorder, usual statistical mechanical tools are often unusable as such. The reason for this is that the presence of the disorder induces a loss of translational and rotational invariance, leading to a system essentially inhomogeneous after an ensemble average. However, the homogeneity of the system is important to get meaningful quantities, and a new type of averaging has therefore to be introduced in order to restore this condition: the disorder average.

The average over disorder follows a very similar scheme as that of the ensemble average. The difference lies in the fact that the realizations over which the average is made do not concern particle position microstates, but realizations of a given disordered environment. This average, for a certain disorder dependent quantity $A[u_{dis}]$, can be formalized in the following way:

$$\overline{A[u_{dis}]} = \int \mathcal{P}_{\text{dis}}[u_{dis}]A[u_{dis}]d[u_{dis}], \tag{2.5}$$

where $\mathcal{P}_{\text{dis}}[u_{dis}]$ is the probability density of the realizations of the disorder, defined such that

$$\int d[u_{dis}]\mathcal{P}_{\text{dis}}[u_{dis}] = 1. \tag{2.6}$$

From this naturally follows the concept of ergodicity with respect to disorder. Again, this concept is very similar to the usual ergodicity concept, in that it links a configuration

driven equality with a more physical one. The ergodicity with respect to disorder can be written as

$$\overline{A[u_{dis}](\mathbf{r})} = \int \mathcal{P}_{\text{dis}}[u_{dis}]A[u_{dis}](\mathbf{r})d[u_{dis}] = \lim_{V\to\infty}\frac{1}{V}\int_V A[u_{dis}](\mathbf{r})d\mathbf{r}, \tag{2.7}$$

where V is the volume of the system. This relation states that in a system that is ergodic with respect to the disorder, doing an average over different realizations of the disorder and doing an average over the volume of the system leads to the same result. This can be understood by virtually splitting the system in many microsystems over which the average will be done separately. Eventually, if the size of the system tends towards infinity, each realization of the disorder will be found in one of the microsystems, hence equality (2.7).

One can furthermore define the concept of self-averaging quantity. A self-averaging quantity is an additive physical quantity, which can be obtained with a good approximation for the whole system, by calculating it for one of the realizations described above. Furthermore, this quantity has to have short range correlations, that typically do not exceed the size of the microsystems. This statement can be expressed as

$$A = A[u_{dis}] = \overline{A[u_{dis}]} \tag{2.8}$$

and will be an important one for future developments.

Therefore, to be a meaningful observable in a system with quenched disorder, a physical quantity has to be averaged over both the realizations of a same ensemble, and the realizations of a same disorder. The problem that arises with this statement is logically about the priority of the averages: should the average over disorder be done before or after the ensemble average? In other words, should we calculate $\langle\overline{A}\rangle$ or $\overline{\langle A\rangle}$? This question will be tackled in more detail further in this chapter, but an intuitive answer can be formulated already.

In the experimental work of Evers *et al.* (2013a), Bewerunge *et al.* (2016b), and Bewerunge and Egelhaaf (2016), which are the base comparison of the present work, measurements are undertaken in a specific way. A laser speckle is generated and Brownian particles are introduced in the environment. Dynamics and structure are recorded on subpopulations of particles that are chosen so to be separated enough not to interract with each other. In this way, a single potential is sampled almost completely, in a rigorous way, while allowing for reasonable experimental times. A time average allows one, due to the principle of ergodicity, to have an ensemble average valid on one particle potential. Then, a new laser speckle is generated and the process starts over. At the end, all the values are averaged and the result is the desired physical quantity. Therefore, a first idea on what order the averages have to be done can be deduced from it: first the ensemble average, then the disorder average : $\overline{\langle A\rangle}$.

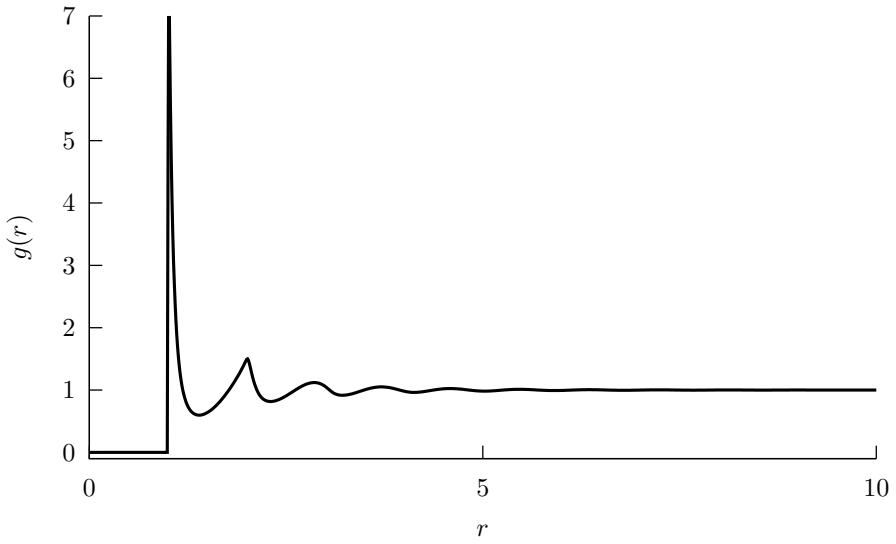

Figure 2.1: Radial distribution function of a system at a high density ($\rho = 1.00$) with the presence of an external Gaussian random potential of relative amplitude $\delta = 2.53$ and Gaussian correlation function of correlation length $\sigma = 0.50$.

2.2 Density correlations and how to calculate them

The structural information on a fluid without the presence of an external potential is mainly contained in the function called the radial distribution function, $g(r_{12})$. This function gives the probability to find a particle labeled 2 at a given distance of a particle labeled 1, normalized by this same probability in an ideal gas, i.e., a fluid without any correlation between the constituting particles. In a crystal, $g(r)$ presents characteristic peaks that mirror the regular disposition of the molecules on the primitive cell. In the case of a liquid, however, which has the essential characteristics of having no order at short nor long range, the radial distribution function presents a damping at long distances, characteristic of the loss of correlations, as one can see on figure 2.1. The function thus naturally tends towards 1 at long distances, where the said probability equals that of an ideal gas.

The radial distribution function is linked to the so-called total correlation function by the following simple relation:

$$h(r_{12}) = g(r_{12}) - 1. \tag{2.9}$$

This subtraction simply allows the manipulation of a function that tends towards zero at long distance, which facilitates many calculations. For simplicity the subscripts will be omitted when possible in the following.

The total correlation function $h(r)$ is furthermore formally defined as

$$h(|\mathbf{r}-\mathbf{r}'|) = \frac{\langle \rho^{(2)}(\mathbf{r},\mathbf{r}')\rangle - \rho^2}{\rho^2}, \tag{2.10}$$

where ρ is the average density, and $\rho^{(2)}(\mathbf{r},\mathbf{r}')$ is the two-point density, and can thetefore be seen as a density correlation function.

Like the radial distribution function, the total correlation function $h(r)$ tends to have a particularly complex shape and cannot in many cases be expressed in simple terms. This is the main problem concerning the characterization of the structure of simple liquids, and even more concerning the characterization of confined simple liquids. The solution starts with rewriting this complex function in simpler terms, which is the point of the Ornstein-Zernike (OZ) relation. This relation states the total correlation function as a chain of correlations that have a supposedly simpler expression. It reads

$$h(r_{12}) = c(r_{12}) + \rho \int c(r_{13})h(r_{32})d\mathbf{r}_3, \tag{2.11}$$

where ρ is the density of the fluid. The OZ equation serves also as a definition of the direct correlation function $c(r_{12})$, in terms of $h(r_{12})$. The second part of the equation (2.11) is a convolution over the position of a particle labeled 3, and has thus the purpose of scanning over all the particles constituting the fluid. A convolution, which is a quite complex operation in real space, can be rewritten in reciprocal space by simply taking its Fourier transform. The advantage of this new form is that a convolution becomes a simple product in reciprocal space,

$$h(\mathbf{q}) = c(\mathbf{q}) + \rho c(\mathbf{q})h(\mathbf{q}), \tag{2.12}$$

which greatly simplifies the calculations.

However, the OZ relation only provides a way of rewriting the total correlation function and to define the direct correlation function accordingly. It provides no new information, and the calculation of $h(r)$ and $c(r)$ cannot be done without the use of another relation linking the two terms. This other relation has to close the set of equations, and is therefore called a closure relation. They come in many flavors and levels of approximation. Those used during this work will be spelled out later on.

The presence of an external disordered potential, as the one studied here, can have a dramatic influence on both the structure and the dynamics of the fluid. However, the usual OZ equation does not take into account the presence of this external potential, and some modifications have to be done in order to get the correct correlation functions. With this in mind, the replica trick developed by Edwards and Anderson (1975) gives a

convenient theoretical framework to include the presence of an external disorder in the structural calculations. This method has had many developments and applications until Menon and Dasgupta (1994) extended it to liquids in presence of an external disorder. It is on this theoretical basis that we will calculate the correlations needed to understand the system.

The replica trick starts with a simple relation :

$$x^s = 1 + s \ln x + O(s^2). \tag{2.13}$$

The knowledge of the canonical partition function allows one to get the corresponding free energy of the system, and thus its whole thermodynamics. The usual relation linking the canonical partition function and the free energy is the following:

$$F = -k_B T \ln Z, \tag{2.14}$$

where Z, presenting no dependence on u_{dis}, is the partition function of the system without external disorder. However, if we include the presence of the external potential, we have to take the average over disorder of the latter expression in order to obtain a meaningful expression of the free energy. At first glance, there are two ways of doing this:

$$F_1 = -k_B T \ln \overline{Z[u_{dis}]}, \tag{2.15}$$

$$F_2 = -k_B T \overline{\ln Z[u_{dis}]}. \tag{2.16}$$

This has quickly been tackled by experimental arguments, but an actual analysis of these two expression can bring further confirmation. Let us first consider the first option, equation (2.15).

We can give the expression for $\overline{Z[u_{dis}]}$:

$$\begin{aligned}\overline{Z[u_{dis}]} &= \int d[u_{dis}] \mathcal{P}_{dis}[u_{dis}] Z[u_{dis}] \\ &= \int d\mathbf{r}^N d[u_{dis}] e^{-\beta(H[u_{dis}](\mathbf{r}^N) - k_B T \ln \mathcal{P}_{dis}[u_{dis}])}.\end{aligned} \tag{2.17}$$

In the last expression of equation (2.17), we notice that u_{dis} is actually taken as a variable, and integrated over in the same way $\mathbf{r}^N$ is. From a mathematical point of vue this means that the potential is taken to be a dynamical potential, which is obviously not the case in the present system. If we go back to the comparison with the experimental work, we could imagine particles undergoing their dynamics in a moving laser speckle. The behavior of this system is expected to be very different from the one we are studying here, whose essential feature is the difference between quenched and annealed degrees of freedom.

Furthermore, thanks to the homogeneity of the external disorder, it is possible to cut the system into many microsystems without losing the properties of this potential. It also happens that the free energy is an additive function whose correlations are short-ranged, effectively classifying it as a self-averaging quantity, as defined above. Due to (2.8), the following statement is true:

$$F = \overline{F[u_{dis}]} = -k_B T \overline{\ln Z[u_{dis}]}, \tag{2.18}$$

which is precisely the second writing proposed in equation (2.16). Hence, this version of the disorder averaged free energy is the one that captures correctly the frozen nature of the potential, while also taking advantage of the fact that the free energy is a self-averaging quantity.

Using expression (2.13), we can write the following :

$$\overline{\ln Z[u_{dis}]} = \lim_{s\to 0} \frac{\ln \overline{Z[u_{dis}]^s}}{s}, \tag{2.19}$$

which we then plug into (2.16) to get

$$F = -k_B T \overline{\ln Z[u_{dis}]} = -k_B T \lim_{s\to 0} \frac{\ln \overline{Z[u_{dis}]^s}}{s}. \tag{2.20}$$

We can detail the expression of $Z[u_{dis}]^s$ to find its actual physical meaning, assuming there is one:

$$Z[u_{dis}]^s = \int \prod_{a=1}^{s} d\mathbf{r}^{N,a} e^{-\beta \sum_{a=1}^{s} H[u_{dis}](\mathbf{r}^{N,a})}. \tag{2.21}$$

The latter expression is that of the partition function of s identical and noninteracting systems, that are copies of the same original one, hence the name of the trick. Taking the disorder average of this partition function is done by

$$\begin{aligned}
\overline{Z[u_{dis}]^s} &= \int d[u_{dis}] \mathcal{P}_{dis}[u_{dis}] Z[u_{dis}]^s \\
&= \int d[u_{dis}] \mathcal{P}_{dis}[u_{dis}] \int \prod_{a=1}^{s} d\mathbf{r}^{N,a} e^{-\beta \sum_{a=1}^{s} H[u_{dis}](\mathbf{r}^{N,a})} \\
&= \int d[u_{dis}] \mathcal{P}_{dis}[u_{dis}] \int \prod_{a=1}^{s} d\mathbf{r}^{N,a} e^{-\beta \sum_{a=1}^{s} [V(\mathbf{r}^{N,a}) + U_{dis}[u_{dis}](\mathbf{r}^{N,a})]} \\
&= \int \prod_{a=1}^{s} d\mathbf{r}^{N,a} e^{-\beta \sum_{a=1}^{s} V(\mathbf{r}^{N,a})} \int d[u_{dis}] \mathcal{P}_{dis}[u_{dis}] e^{-\beta \sum_{a=1}^{s} U_{dis}[u_{dis}](\mathbf{r}^{N,a})} \\
&= \int \prod_{a=1}^{s} d\mathbf{r}^{N,a} e^{-\beta \left[\sum_{a=1}^{s} V(\mathbf{r}^{N,a}) - k_B T \ln \int d[u_{dis}] \mathcal{P}_{dis}[u_{dis}] e^{-\beta \sum_{a=1}^{s} U_{dis}[u_{dis}](\mathbf{r}^{N,a})} \right]} \\
&= \int \prod_{a=1}^{s} d\mathbf{r}^{N,a} e^{-\beta [\sum_{a=1}^{s} V(\mathbf{r}^{N,a}) + W_s^{av}(\mathbf{r}^{N,1}, \ldots, \mathbf{r}^{N,s})]}.
\end{aligned} \tag{2.22}$$

We can define the replicated Hamiltonian as

$$H_s^{rep}(\mathbf{r}^{N,1},\ldots,\mathbf{r}^{N,s}) = \sum_{a=1}^{s} V(\mathbf{r}^{N,a}) + W_s^{av}(\mathbf{r}^{N,1},\ldots,\mathbf{r}^{N,s}). \tag{2.23}$$

One can notice that by averaging out the external potential, the initially independent replicas now have an effective interaction coming from the term $W_s^{av}(\mathbf{r}^{N,1},\ldots,\mathbf{r}^{N,s})$. This effective interaction can be thought to come from the presence of a potential, or rather the fact that it has been averaged out.

In the case of Gaussian disorder, all interactions can be decomposed as sums of pairwise interactions. We get

$$V(\mathbf{r}^N) = \sum_{i=1}^{N-1}\sum_{j=i+1}^{N} w(|\mathbf{r}_i - \mathbf{r}_j|), \tag{2.24}$$

and, for the disordered potential,

$$W_s^{av}(\mathbf{r}^{N,1},\ldots,\mathbf{r}^{N,s}) = -\frac{\beta}{2}\sum_{a,b=1}^{s}\sum_{i,j=1}^{N} k(|\mathbf{r}_{i,a} - \mathbf{r}_{j,b}|), \tag{2.25}$$

where $k(r)$ is the covariance of the Gaussian random potential and has been chosen as a Gaussian function as well:

$$k(r) = \varepsilon^2 e^{-(r/\sigma)^2}. \tag{2.26}$$

Using the above-mentioned expressions, and equation (2.20), the free energy can now be written

$$F = \overline{F[u_{dis}]} = -k_B T \overline{\ln Z[u_{dis}]} = \lim_{s\to 0} \frac{F_s^{\text{rep}}}{s}. \tag{2.27}$$

The calculation of the disorder-averaged free energy sums up to creating s replicas of the initial system, finding a good approximation for the effective Hamiltonian, and taking the limit $s \to 0$ of the number of replicas. This last part involves analytic continuation. It can be highly non-trivial and lead to breaking of the symmetry of the replicas. These subtleties will not be covered here, but one can refer to Menon and Dasgupta (1994) and Mezard *et al.* (1987) for further information.

The latter method can be applied not only to the free energy, but also to a whole other class of dynamical variables. The case that is of particular interest here is that of the correlation functions, which includes $g(r)$, $h(r)$ and $c(r)$ defined above. Following the scheme of equation (2.27), one can write, for a configurational variable denoted by $A(\mathbf{r}^N)$,

$$\begin{aligned}\overline{\langle A(\mathbf{r}^N)\rangle} &= \int d[u_{dis}]\mathcal{P}_{\rm dis}[u_{dis}] \int d\mathbf{r}^N \frac{e^{-\beta H[u_{dis}](\mathbf{r}^N)}}{Z[u_{dis}]} A(\mathbf{r}^N) \\ &= \lim_{s\to 0} \int d[u_{dis}]\mathcal{P}_{\rm dis}[u_{dis}] Z[u_{dis}]^{s-1} \int d\mathbf{r}^N e^{-\beta H[u_{dis}](\mathbf{r}^N)} A(\mathbf{r}^N) \\ &= \lim_{s\to 0} \int \prod_{b=1}^{s} d\mathbf{r}^{N,b} e^{-\beta H_s^{\rm rep}(\mathbf{r}^{N,1},\ldots,\mathbf{r}^{N,s})} A(\mathbf{r}^{N,a}),\end{aligned} \tag{2.28}$$

where the replica symmetry allows the choice of the value of a to be arbitrary. Using that $\lim_{s\to 0} \overline{Z[u_{dis}]^s} = 1$ we get

$$\overline{\langle A(\mathbf{r}^N)\rangle} = \lim_{s\to 0} \int \prod_{b=1}^{s} d\mathbf{r}^{N,b} \frac{e^{-\beta H^{\rm rep}(\mathbf{r}^{N,1},\ldots,\mathbf{r}^{N,s})}}{\overline{Z[u_{dis}]^s}} A(\mathbf{r}^{N,a}), \tag{2.29}$$

and finally we arrive at the replicated form of the average :

$$\overline{\langle A(\mathbf{r}^N)\rangle} = \lim_{s\to 0} \langle A(\mathbf{r}^{N,a})\rangle_s^{\rm rep}. \tag{2.30}$$

One can also define

$$\overline{\langle A(\mathbf{r}^N)B(\mathbf{r}^N)\rangle} = \lim_{s\to 0} \langle A(\mathbf{r}^{N,a})B(\mathbf{r}^{N,a})\rangle_s^{\rm rep}, \tag{2.31}$$

$$\overline{\langle A(\mathbf{r}^N)\rangle\langle B(\mathbf{r}^N)\rangle} = \lim_{s\to 0} \langle A(\mathbf{r}^{N,a})\rangle_s^{\rm rep} \langle B(\mathbf{r}^{N,b})\rangle_s^{\rm rep} \quad , a \neq b, \tag{2.32}$$

where in the first expression the thermal average is to be taken over the product of these variables, leading to the correlations of these two variables taking place in the same replica. The second expression gives the same kind of correlations, except that the thermal average is taken over each variable separately. This translates to having the two variables arising from two different replicas. The power of the replica trick is to give a way from a system with a quenched disorder in which the usual tools of statistical mechanics cannot be put in good use, to s replicated systems interacting indirectly through the presence of the disordered potential, in which variables with a standard physical meaning can be calculated.

Looking at the previous equations, one can notice that, in the case where $A(\mathbf{r}^N) = B(\mathbf{r}^N) = \rho^{(1)}(\mathbf{r})$, we get (omitting a trivial self term)

$$\overline{\langle \rho^{(1)}(\mathbf{r})\rho^{(1)}(\mathbf{r}')\rangle} = \rho^2 g(|\mathbf{r}-\mathbf{r}'|), \tag{2.33}$$

$$\overline{\langle \rho^{(1)}(\mathbf{r})\rangle\langle \rho^{(1)}(\mathbf{r}')\rangle} = \rho^2 g^d(|\mathbf{r}-\mathbf{r}'|). \tag{2.34}$$

The latter development of the replica theory can now help us to express the total correlation function $h(r)$ in the framework of a system with an external disorder, by simply

rewriting it in terms of correlation functions in different replicas. One can write the OZ equations applied to an unconstrained system containing s different species of particles:

$$h_{ab}(r) = c_{ab}(r) + \sum_c \rho_c h_{ac}(r) c_{cb}(r). \tag{2.35}$$

The case of an s component fluid is a general case of the replicated system. The main difference is obviously that the replicated systems are the exact same as the original, and this translates to simple relations in terms of correlation functions:

$$h_{aa}(r) = h_{bb}(r), \tag{2.36}$$
$$c_{aa}(r) = c_{bb}(r). \tag{2.37}$$

In equation (2.35), no restriction is imposed on the values of a and b. One might want to separate the terms which belong to the same species (or replicas in our case) from the terms which describe an inter replica interaction in order to get an OZ equation for the terms described in equations (2.33) and (2.34). The following notation will be used:

$$\begin{aligned} h(r) &= h_{aa}(r), \\ h^d(r) &= h_{ab}(r), \\ c(r) &= c_{aa}(r), \\ c^d(r) &= c_{ab}(r), \end{aligned}$$

where the subscript d means disconnected (a subscript c for connected will appear later). Now, rewriting equation (2.35) to separate the total and the disconnected components, we get:

$$\begin{cases} h_{aa}(r_{12}) = c_{aa}(r_{12}) + \rho \int d\mathbf{r}_3 c_{aa}(r_{13}) h_{aa}(r_{32}) + (s-1)\rho \int d\mathbf{r}_3 c_{ab}(r_{13}) h_{ab}(r_{32}), \\ h_{ab}(r_{12}) = c_{ab}(r_{12}) + \rho \int d\mathbf{r}_3 c_{aa}(r_{13}) h_{ab}(r_{32}) + \rho \int d\mathbf{r}_3 c_{ab}(r_{13}) h_{aa}(r_{32}) \\ \qquad\qquad +(s-2)\rho \int d\mathbf{r}_3 c_{ab}(r_{13}) h_{ab}(r_{32}). \end{cases} \tag{2.38}$$

And finally, taking the $s \to 0$ limit and using the just defined notation, we get the replicated OZ equation for a system with an external disorder:

$$\begin{cases} h(r_{12}) = c(r_{12}) + \rho \int d\mathbf{r}_3 c(r_{13}) h(r_{32}) - \rho \int d\mathbf{r}_3 c^d(r_{13}) h^d(r_{32}), \\ h^d(r_{12}) = c^d(r_{12}) + \rho \int d\mathbf{r}_3 c(r_{13}) h^d(r_{32}) + \rho \int d\mathbf{r}_3 c^d(r_{13}) h(r_{32}) \\ \qquad\qquad -2\rho \int d\mathbf{r}_3 c^d(r_{13}) h^d(r_{32}), \\ h^c(r_{12}) = h(r_{12}) - h^d(r_{12}) = c^c(r_{12}) + \rho \int d\mathbf{r}_3 c^c(r_{13}) h^c(r_{32}). \end{cases} \tag{2.39}$$

The total correlation function is the sum of the connected and disconnected parts, and in order to get a full structural description of the system, both need to be calculated. Furthermore, these two types of correlation functions can be related to a physical reality: the disconnected correlation function brings the correlations between the particles that

mainly go through the external potential, and the total correlation function ($h(r)$) brings *all* the correlations, considering as well those coming through the fluid interactions. Obviously interplay between the density-related and potential-related effects leads to a much more complicated picture. However, considering this simple separation can help a lot in the understanding of the complexity the potential can bring on the structural properties of the fluid.

2.3 Closure relations and how to actually get results out of the OZ equations

As stated above, the OZ relations, which are exact equations expressing the total correlation functions, rather complex quantities, in terms of chains of direct and simpler correlations between all the particles constituting the system, do not give in themselves any more information about the structure than the total correlation functions do. In order to calculate the latter, other relations must be introduced to close the set and calculate the structural properties: the closure relations. The OZ equations themselves include no approximations, but this is not the case for these new relations. In each case, the bulk relations will be derived. The replica trick will then be applied to them, to get the closure relation adapted to the presence of disorder. In that way, the closure relations can be used together with the replicated OZ relations to get the full correlation functions needed to describe our system.

2.3.1 Percus-Yevick

One of the first closure relations to be developed and used extensively in liquid state theory is the Percus-Yevick (PY) relation, developed by Percus and Yevick (1958), hence the name. This relation will be systematically taken as the starting point for the development of the other closure relations hereafter. The derivation of the PY relation starts from the idea that the direct correlation function, $c(r)$ as introduced in the previous chapter, can be simply defined as:

$$c(r) = g_{\text{tot}}(r) - g_{\text{ind}}(r) \tag{2.40}$$

where the terms can be empirically understood as: g_{tot} is the standard radial distribution function that gives the total correlation between two particles, and g_{ind} only takes into account the correlations through the other particles of the system, i.e., the indirect correlations. We can approximately rewrite the latter in the following way:

$$c(r) \approx e^{-\beta w(r)} - e^{-\beta[w(r)-u(r)]} \tag{2.41}$$

where $w(r)$ denotes the potential of mean force and $u(r)$ denotes the pair potential.

The point to raise here is that the actual correlations are not only consisting of direct pairwise interactions, but also contain a lot of more complicated contributions like chains of interactions. Thus, equation (2.41) is to be considered as an approximation.

Further developing and rearranging:

$$c(r) = g_{\text{tot}}(r) - e^{\beta u(r)} g_{\text{tot}}(r) = e^{\beta u(r)} g_{\text{tot}}(r)(e^{-\beta u(r)} - 1), \tag{2.42}$$

leading to

$$e^{-\beta u(r)} c(r) = (1 + h(r))(e^{-\beta u(r)} - 1), \tag{2.43}$$

and eventually

$$c(r) = (1 + h(r) - c(r))(e^{-\beta u(r)} - 1). \tag{2.44}$$

This is the essence of the PY approximation. It is therefore simply a way to relate $c(r)$, $h(r)$, and the pair potential. An iterative numerical solution is now possible, combining the PY and the OZ equations, but, up to now, this only holds for bulk systems. In order to take into account the disorder in the calculation, and use the closure and the replicated OZ relation together, we must apply the replica trick to the closure as well. The route to do this is the exact same as has been done with the OZ relation in the previous section: extend the closure relation to the case of a bulk multicomponent mixture and take the limit of the special case when the different species represent different replicas. For the multicomponent PY closure we get

$$c_{ab}(r) = (1 + h_{ab}(r) - c_{ab}(r))(e^{-\beta u_{ab}(r)} - 1). \tag{2.45}$$

Taking the particular case when the components of the mixture are but replicated versions of the original system, it is possible to distinguish between the intra-replica correlations and the inter-replica correlations,

$$\begin{aligned} c_{aa}(r) &= (h_{aa}(r) - c_{aa}(r) + 1)(e^{u_{aa}(r)} - 1), \\ c_{ab}(r) &= (h_{ab}(r) - c_{ab}(r) + 1)(e^{u_{ab}(r)} - 1). \end{aligned} \tag{2.46}$$

Furthermore, from the form of the effective potential energy, equation (2.25), one gets an effective pair interaction as

$$\begin{aligned} u_{aa}(r) &= w(r) - \beta k(r), \\ u_{ab}(r) &= -\beta k(r), \end{aligned} \tag{2.47}$$

where $w(r)$ is the hard-sphere interaction, and $k(r)$ is the Gaussian covariance of the disordered potential. The replicated PY relation takes therefore the final form

$$\begin{aligned} c(r) &= (1 + h(r) - c(r))(e^{-\beta w(r) + \beta^2 k(r)} - 1), \\ c^d(r) &= (1 + h^d(r) - c^d(r))(e^{\beta^2 k(r)} - 1). \end{aligned} \tag{2.48}$$

2.3.2 HyperNetted Chain

Starting with the PY relation (2.44) for the bulk system, we might rewrite it in the following way :

$$\begin{aligned} c(r) &= (1+h(r)-c(r))e^{-\beta u(r)} - 1 - h(r) + c(r), \\ h(r) &= e^{-\beta u(r)} \underbrace{(1+h(r)-c(r))} -1, \end{aligned}$$

where the bracketted term can be seen as the first term of a Taylor expansion of $e^{h(r)-c(r)}$. Therefore, we can rewrite the last equation as

$$h(r) \approx e^{-\beta u(r)+h(r)-c(r)} - 1. \tag{2.49}$$

This equation is called the HyperNetted Chain (HNC) closure relation for the bulk fluids. The HNC closure relation is an other way of rewriting $h(r)$ in terms of $c(r)$, and will obviously lead to different results compared to the PY relation. The reason for this is their very expression, and the way the correlations are treated in each one of them.

In order to specialize this equation to systems with a frozen disorder, we follow the scheme used for the PY relation, in which the first step consists in writing the equation for a multicomponent system:

$$h_{ab}(r) = e^{-\beta u_{ab}(r)+h_{ab}(r)-c_{ab}(r)} - 1. \tag{2.50}$$

Separating the intra and the inter replica components, we get :

$$\begin{aligned} h_{aa}(r) &= e^{-\beta u_{aa}(r)+h_{aa}(r)-c_{aa}(r)} - 1, \\ h_{ab}(r) &= e^{-\beta u_{ab}(r)+h_{ab}(r)-c_{ab}(r)} - 1, \end{aligned} \tag{2.51}$$

with $a \neq b$. And finally using the notation defined above, we get the HNC closure relation for systems with a quenched disorder:

$$\begin{aligned} h(r) &= e^{-\beta w(r)+\beta^2 k(r)+h(r)-c(r)} - 1, \\ h^d(r) &= e^{\beta^2 k(r)+h^d(r)-c^d(r)} - 1. \end{aligned} \tag{2.52}$$

2.3.3 Mean Spherical Approximation

Starting with the HNC equation, and considering a case where $u(r) = w(r) + \phi(r)$, with $w(r)$ the hard-sphere potential and $\phi(r)$ a weak long-range tail, we might tentatively write

$$\begin{aligned} h(r) &= e^{-\beta w(r)-\beta\phi(r)+h(r)-c(r)} - 1 \\ &= e^{-\beta w(r)} e^{-\beta\phi(r)+h(r)-c(r)} - 1 \\ &\approx e^{-\beta w(r)}(1-\beta\phi(r)+h(r)-c(r)) - 1, \end{aligned} \tag{2.53}$$

where the last line results from a Taylor expansion on the second exponential on the r.h.s. The resulting equation is called the Mean Spherical Approximation, developped by Lebowitz and Percus (1966). A better and clearer way to look at the MSA closure is the following, for the case treated here:

$$\begin{cases} h(r) = -1 & \text{inside the core,} \\ c(r) = -\beta\phi(r) & \text{outside the core.} \end{cases} \tag{2.54}$$

This closure relation takes a much simpler form compared to HNC and PY, developed heretofore, but its validity is nonetheless to be tested. Particularly in this kind of problems, it seems that a more complicated expression, including more terms, does not lead to especially improved results.

Following the same scheme as previously, one may derive the replicated MSA equation:

$$\begin{aligned} h(r) &= e^{-\beta w(r)}(1 + \beta^2 k(r) + h(r) - c(r)) - 1, \\ c^d(r) &= \beta^2 k(r). \end{aligned} \tag{2.55}$$

The last expression follows from the lack of an inter-replica hard-core interaction.

2.3.4 Exponential

Developed by Andersen *et al.* (1972) the exponential closure relation takes the form of a renormalized perturbation theory. The method has initially been developed to account for attractive interparticle Lennard-Jones potentials, and considers the latter as a perturbation over a reference system. This closure relation is applicable here as well, by setting the reference system as the bulk one, and the potential as the perturbation. Therefore, this method contrary to PY, HNC, and MSA, does take its roots from a physical argument.

In the framework of this closure relation, the correlation functions are approximated through means of diagrammatic methods. The advantage of a diagrammatic method is the possibility to classify and distinguish integrals, represented by the diagrams, according to symmetry and topology criteria. Following a separation of the correlation functions in short and long range contributions, each of them is approximated in a different way. The diagrams of both contributions are classified using a parameter γ such that γ^{-1} measures the range of the external potential. The short range correlations are then approximated using the MSA closure relation, which aims to represent the reference system in the following way:

$$\begin{cases} h^{\text{ref}}(r) = -1, \quad r < d, \\ c^{\text{ref}}(r) = 0, \quad r > d, \\ h^{d,\text{ref}}(r) = 0, \quad \forall r, \end{cases} \tag{2.56}$$

where the disconnected correlation functions are obviously equal to zero, since the reference system does not consider any external potential. In an alternative scheme, which is actually the original one, the reference system is treated exactly, but the use of the MSA results instead is generically found to represent a minor approximation.

In a first step, the MSA is used for the full system as well, which reads

$$\begin{cases} h^{\mathrm{MSA}}(r) = -1, \quad r < d, \\ c^{\mathrm{MSA}}(r) = \beta^2 k(r), \quad r > d, \\ c^{d,\mathrm{MSA}}(r) = \beta^2 k(r), \quad \forall r. \end{cases} \tag{2.57}$$

Several ways have been designed to take a further step, and the first one leads to the EXP approximation. In this approximation, we define the chain sums $\mathcal{C}^*(r)$ and $\mathcal{C}^{*d}(r)$ as

$$\begin{aligned} \mathcal{C}^*(r) &= g^{\mathrm{MSA}}(r) - g^{\mathrm{ref}}(r), \\ \mathcal{C}^{*d}(r) &= g^{d,\mathrm{MSA}}(r) - g^{d,\mathrm{ref}}(r). \end{aligned} \tag{2.58}$$

The chain sum takes the form of a potential applied to the reference system. As this potential is applied on top of a hard-core one, it is said to be "renormalized". Due to the previous approximations, and the fact that the long range parts of the correlation functions are screened by the short ranged parts, this potential is said to be "renormalized". The essential step to obtain the higher order approximation EXP, is done by a careful understanding of the nature of the diagrams included, and those that are neglected. Adding the so-called "ring" diagrams, and retaining all the diagrams with a nodal order of two or less, and performing additional manipulations using the properties of the diagrams leads to the following expression for the radial distribution functions:

$$\begin{aligned} g(r) &= g^{\mathrm{ref}}(r) e^{\mathcal{C}^*(r)}, \\ g^d(r) &= g^{d,\mathrm{ref}}(r) e^{\mathcal{C}^{*d}(r)}. \end{aligned} \tag{2.59}$$

Inserting the expressions for the reference system calculated using the MSA, this leads to

$$\begin{cases} h^{\mathrm{EXP}}(r) = -1, \quad r < d, \\ h^{\mathrm{EXP}}(r) = (1 + h^{\mathrm{ref}}(r)) e^{h^{\mathrm{MSA}}(r) - h^{\mathrm{ref}}(r)} - 1, \quad r > d, \\ h^{d,\mathrm{EXP}}(r) = e^{h^{d,\mathrm{MSA}}(r)} - 1, \quad \forall r, \end{cases} \tag{2.60}$$

which is the form of the EXP closure relation that has been used in this work, though as one may see in chapter 3, this closure relation did not give the expected results.

Chapter 3

Structural properties of a fluid in a random potential

The structural properties of a fluid are a very important step in understanding the dynamics of the system. Indeed, as one can see in chapter 4, the memory function of the generalized Langevin equation contains a term called the memory function, which encodes the critical and difficult part of the dynamics. Therefore, on the proper calculation of this term lies the validity of the results, and this term is solely expressed in the framework of MCT in terms of the structural functions, total and disconnected as described in chapter 2. Soling the structural properties is done through solving the Ornstein-Zernike (OZ) equation together with a chosen closure relation. Those that have been tested are presented in chapter 2, and the results are presented in this very chapter.

3.1 General results with HNC

The bulk of the calculations have been undertaken using the HyperNetted Chain (HNC) closure relation (see chapter 2) for the structural calculations. This closure relation is known to perform very well for fluids that present a smooth interaction. This at first glance seem not to be the case here, but the external potential can be seen as an effective interaction between the particles, and this becomes clear if one looks at the effective Hamiltonian that can be derived using the replica trick (chapter 2). In this way, HNC came out at a first good choice, and showed later on to be the best among all the other closure relations. Therefore, the more general results will be presented using this very closure relation.

One first and easy to interpret result that we may compute is that of the bulk system, i.e. $\delta = 0.0$ which sets the amplitude of the potential uniformly to zero. In this case, the disconnected correlation functions will all yield a expected zero result. This is of course

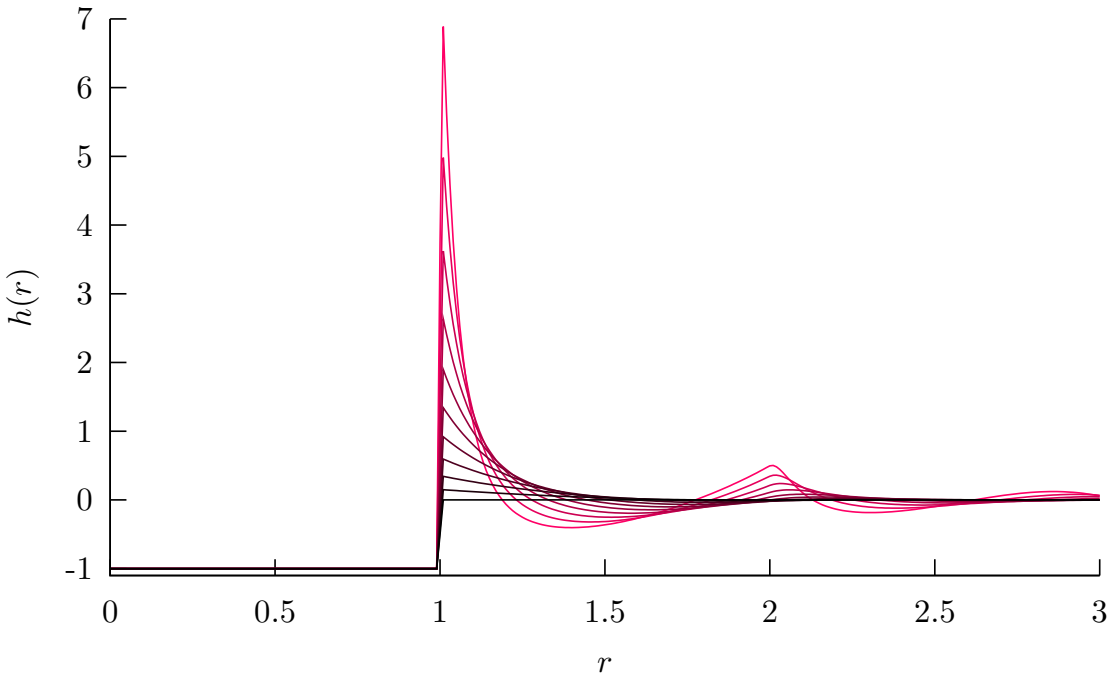

Figure 3.1: Total correlation function $h(r)$ of a fluid of N hard-spheres, calculated with the OZ equation together with the HNC closure relation. The density of the fluid goes up with the saturation of the color of the curves, the lowest density being $\rho = 0.0$ and the highest $\rho = 1.0$.

to be expected, since the disconnected functions are giving the correlations between two particles that are conveyed through the disordered potential. The usual total correlation function can however be calculated, and is presented in figure 3.1.

As the density increases, different peaks become more and more visible in the total correlation function. The value of $h(r)$ is closely linked to the probability of finding a particle at a distance r of the reference particle, normalized with that value in an ideal gas, i.e. a fluid in which particles have no interaction. One peak rises very fast with the increase in density at $r = 1$, and therefore corresponds to the first neighbor of the reference particle, the unit of length being the diameter of a particle, and no polydispersity having been introduced. A second peak grows as well around $r = 2$ and corresponds to the second neighbors, and then a third around $r = 3$. The height of the peaks is decreasing, and the probability of finding a particle at that precise distance with respect to a ideal gas as well. At infinite distance eventually, no precise correlation can be monitored, and the fluctuations decrease to zero, which is therefore the value they have in an ideal gas.

On the other hand, one can chooses to keep a constant value of δ and instead increase the value of the density. The simplest case of this option is when $\rho = 0.0$, which means

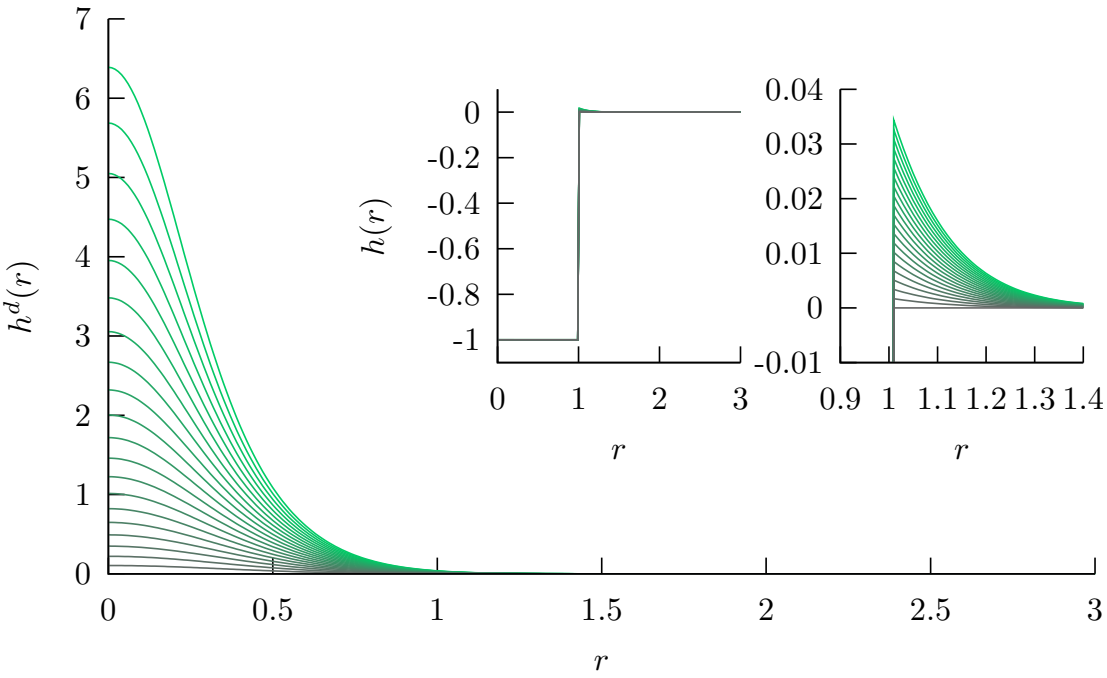

Figure 3.2: Total disconnected correlation function $h^d(r)$ usual total correlation function (graphs in inset, the right picture is a zoom of the left one) of a fluid of N hard-spheres in a disordered potential of amplitude δ, calculated with the OZ equation and the HNC closure relation. The amplitude of the fluid goes up with the saturation of the color of the curves by steps of $\Delta\delta = 0.1$, the lowest amplitude being $\delta = 0.0$ and the highest $\delta = 2.0$.

that either only one particle is present in the system, or the particles are at virtually infinite distance from one another. In this case, the usual total correlation function is of little to no interest, since no correlation between the particles is expected to be observed. The disconnected total correlation function however is a quantity that might bring some insight about the correlations, since it represents the correlations between the particles that is conveyed through the disordered potential.

Contrary to the total correlation function, the disconnected total correlation function does not have the hard-sphere core potential that prevents any correlation from happening below the distance of a diameter. Therefore, even though particles are supposedly not in contact in the case of $\rho = 0.0$, correlations can be found at small distances, as is can be seen from figure 3.2. In this figure, the large graphs shows a disconnected total correlation function, and each curve is drawn for a different value of δ, with an increase of the saturation meaning an increase of the value of that parameter, in order to keep the picture intuitive. The graphs in inset shows the total correlation function $h(r)$.
The first thing that is noticeable is the the short distance values of $h^d(r)$ increases with

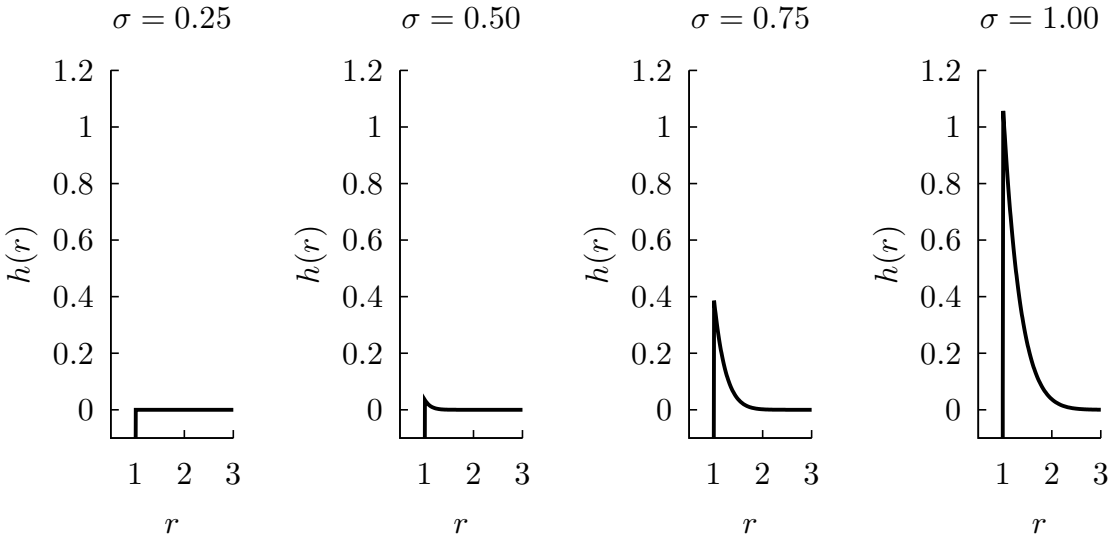

Figure 3.3: Total correlation function of a fluid of N hard-spheres in a disordered potential of amplitude $\delta = 2.0$ and density $\rho = 0.0$, calculated with the OZ equation and the HNC closure relation. The four graphs are calculated for increasing values of σ, ranging from 0.25 to 1.00.

an increase of the amplitude of the potential, which is expected, since this function describe the correlations that come through the potential. The correlation are increasing steadily, and no anomalous behavior seems to happen in this case.

One other thing to be seen here, is that $h(r)$ which was expected to be flat outside the hard-sphere core, presents very small but noticeable correlations around $r = 1$. The reason for this is that since all the correlation of the system is brought solely by the disorder, we can write $h(r) = e^{-\beta(k(r)-w(r))} - 1$ where $u(r)$ is the covariance of the disordered potential, and $w(r)$ is the hard-sphere potential, in the case of the HNC closure relation. In $h(r)$ the hard-sphere core overwrites the inside correlations brought by $h^d(r)$, and the remaining outside correlations are therefore due to the tail of $h^d(r)$. This means that two particles that cannot enter in contact due to he too low density, are still having correlations, that are the correlations the disordered potential has between the points the particles occupy. This effect is therefore expected to increase with the value of the correlation length of the potential σ. And indeed, as shown by figure 3.3, the total correlation at constant δ and density increases with the value of the correlation length of the potential σ.

The most interesting structural feature of a system with a disordered potential is when a constant value of the amplitude of the potential δ is maintained, and the density of the system increased steadily. The result of such a process on the disordered total correlation function can be seen in figure 3.4.

As the density increases, the correlations due to the potential are decreasing, and this

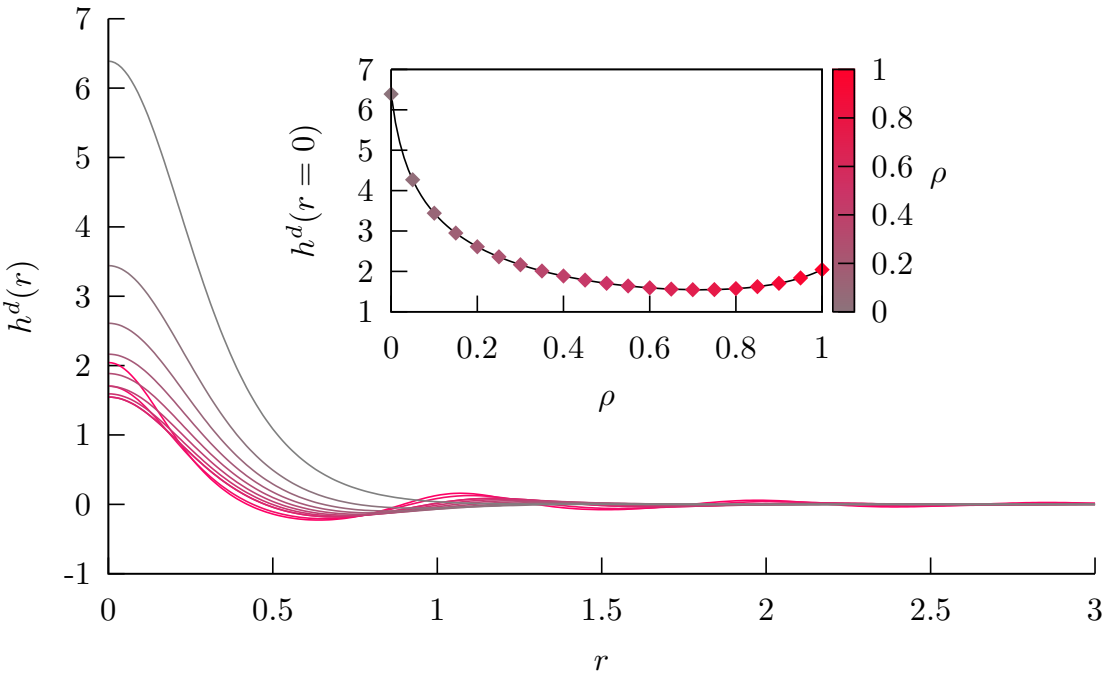

Figure 3.4: Total disconnected correlation function of a fluid of N hard-spheres in a disordered potential of amplitude $\delta = 2.0$, a correlation length of $\sigma = 0.50$, and an increasing density ranging from 0.0 to 1.0 by steps of $\Delta\rho = 0.1$. The saturation of the color is proportional to the value of ρ. The graph in inset shows the variation of the value of $h^d(r)$ at distance $r = 0$ in function of the density.

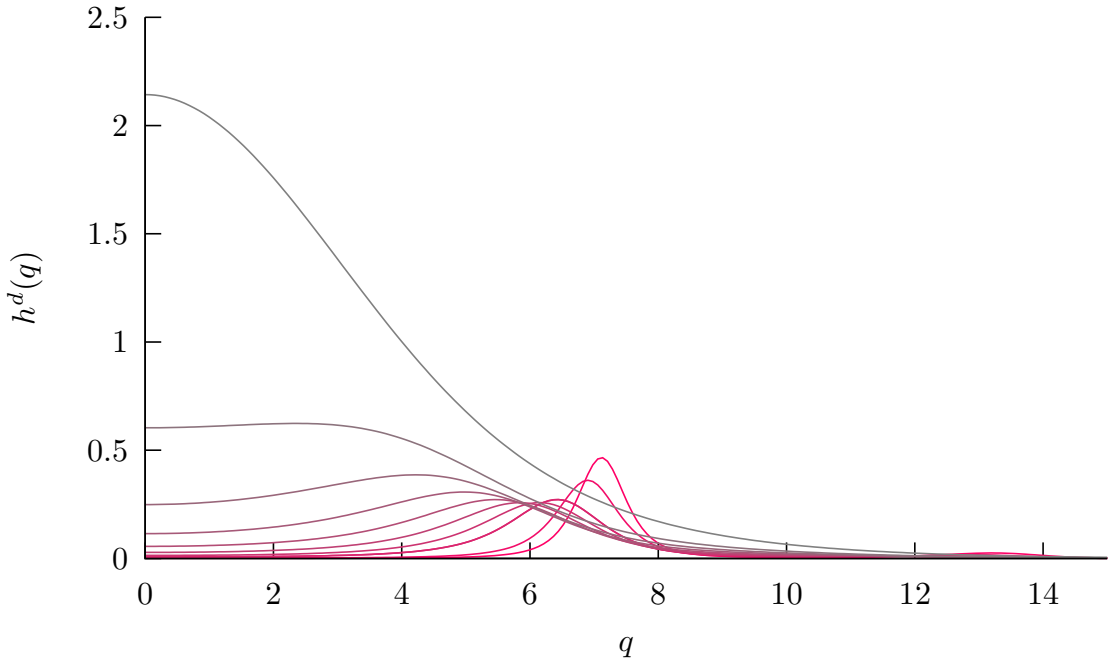

Figure 3.5: Fourier transform of the total disconnected correlation function of a fluid of N hard-spheres in a disordered potential of amplitude $\delta = 2.0$, a correlation length of $\sigma = 0.50$, and an increasing density ranging from 0.0 to 1.0 by steps of $\Delta\rho = 0.1$. The saturation of the color is proportional to the value of ρ.

is due to the fact that a higher value of ρ leads the steric interactions to have more ad more importance. The steric interaction leading to a strong hard-sphere potential, its influence therefore quickly takes over the softer influence of the disordered potential, which leads to a quick decrease of the value of $h^d(r)$. However, this is only true for low to mid value of ρ, and one can see that at high values of the density the density, $h^d(r)$ starts to increase again. This may not be clear from the highly overlapping graphs, but can be more clearly seen if one plots $h^d(r = 0)$ in function of ρ, which gives a good idea of this behavior. This has been done in the inset graph of figure 3.4, and the trend is clear : the potential-induced correlations diminish from low to mid densities, and increase from mid to high values of this parameter. This phenomenon reflects the one treated in chapter 5, where the dynamics of the system is accelerating as the density increases, before decelerating again at high density. Therefore, the non monotonous behavior of the dynamics are very probably caused by the non monotonous behavior of the structure.
The Fourier transform of the disconnected total correlation function $h^d(q)$, as shown in figure 3.5 gives a different insight on this phenomenon.
As expected in this case, the initially high peak the correlation function presents at the vicinity of $q = 0$ is decreasing dramatically with an increase of the density. For high values of the density however, a new peak starts to grow around $q = 7$. The growth

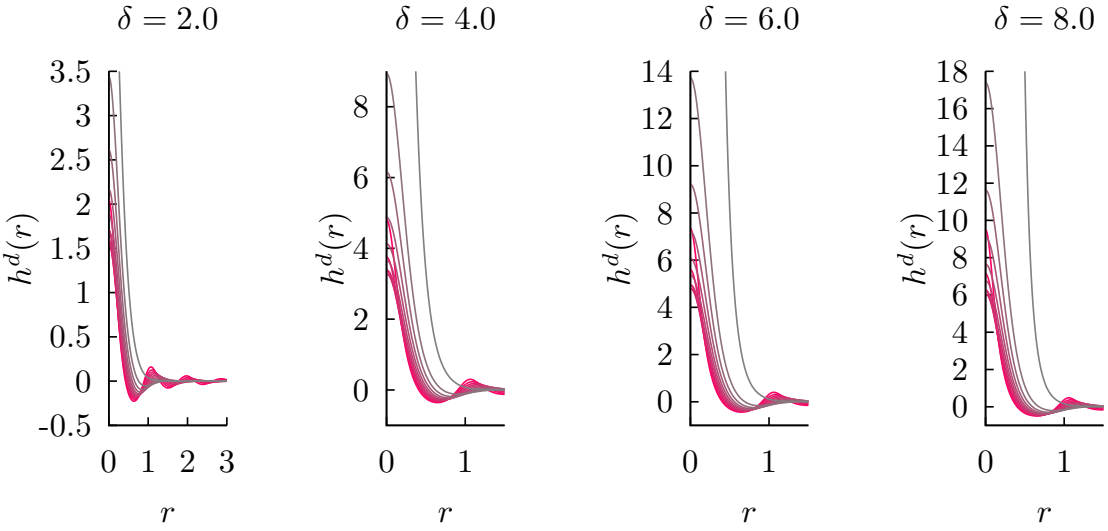

Figure 3.6: Total disconnected correlation function of fluids of N hard-spheres in disordered potentials of amplitude $\delta = 2.0, 4.0, 6.0, 8.0$ with a correlation length of $\sigma = 0.50$. The different curves are for increasing density ranging from 0.0 to 1.0 by steps of $\Delta\rho = 0.1$. The saturation of the color is proportional to the value of ρ. The curves representing $\rho = 0.0$ have been cut for the sake of readability.

of this new peaks makes the overall correlations to increase again, and also pinpoints the start of a new regime. This shows that the correlations that arise at high values of the density are of a different nature than those present at low values of the density. We could postulate that at low value of the density, the potential plays a huge role in positioning the particles, those having not many collisions with rest of the fluid. However, as the density increases, the hard-sphere density related interactions take over the much smoother potential, leading to a decrease of $h^d(r)$. At high value of the density however the crowding becomes so intense that the fluid starts to slow down leading in turn to a reduced importance of the density related effects. In this case, the fluid is very dense and slow and small deviations of the position of a particle can be caused by the presence of a minimum or a maximum of the potential in its vicinity. TO sum up, at low density the potential can shape the structure of the fluid on large scales due to the rare interactions the particles have with the recite of the fluid. At high values of the density, crowing lets the potential to shape the correlations on a much more smaller level, due to the dense crowding. Of course these suppositions have to be verified with simulations and actual studies of the behavior of the fluid and its correlations.

This loss of correlation at mid values of the density is a phenomenon that becomes more important as the amplitude of the potential increases, as it can be seen from figure 3.6. The values at $r = 0$ are known analytically as $h^d(r = 0)|_{\rho=0.0} = e^{\delta} - 1$, and have

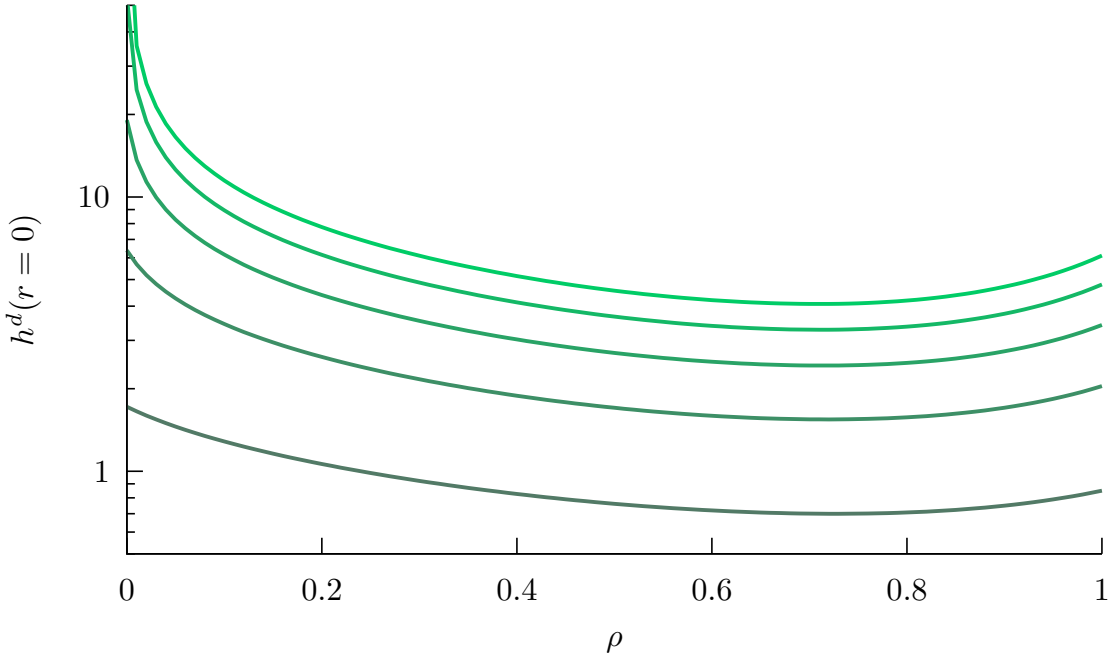

Figure 3.7: Total disconnected correlation function at a zero distance $h^d(r=0)$ in function of the density ρ of fluids of N hard-spheres in disordered potentials with correlation lengths of $\sigma = 0.50$. The different curves are for increasing amplitudes $\delta = 2, 4, 6, 8$. The value of $h^d(r=0)|_{\rho=0}$ has been cut out for the sake of readability, but can be found above. The saturation of the color is proportional to the value of δ.

therefore not been plotted, to keep the figure readable. We get for the different values of δ presented in figure 3.6:

$$h^d(r=0)|_{\delta=2.0,\rho=0.0} \approx 6.39$$
$$h^d(r=0)|_{\delta=4.0,\rho=0.0} \approx 53.60$$
$$h^d(r=0)|_{\delta=2.0,\rho=0.0} \approx 402.43$$
$$h^d(r=0)|_{\delta=2.0,\rho=0.0} \approx 2979.96$$

These values are in striking contrast with the values of $h^d(r=0)|_{\rho=0.1}$ that can be seen on the figure, for which the influence of δ is much smaller. Therefore, as the amplitude of the potential increases, the loss of correlations with the increase of the density increases dramatically, by factors of thousands. The following resurgence of correlations at high values of the density however does not follow this rather extreme trend. In figure 3.7 the value of $h^d(r=0)$ is plotted in function of the density of the fluid.
It can be seen that, although the correlations increase again with an increase of the density, the effect responsible for this does not lead the correlations to meet the values

they have at low values of the density. This seems to work with the assumption that the potential induced correlations at high density induces only minor and short range influence on the structure of the fluid.

3.2 Comparisons with other closure relations

These last very general features of the correlations are not specific to HNC, but are a common feature of all the closure relations and can therefore be thought to have some kind of universality built into them. Something however that is not invariant is the strength with which the different closure relations treat the correlations, both coming from the potential and coming from the fluid. This will have dramatic consequences as for the way the dynamics is treated because, as stated before, the dynamics are fully dependent on the structure.

Figure 3.8 shows a comparison of the HNC ans the MSA closure relations in terms of total correlation functions, both usual and disconnected. It is clear that the MSA closure relation treats the correlations in a lighter way. The reason for this is not obvious at first, but can be seen from the equations of the closure relations themselves, in which the HNC treats the interparticle interactions inside a exponential, while MSA has a linear construction, leading to a softer treatment of the correlations.

This happens in a similar way concerning the PY closure relation, as seen in figure 3.9. The PY closure relation underestimates the correlations, both disconnected and usual, compared to the HNC closure relation in a way that is very reminiscent of what happens with MSA. This time, the equations themselves do not lead to an easy answer as to why, PY and HNC both being constructed around an exponentiation of the correlations between the particles.

Finally, looking at figure 3.10, we can see that the EXP closure relation is underestimating the usual total correlation function, while overestimating the disconnected total correlation function, compared to HNC.

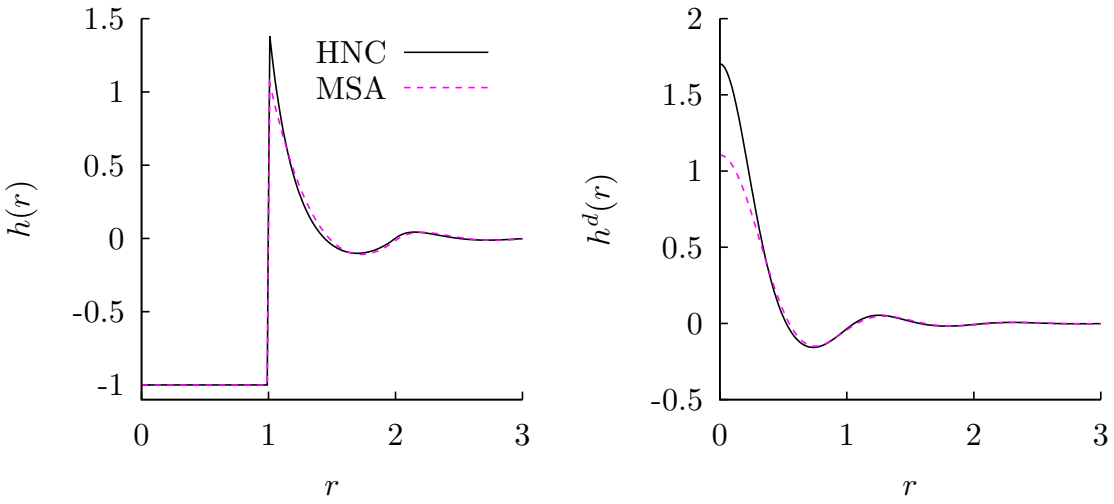

Figure 3.8: Total correlation function (left panel) and disconnected total correlation function (right panel) of a fluid of N hard spheres in a random Gaussian potential, calculated using the OZ equation and the HNC and MSA closures relations (plain black and dotted pink curves respectively) at a density of $\rho = 0.50$, an amplitude of the potential of $\delta = 2.0$ and a correlation length of the potential of $\sigma = 0.5$.

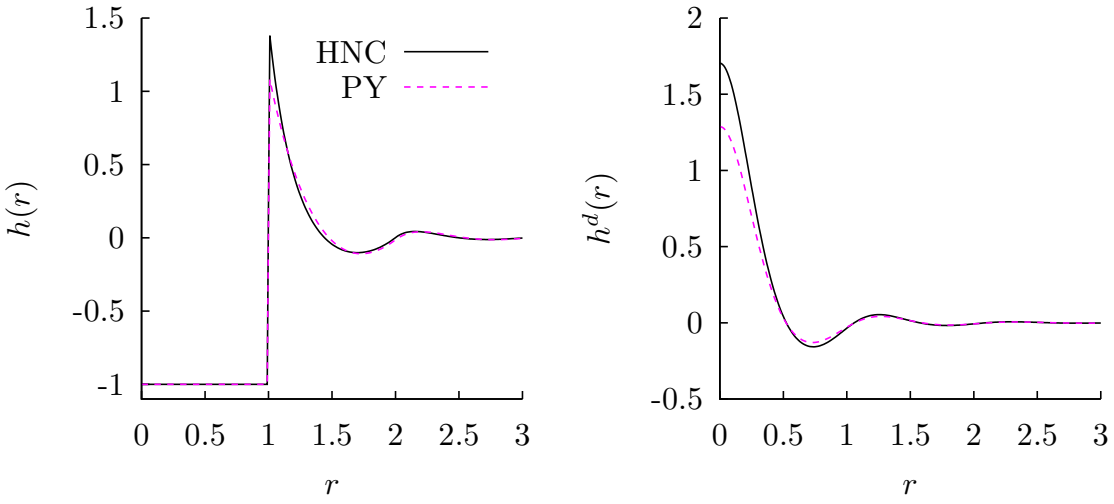

Figure 3.9: Total correlation function (left panel) and disconnected total correlation function (right panel) of a fluid of N hard spheres in a random Gaussian potential, calculated using the OZ equation and the HNC and PY closures relations (plain black and dotted pink curves respectively) at a density of $\rho = 0.50$, an amplitude of the potential of $\delta = 2.0$ and a correlation length of the potential of $\sigma = 0.5$.

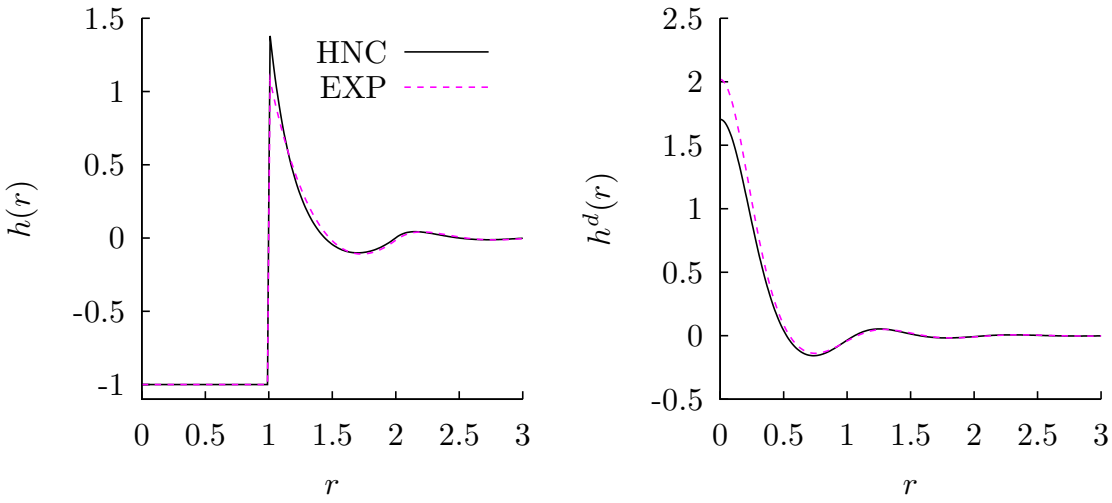

Figure 3.10: Total correlation function (left panel) and disconnected total correlation function (right panel) of a fluid of N hard spheres in a random Gaussian potential, calculated using the OZ equation and the HNC and EXP closures relations (plain black and dotted pink curves respectively) at a density of $\rho = 0.50$, an amplitude of the potential of $\delta = 2.0$ and a correlation length of the potential of $\sigma = 0.5$.

3.3 Unfortunate outcomes and unphysical solutions

3.3.1 HNC

Overall even small discrepancies, many of these closure relations give very similar results concerning $h(r)$ and $h^d(r)$. These small discrepancies however can lead to massive different outcomes concerning dynamics, and without possible experimental comparison, selecting a "more accurate" closure relation is not possible. However, one of the reasons why HNC has been kept as the closure relation of choice in this work, is because of the unreliability of most of all the other closures that have been tested.

As interesting as HNC is as a closure relation, it does present its fair share of issues as well, but they mainly occur at extreme values of the correlation length. As showed previously, the increase in correlation length leads to changes in the behavior of the structural functions. The study mainly focuses on $\sigma = 0.5$, being close to what has been experimentally measured. Small increments around this value have been undertaken, but in order to be fully rigorous, a study of the structural functions beyond this arbitrary limit has to be undertaken. Unfortunately, a quick glance to what happens beyond $\sigma = 1.0$, tells us that the limits of the HNC closure relation is exactly the one that has

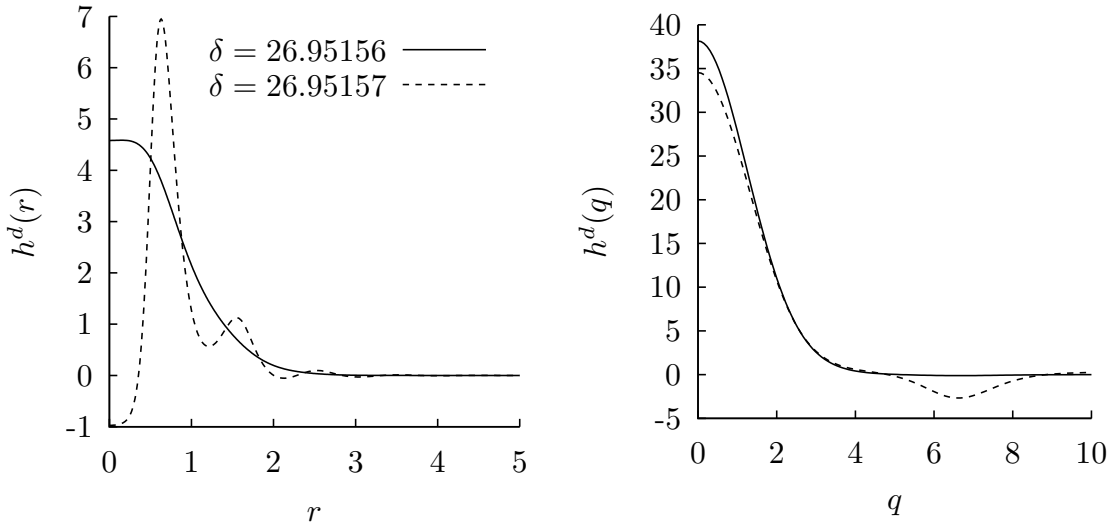

Figure 3.11: Total disconnected correlation function in real (left panel) and reciprocal space (right panel) of a fluid of N hard spheres in a random Gaussian potential, calculated using the OZ equation together with the HNC closure relation at a density of $\rho = 0.08$, an amplitude of the potential of $\delta = 26.95156$ (plain line) and $\delta = 26.95157$ (dashed line), and a correlation length of the potential of $\sigma = 1.25$.

been arbitrarily set. Indeed, if one proceeds to explore the variable space (ρ, δ, σ) further, the structural functions seem to reach very quickly a new branch of solutions. In order to stay consistent with the rest of the calculations, a value of $\sigma = 1.25$ has been tested. The structural functions have then been used as inputs for the calculation of a phase diagram, as described in chapters 4 and 5. At a low value of of the density of $\rho = 0.08$, and an amplitude of $\delta = 26$, which has been later on refined to $\delta = 26.95156$, the dynamical calculations seemed to meet a new branch of solutions, that had physically no sense. This phenomenon could be traced down to its structural origins, as an unexpected behavior of $h^d_{\mathbf{q}}$. In figure 3.11 is shown the disconnected total correlation function in real and reciprocal space at the precise point where this new branch of solutions is met.

As it can be seen from the right panel, the disconnected total correlation function changes very suddenly, passing the value $\delta = 26.95156$, and present afterwards a negative peak around $q = 7$. The corresponding change in the real space behavior is even more dramatic, with a disconnected total correlation function presenting very clear oscillations where it previously was simply monotonically decreasing.

Such a behavior is physically unrealistic, and is prohibited by the very definition of the disconnected total correlation function in reciprocal space :

$$h^d_{\mathbf{q}}(t) = \overline{\langle \rho_{\mathbf{q}}(t) \rangle \langle \rho^*_{\mathbf{q}}(t) \rangle} \tag{3.1}$$

which has the symmetry of the square of the complex function $\rho_{\mathbf{q}}(t)$, and cannot therefore be negative. A positive Fourier component is by definition a property of the disconnected total correlation function, and an essential characteristic of all correlation functions in general. This requirement is however not taken into account by the OZ equation nor by the HNC closure relation. Therefore, the mathematical structure of these relations leads, after multiple iterations and at extreme values of the correlation length, to the consequence that the disconnected total correlation function does not present anymore the main characteristic of a correlation function. This is unfortunate, and because it is purely a mathematical artifact without any physical explanation, nothing can be really done to circumvent the problem. This new branch of solution, event though mathematically allowed, is unrealistic and leads the dynamical calculations in a dead end. Increasing the value of σ further leads to the same result.

3.3.2 Percus-Yevick

The PY closure relation, which is one of the most used relations and is well known for its accuracy concerning hard-sphere systems has been tested on the present system as well. Unfortunately, its failures are even more dramatic than those of the HNC closure. Considering that the purpose of calculating the structural properties is being able to calculate the phase diagram and other dynamical properties, PY fails almost entirely. Figure 3.12 shows the Fourier component of the disconnected total correlation function at a given low value of the density $\rho = 0.15$, and respectively $\delta = 2.0$ and $\delta = 4.0$. nfigure As one can see, a small increase of the amplitude from $\delta = 2.0$ to $\delta = 2.0$ leads h_q^d to present an unwelcome negative minimum around $q = 13$. This minimum leads to a total failure of the MCT equations, that require only positive values to calculate the dynamical variables and the phase diagram. An increase of the amplitude of the potential beyond $\delta = 4.0$ leads to a failure of the iterative resolution of the OZ equation and the PY closure relation as well. Furthermore, an increase of the density at low values of the amplitude leads to the apparition of the same negative minimum. It seems that the PY relation fails very early, both in terms of density and of amplitude of the potential. Its the area of exploitability is therefore confined to the bottom left of the phase diagram, and to the regions of high density.

3.3.3 EXP

On the other hand, the EXP closure relation has a good performance, for the low values of the density. But the high densities are the issue with this closure relation. Figure 3.13 shows the Fourier component of the connected static structure factor S_q^d for a high density of $\rho = 1.0$ and an amplitude of $\delta = 0.5$. The static structure factor is defined as

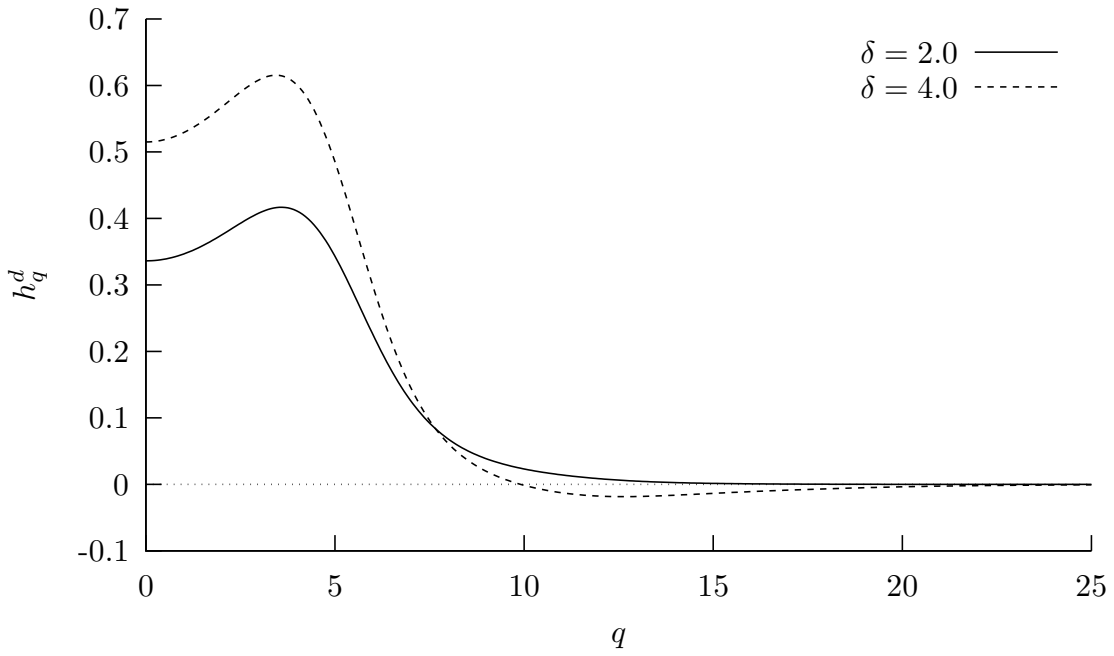

Figure 3.12: Fourier component of the total disconnected correlation function of a fluid of N hard spheres in a random Gaussian potential, calculated using the OZ equation together with the PY closure relation at a density of $\rho = 0.15$, an amplitude of the potential of $\delta = 2.0$ (plain line) and $\delta = 4.0$ (dashed line), and a correlation length of the potential of $\sigma = 0.5$.

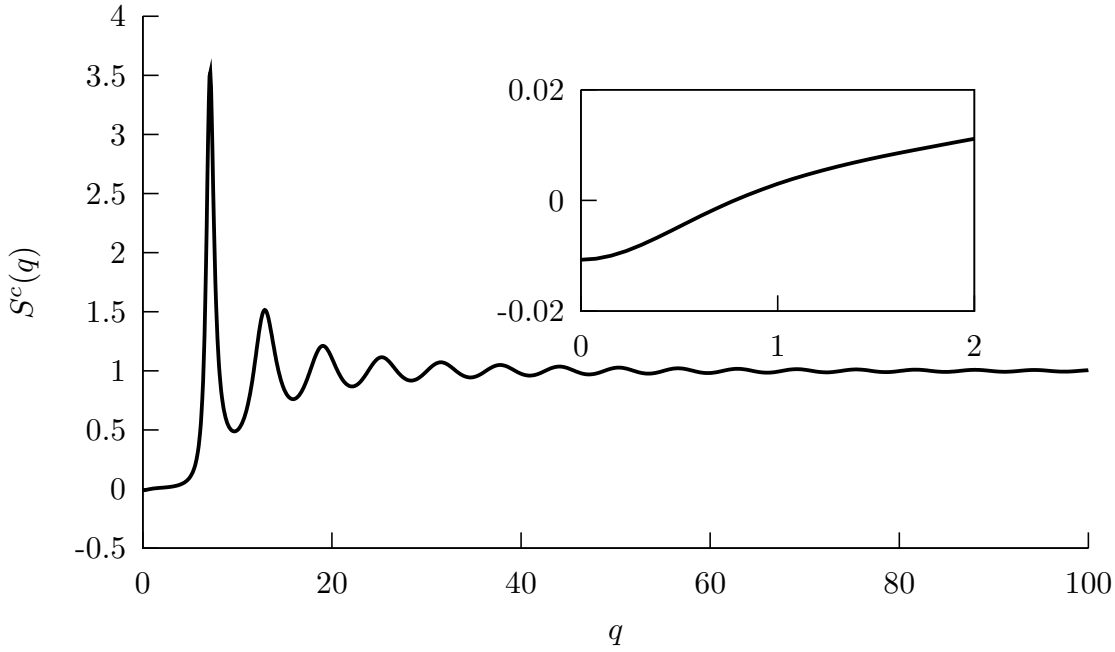

Figure 3.13: Fourier component of the connected static structure factor of a fluid of N hard spheres in a random Gaussian potential, calculated using the OZ equation and the HNC closure relation at a density of $\rho = 1.0$, an amplitude of the potential of $\delta = 0.5$ and $\delta = 4.0$, and a correlation length of the potential of $\sigma = 0.5$.

;

$$S_q^c = 1 + \rho h_q^c \tag{3.2}$$

where h_q^c is the connected total correlation function, and is subject to the same limitations than h_q^d concerning the fact that it cannot have negative values, in order to be a proper correlation function. Therefore, as one can see on the graph in inset, which is simply a zoom of the first values of S_q^c, this function presents a negative peak around $q = 0$, which increases with the increase of the amplitude of the potential. This negative peak leads here again unfortunately the dynamical calculations to encounter a dead end.

All these problems should be seen as further justifications of why the HNC closure relation has been chosen as the relation of choice : PY does not allow for calculations at low values of the density, EXP encounters similar problems at high values of the density. And finally, while HNC and EXP lead to similar results when calculation is possible, MSA and PY leads extreme values of the phase diagram. While this is not necessarily an issue, the fact that HNC is known to be very accurate, and that MSA is known to be a simplistic closure relation contributes to push MSA aside, and consider HNC as our closure relation of choice.

Chapter 4

Dynamics of a hard-sphere fluid in a disordered environment: Mode Coupling Theory

The original eponymous Langevin equation developed in 1908 (Lemons and Gythiel, 1997) takes the simple assumption of a particle, said to be Brownian, in a solvent itself composed of smaller particles. This development came from the need to understand observations made by Jan Ingenhousz and Robert Brown of respectively coal dust particles in an alcohol solution and pollen grains in water, that were seemingly moving in a random fashion. In those cases, the pollen and the dust are the Brownian particles, whose size compared to the solvent molecules is huge. This very difference in sizes and therefore of timescales leads to an actual separation of these two types of particles, that allows for an efficient treatment of the forces in action in this system. The first force felt by the Brownian particle takes the form of an isotropic random force with a Gaussian distribution that pushes the particle in a different direction at every moment. This force is due to the presence of the multiple solvent particles around the big particle, and their collisions with the latter are at the origin of the observed effect. The second force to be accounted for takes the form of a friction force that appears when the big particle attempts to pass through a bulk of solvent particles. Hence, the solvent particles are responsible both for the dynamics and the damping of the dynamics of the big particle (Haw, 2002; Hänggi and Marchesoni, 2005; Frey and Kroy, 2005; Babič *et al.*, 2005). The Langevin equation takes the following form:

$$m\ddot{x}(t) = -\lambda\dot{x}(t) + \eta(t), \tag{4.1}$$

where m is the mass of the big particle, $x(t)$ its position, λ is the friction coefficient and η is the random force that pushes the particle around.

The presence of a random isotropic force in the Langevin equation accounts for the so-

called Markovian processes in Brownian systems. A process is called Markovian when, if this process is stochastic, the probability of obtaining a certain outcome at time, say, $t+1$ only depends on the immediate past of the process, i.e., its state at time t. In more rigorous terms, one can write, for a random variable X that follows a Markovian scheme,

$$P(X_{t+1} = x|X_0, X_1, X_2, ..., X_t) = P(X_{t+1} = x|X_t), \tag{4.2}$$

where x is the outcome of the process.

A Markovian process is thus characterizing phenomena with a very small correlation time, virtually none, which is precisely the case of the collisions of the solvent particles against the big particle. The latter point seems obvious, but specifying the underlying reasons can be of some utility. We can distinguish two major time scales that are at play in Brownian motion, namely $\tau_s \approx 10^{-12}$ s, the relaxation time of a solvent particle, and $\tau_b \approx 10^{-3}$ s the relaxation time of the Brownian particle. Clearly the difference in timescales is huge, and its origin can be traced back to the difference in size between the two types of particles. The Markov property of Brownian motion thus comes from the fact that, due to the humongous difference in timescales, the number of collisions experienced by the Brownian particle is of the order of 10^{14} per second. Clearly, after 10^{14} collisions, no memory of the first one can be kept, and the whole process can be thought as being a memoryless random process.

Is the Langevin equation still valid when one wants to calculate the properties of a fluid like the one described in chapter 1? As a reminder, we consider a fluid made of N identical sized particles with a hard-sphere potential, undergoing their dynamics in a three dimensional Gaussian random potential with a Gaussian correlation function. Clearly, we are far from the considerations of Einstein, von Smoluchovski and Langevin, since each particle is plunged in a bath of other identical particles, and both the scales of size and time are of the same order of magnitude. The essential hallmark of the historical Langevin equation is the clear separation of those scales: the forces arising from the solvent particles are the "fast" variables, and are therefore treated altogether as a white noise; the position of the big particle is the "slow" variable and the one we want to get the behavior of. The absence of a clear timescale separation makes it impossible to treat the present system in such a simple way. In order to recover an equation of motion in the form of a Langevin equation, one has to separate "slow" variables from "fast" variables in a way that correctly represents the physical nature of the system.

The whole problem stands on the basis of a good definition for the fast and slow variables, and this is very dependent on the system under study. A good definition leads then to the development of a new equation of motion, that accounts for the new variables. Such an equation is called a Generalized Langevin Equation (GLE), and its development will be the point of this chapter. A lot of quantities used in this development are defined

and explained in chapter 2, one can refer to there for more information. In order to keep the derivation as straightforward as possible, the generalized Langevin equation for N hard-spheres in a Gaussian random potential will be directly derived: the bulk system will be considered as a particular case of this one. After having defined and derived the generalized Langevin equation, approximations will be made that will lead to the derivation of the Mode Coupling Theory (MCT), that allows for an actual solution of the GLE, and more importantly accounts for the non-Markovian processes in an accurate way Götze (1991, 2009).

Knowing the strengths and the weaknesses of a theory is important, and MCT has it fair share of both of them. This theory is mostly known to correctly predict nontrivial dynamical scenarios, such as the reentry phenomenon and logarithmic relaxations in the slow dynamics of fluids with short-ranged attractions (Foffi *et al.*, 2002; Zaccarelli *et al.*, 2002; Sciortino *et al.*, 2003; Pham *et al.*, 2004). More recent studies show its ability to reproduce strong non-monotonic variations of the dynamics of fluids confined in slit pores (Lang *et al.*, 2010; Mandal *et al.*, 2014).

On the other hand, MCT tends to consisteltly overestimating the dynamical slowing down of the liquid, which leads to the usual prediction of sharp ergodicity beaking (Götze and Sjögren, 1992; Götze, 1999). This will lead natuarally to the calculation of transition lines with a great precision, and to the subsequent building of phase diagrams, which even though being issued from a known anomaly of the theory, can lead to fruitful discussion about the behavior of the dynamics for different kind of systems.

The following development relies on a version of the MCT that specializes the theory to systems with quenched-annealed degees of freedom. In particular, it is dealt with a matrix of frozen particles, that aims to represent streamlined models of amorphous porous solids. Single particle system (Götze *et al.*, 1981b,a; Leutheusser, 1983a; Szamel, 2004) and extensions to fluids of nonzero density has been made Krakoviack (2005a,b, 2007, 2009, 2011). The corresponding theoretical predictions have been compared with computer simulation results (Kurzidim *et al.*, 2009, 2010, 2011; Kim *et al.*, 2009, 2010, 2011; Spanner *et al.*, 2013) and show to outline a good picture of the dynamics of the system. This supports the idea that this version of the MCT can indeed be put to good use in studies of fluids in "pure" randomness. The connection with the present problem follows from the observation that the MCT equations for the random fluid-matrix systems make no reference at all to the particulate character of the disorder Krakoviack (2007, 2009). Therefore, whether the disorder is originated from a quenched-annealed matrix, or from an external potential as the one described in chapter 2, does not change the applicability of this theory. This naturally suggests that this framework might have a broader domain of application, encompassing many system that present frozen disorder, to which MCT can be systematically applied after calculation of the structural correlations using the relations presented in chapter 2.

The following presents a detailed derivation of the MCT framework extended to the case of a system with disorder originating from an external potential. One has to keep in mind that this derivation concerns a three-dimensional system ; it has been found that derivation from first principles of this theory in less than three dimensions gives rise to serious difficulties (Götze, 1978, 1979; Götze *et al.*, 1979; Götze, 1981; Leutheusser, 1983b; Schnyder *et al.*, 2011).

4.1 Collective dynamics

4.1.1 Generalized Langevin equation

We consider a fluid made of N spherically symmetric and identical particles of mass m in a Gaussian random potential with a Gaussian correlation function as defined in chapter 1. The volume of the system is given as V, and the total density of the fluid accordingly, as $\rho = N/V$.
We choose to consider the set of slow variables $\delta\rho_{\mathbf{q}}(t) = \rho_{\mathbf{q}}(t) - \langle\rho_{\mathbf{q}}\rangle$, with

$$\rho_{\mathbf{q}}(t) = \sum_{j=1}^{N} e^{i\mathbf{q}\mathbf{r}_j(t)}, \tag{4.3}$$

and $g_{\mathbf{q}}(t) = \sum_{j=1}^{N} \frac{\mathbf{q}}{q} \cdot \mathbf{p}_j(t) e^{i\,\mathbf{q}\,\mathbf{r}_j(t)}$, where $\mathbf{r}_j(t)$ is the position of fluid particle j at time t and $\mathbf{p}_j(t)$ its momentum.
We have the following static correlations:

$$\overline{\left\langle \begin{bmatrix} \delta\rho_{\mathbf{q}} \\ g_{\mathbf{q}} \end{bmatrix} \cdot \begin{bmatrix} \delta\rho_{-\mathbf{q}} & g_{-\mathbf{q}} \end{bmatrix} \right\rangle} = \begin{bmatrix} \overline{\langle \delta\rho_{\mathbf{q}}\delta\rho_{-\mathbf{q}}\rangle} & \overline{\langle \delta\rho_{\mathbf{q}} g_{-\mathbf{q}}\rangle} \\ \overline{\langle g_{\mathbf{q}}\delta\rho_{-\mathbf{q}}\rangle} & \overline{\langle g_{\mathbf{q}} g_{-\mathbf{q}}\rangle} \end{bmatrix} = \begin{bmatrix} NS^c(q) & 0 \\ 0 & Nk_BTm \end{bmatrix}, \tag{4.4}$$

and

$$\overline{\left\langle \begin{bmatrix} \delta\dot{\rho}_{\mathbf{q}} \\ \dot{g}_{\mathbf{q}} \end{bmatrix} \cdot \begin{bmatrix} \delta\rho_{-\mathbf{q}} & g_{-\mathbf{q}} \end{bmatrix} \right\rangle} = \begin{bmatrix} \overline{\langle \delta\dot{\rho}_{\mathbf{q}}\delta\rho_{-\mathbf{q}}\rangle} & \overline{\langle \delta\dot{\rho}_{\mathbf{q}} g_{-\mathbf{q}}\rangle} \\ \overline{\langle \dot{g}_{\mathbf{q}}\delta\rho_{-\mathbf{q}}\rangle} & \overline{\langle \dot{g}_{\mathbf{q}} g_{-\mathbf{q}}\rangle} \end{bmatrix} = \begin{bmatrix} 0 & iNqk_BT \\ iNqk_BT & 0 \end{bmatrix}, \tag{4.5}$$

where $\langle \dots \rangle$ denotes the thermal average, $\overline{\dots}$ is the disorder average, as defined in chapter 2. $S^c(q)$ is the connected static structure factor, defined as $S^c(q) = 1 + \rho h^c_q$, where h^c_q is the Fourier transform of the connected total correlation function.
We define the autocorrelation matrix $\mathbf{C}(q,t)$ of the set of slow variables that have been chosen as

$$\begin{aligned} \mathbf{C}(q,t) &= \frac{1}{N} \overline{\left\langle \begin{bmatrix} \delta\rho_{\mathbf{q}}(t) \\ g_{\mathbf{q}}(t) \end{bmatrix} \cdot \begin{bmatrix} \delta\rho_{-\mathbf{q}} & g_{-\mathbf{q}} \end{bmatrix} \right\rangle} \\ &= \frac{1}{N} \begin{bmatrix} \overline{\langle \delta\rho_{\mathbf{q}}(t)\delta\rho_{-\mathbf{q}}\rangle} & \overline{\langle \delta\rho_{\mathbf{q}}(t) g_{-\mathbf{q}}\rangle} \\ \overline{\langle g_{\mathbf{q}}(t)\delta\rho_{-\mathbf{q}}\rangle} & \overline{\langle g_{\mathbf{q}}(t) g_{-\mathbf{q}}\rangle} \end{bmatrix} = \begin{bmatrix} F(q,t) & C^{\rho g}(q,t) \\ C^{g\rho}(q,t) & C^{gg}(q,t) \end{bmatrix}, \end{aligned} \tag{4.6}$$

where the specific quantity $F(q,t)$ at the top left of the matrix is the density fluctuation autocorrelation function, and its behavior is an indicator of the relaxation undergone by the fluid. Its behavior in time is an indicator of how much correlations the density fluctuations have with their value at initial time. Furthermore, its infinite time value is of great interest as well, since it defines the phase of the fluid, and allows for the building of phase diagrams. It is therefore the main focus in studying the slow dynamics of fluids, hence in the present work.

Using a projection operator denoted as $\mathscr{P}$, that has the property of extracting the slow component of a given variable, we arrive at a generalized Langevin equation for the matrix $\mathbf{C}(q,t)$:

$$\dot{\mathbf{C}}(q,t) = i\mathbf{\Omega}(q)\mathbf{C}(q,t) - \int_0^t d\tau \mathbf{K}(q,t-\tau)\mathbf{C}(q,\tau), \tag{4.7}$$

which is an exact equation for the matrix of correlation functions $\mathbf{C}(q,t)$. $\mathbf{K}(q,t)$ is called the memory function. As it can be seen from the structure of the integral on the r.h.s. of equation (4.7), the memory function accounts for an effect that happens at a time prior to the present moment. It is defined as

$$\begin{aligned}
\mathbf{K}(q,t) &= \overline{\left\langle \begin{bmatrix} 0 \\ R_{\mathbf{q}}(t) \end{bmatrix} \cdot \begin{bmatrix} 0 & R_{-\mathbf{q}} \end{bmatrix} \right\rangle} \left[\overline{\left\langle \begin{bmatrix} \delta\rho_{\mathbf{q}} \\ g_{\mathbf{q}} \end{bmatrix} \cdot \begin{bmatrix} \delta\rho_{-\mathbf{q}} & g_{-\mathbf{q}} \end{bmatrix} \right\rangle} \right]^{-1} \\
&= \begin{bmatrix} 0 & 0 \\ 0 & \overline{\langle R_{\mathbf{q}}(t) R_{-\mathbf{q}} \rangle} \end{bmatrix} \begin{bmatrix} (NS^c(q))^{-1} & 0 \\ 0 & (Nk_BTm)^{-1} \end{bmatrix} \\
&= \begin{bmatrix} 0 & 0 \\ 0 & \dfrac{\overline{\langle R_{\mathbf{q}}(t) R_{-\mathbf{q}} \rangle}}{Nk_BTm} \end{bmatrix} = \begin{bmatrix} 0 & 0 \\ 0 & M(q,t) \end{bmatrix}
\end{aligned} \tag{4.8}$$

This term accounts for the non-Markovian processes that are expected to be very important in a fluid made of identical particles, and is therefore crucial in the calculation of the time behavior of the said fluid. Furthermore, the term $R_{\mathbf{q}}(t)$ is defined as

$$R_{\mathbf{q}}(t) = e^{i\mathscr{Q}\mathscr{L}\mathscr{Q}t} i\mathscr{Q}\mathscr{L} g_{\mathbf{q}},$$

which is the force described earlier as the fluctuating and random effect coming through the many collisions experienced by the particles from their environment. $\mathscr{L}$ is the Liouville operator of the system, and $\mathscr{Q}$ is the projector on the space orthogonal to the slow variables, i.e., it effectively projects a given quantity on the subspace of the fast variables. Therefore we have

$$\mathscr{Q}R_{\mathbf{q}} = \mathscr{I} - \frac{\overline{\langle R_{\mathbf{q}} \delta\rho_{-\mathbf{q}} \rangle}}{NS^c(q)} \delta\rho_{\mathbf{q}} - \frac{\overline{\langle R_{\mathbf{q}} g_{-\mathbf{q}} \rangle}}{Nk_BTm} g_{\mathbf{q}},$$

where $\mathscr{I}$ is the identity operator.

Finally, we define $\mathbf{\Omega}(q)$ as an intrinsic frequency of the system, characterizing the short time dynamics:

$$\begin{aligned} i\mathbf{\Omega}(q) &= \overline{\left\langle \begin{bmatrix} \delta\dot{\rho}_{\mathbf{q}} \\ \dot{g}_{\mathbf{q}} \end{bmatrix} \cdot \begin{bmatrix} \delta\rho_{-\mathbf{q}} & g_{-\mathbf{q}} \end{bmatrix} \right\rangle} \left[\overline{\left\langle \begin{bmatrix} \delta\rho_{\mathbf{q}} \\ g_{\mathbf{q}} \end{bmatrix} \cdot \begin{bmatrix} \delta\rho_{-\mathbf{q}} & g_{-\mathbf{q}} \end{bmatrix} \right\rangle} \right]^{-1} \\ &= \begin{bmatrix} 0 & iNqk_BT \\ iNqk_BT & 0 \end{bmatrix} \begin{bmatrix} NS^c(q) & 0 \\ 0 & Nk_BTm \end{bmatrix}^{-1} \\ &= \begin{bmatrix} 0 & iNqk_BT \\ iNqk_BT & 0 \end{bmatrix} \begin{bmatrix} (NS^c(q))^{-1} & 0 \\ 0 & (Nk_BTm)^{-1} \end{bmatrix} \\ &= \begin{bmatrix} 0 & \dfrac{iq}{m} \\ iqk_BTS^c(q)^{-1} & 0 \end{bmatrix}. \end{aligned} \tag{4.9}$$

The point is here to derive an equation of motion for $F(q,t)$, the top left component of $\mathbf{C}(q,t)$ (equation (4.6). This function, otherwise called the density fluctuation autocorrelation function, or the ISF gives precious information about the relaxation process a fluid undergoes towards its final phase. Ultimately, the infinite time behavior of $F(q,t)$ defines the phase of the fluid, which is the main concern in the present work.

Inserting the expressions of $\mathbf{C}(q,t)$, $\mathbf{\Omega}(q,t)$ and $\mathbf{K}(q,t)$ into (4.7) leads to a matrix equation, whose evaluation would in theory enable the calculation of the top left component $F(q,t)$. However, the presence of a convolution product in the r.h.s. of equation (4.7) renders the latter extremely difficult. The solution comes from introducing the Laplace transform in the form of

$$\tilde{f}(z) = i\int_0^\infty dt e^{izt} f(t). \tag{4.10}$$

Applying it to equation (4.7), we find that

$$\begin{aligned} -iz \begin{bmatrix} \tilde{F}(q,z) & \tilde{C}^{\rho g}(q,z) \\ \tilde{C}^{g\rho}(q,z) & \tilde{C}^{gg}(q,z) \end{bmatrix} - i \begin{bmatrix} S^c(q) & 0 \\ 0 & k_BTm \end{bmatrix} = \\ \begin{bmatrix} 0 & \dfrac{iq}{m} \\ iqk_BTS^c(q)^{-1} & 0 \end{bmatrix} \begin{bmatrix} \tilde{F}(q,z) & \tilde{C}^{\rho g}(q,z) \\ \tilde{C}^{g\rho}(q,z) & \tilde{C}^{gg}(q,z) \end{bmatrix} \\ + i \begin{bmatrix} 0 & 0 \\ 0 & \tilde{M}(q,z) \end{bmatrix} \begin{bmatrix} \tilde{F}(q,z) & \tilde{C}^{\rho g}(q,z) \\ \tilde{C}^{g\rho}(q,z) & \tilde{C}^{gg}(q,z) \end{bmatrix}, \end{aligned} \tag{4.11}$$

which can be solved for $\tilde{F}(q,z)$:

$$-iz\tilde{F}(q,z) - iS^c(q) = \frac{iq}{m}\tilde{C}^{\rho g}(q,z). \tag{4.12}$$

This expression presents the term $\tilde{C}^{\rho g}(q,z)$ in its r.h.s., which can also be calculated using the Laplace transform of equation (4.11):

$$-iz\tilde{C}^{\rho g}(q,z) = iqk_BTS^c(q)^{-1}\tilde{F}(q,z) + i\tilde{M}(q,z)\tilde{C}^{\rho g}(q,z), \tag{4.13}$$

and ultimately, gathering these two equations,

$$\begin{aligned} -iz\left[-iz\tilde{F}(q,z) - iS^c(q)\right] &= \frac{iq}{m}\left[-iz\tilde{C}^{\rho g}(q,z)\right] \\ &= -\frac{q^2k_BT}{m}S^c(q)^{-1}\tilde{F}(q,z) + i\tilde{M}(q,z)\left[-iz\tilde{F}(q,z) - iS^c(q)\right]. \end{aligned} \tag{4.14}$$

After inverting the Laplace transforms of equation (4.14), one gets a Generalized Langevin Equation (GLE) for the density fluctuation autocorrelation function $F(q,t)$ alone:

$$\ddot{F}(q,t) + \Omega^2(q)F(q,t) + \int_0^t d\tau M(q,t-\tau)\dot{F}(q,\tau) = 0, \tag{4.15}$$

with $\Omega^2(q) = q^2k_BT/mS^c(q)$ and initial conditions $F(q,0) = S^c(q)$ and $\dot{F}(q,0) = 0$.

4.1.2 Mode Coupling Theory

The equation of motion that has just been derived takes the form of a GLE, and lies on the basis of a separation of the slow and fast variables. However, defining what is slow and what is fast solely on the basis of our intuition will not lead to a very rigorous separation. Therefore, the supposedly fast parts of the dynamics contained in the fluctuating random force $R_{\mathbf{q}}(t)$ will not necessarily be the fastest objects in the problem, and this can affect the quality of the calculated dynamics. The point of the Mode Coupling Theory (MCT) is to get a better separation of the fast and slow variables by considering quadratic contributions of the slow variables. These quadratic contributions are thought to contain some slow parts as well, though not as slow as the linear slow variables. The point is then to extract these quadratic slow variables from the random force, in order to include them in the memory function, and in this way proceed towards a better separation of fast and slows modes of the system.

We here define two terms quadratic with respect to the slow variables, in the form of

$$\begin{aligned} B_{\mathbf{q},\mathbf{k}} &= \delta\rho_{\mathbf{k}}\delta\rho_{\mathbf{q}-\mathbf{k}}, \\ C_{\mathbf{q},\mathbf{k}} &= \delta\rho_{\mathbf{k}}\langle\rho_{\mathbf{q}-\mathbf{k}}\rangle. \end{aligned} \tag{4.16}$$

The random force $R_{\mathbf{q}}$ and quadratic variables $B_{\mathbf{q},\mathbf{k}}$ and $C_{\mathbf{q},\mathbf{k}}$ have similar symmetry properties, and coupling them will allow to extract a remaining slow part of the random force (i.e., the slower parts of the fast term).
One might ask why the initial slow variable $g_{\mathbf{q}}$ has not been used to create quadratic variables in the form of either $D_{\mathbf{q},\mathbf{k}} = \delta\rho_{\mathbf{k}} g_{\mathbf{q},\mathbf{k}}$ or $E_{\mathbf{q},\mathbf{k}} = g_{\mathbf{k}} g_{\mathbf{q},\mathbf{k}}$. The reason for this lies in the symmetry of the slow variables in question. Indeed, $g_{\mathbf{q}}(t) = \sum_{j=1}^{N} \frac{\mathbf{q}}{q} \cdot \mathbf{p}_j(t) e^{i\,\mathbf{q}\,\mathbf{r}_j(t)}$ takes the form of a current, or a momentum, which under time reversal changes sign. $\delta\rho_{\mathbf{q}}$, however, remains unchanged under time reversal, as does the random force $R_{\mathbf{q}}$. Therefore, there is no coupling between $D_{\mathbf{q},\mathbf{k}}$ and the random force. Furthermore, the variable $E_{\mathbf{q},\mathbf{k}} = g_{\mathbf{k}} g_{\mathbf{q},\mathbf{k}}$ can be shown to be always ergodic, and therefore cannot contribute to a glass transition, which is still the main purpose of the MCT.
The corresponding slow part of $R_{\mathbf{q}}$ is obtained using the projection operator $\mathcal{P}$, defined as

$$\mathcal{P}R_{\mathbf{q}} = {\sum_{\mathbf{k}}}' \overline{\langle R_{\mathbf{q}} B_{-\mathbf{q},-\mathbf{k}} \rangle} G(\mathbf{q},\mathbf{k}) B_{\mathbf{q},\mathbf{k}} + \sum_{\mathbf{k}} \overline{\langle R_{\mathbf{q}} C_{-\mathbf{q},-\mathbf{k}} \rangle} H(\mathbf{q},\mathbf{k}) C_{\mathbf{q},\mathbf{k}}, \tag{4.17}$$

where we have anticipated the fact that, within the mode-coupling approximation, $\mathcal{P}$ is diagonal in $\mathbf{k}$ and the subspaces spanned by B and C are orthogonal. The matrices $G(\mathbf{q},\mathbf{k})$ and $H(\mathbf{q},\mathbf{k})$ insure the normalization of the projector:

$$\begin{aligned} \mathcal{P}B_{\mathbf{q},\mathbf{k}} &= B_{\mathbf{q},\mathbf{k}}, \\ \mathcal{P}C_{\mathbf{q},\mathbf{k}} &= C_{\mathbf{q},\mathbf{k}}. \end{aligned} \tag{4.18}$$

In the following, a mode coupling approximation is performed, in order to compute the following expressions:

$$\overline{\langle e^{i\mathcal{Q}\mathcal{L}\mathcal{Q}t} B_{\mathbf{q},\mathbf{k}} B_{-\mathbf{q},-\mathbf{k}} \rangle} = N^2 F(k,t) F(|\mathbf{q}-\mathbf{k}|,t), \tag{4.19}$$

$$\overline{\langle e^{i\mathcal{Q}\mathcal{L}\mathcal{Q}t} C_{\mathbf{q},\mathbf{k}} C_{-\mathbf{q},-\mathbf{k}} \rangle} = N^2 F(k,t) S^d(|\mathbf{q}-\mathbf{k}|), \tag{4.20}$$

$$\overline{\langle e^{i\mathcal{Q}\mathcal{L}\mathcal{Q}t} B_{\mathbf{q},\mathbf{k}} C_{-\mathbf{q},-\mathbf{k}} \rangle} = 0, \tag{4.21}$$

where $S^d(q)$ is the disconnected structure factor, defined as $S^d(q) = \rho h^d(q)$.
This allows for the calculation of the normalization functions $G(\mathbf{q},\mathbf{k})$ and $H(\mathbf{q},\mathbf{k})$:

$$G(\mathbf{q},\mathbf{k}) = N^{-2} S^c(k)^{-1} S^c(|\mathbf{q}-\mathbf{k}|)^{-1}, \tag{4.22}$$

$$H(\mathbf{q},\mathbf{k}) = N^{-2} S^c(k)^{-1} S^d(|\mathbf{q}-\mathbf{k}|)^{-1}. \tag{4.23}$$

It remains to obtain $\overline{\langle R_{\mathbf{q}} B_{-\mathbf{q},-\mathbf{k}} \rangle}$ and $\overline{\langle R_{\mathbf{q}} C_{-\mathbf{q},-\mathbf{k}} \rangle}$. Using the definition of $B_{\mathbf{q},\mathbf{k}}$ and $C_{\mathbf{q},\mathbf{k}}$, and the fact that $\mathcal{Q} = 1 - \mathcal{P}$, we can rewrite these two terms as

$$\overline{\langle R_{\mathbf{q}} B_{-\mathbf{q},-\mathbf{k}} \rangle} = \overline{\langle i\mathcal{Q}\mathcal{L} g_{\mathbf{q}} B_{-\mathbf{q},-\mathbf{k}} \rangle} = \overline{\langle i\mathcal{L} g_{\mathbf{q}} B_{-\mathbf{q},-\mathbf{k}} \rangle} - \overline{\langle i\mathcal{P}\mathcal{L} g_{\mathbf{q}} B_{-\mathbf{q},-\mathbf{k}} \rangle}, \tag{4.24}$$

$$\overline{\langle R_{\mathbf{q}} C_{-\mathbf{q},-\mathbf{k}} \rangle} = \overline{\langle i\mathcal{Q}\mathcal{L} g_{\mathbf{q}} C_{-\mathbf{q},-\mathbf{k}} \rangle} = \overline{\langle i\mathcal{L} g_{\mathbf{q}} C_{-\mathbf{q},-\mathbf{k}} \rangle} - \overline{\langle i\mathcal{P}\mathcal{L} g_{\mathbf{q}} C_{-\mathbf{q},-\mathbf{k}} \rangle}. \tag{4.25}$$

Using that $\{g_{\mathbf{q}}, \delta\rho_{-\mathbf{k}}\} = i\frac{\mathbf{q}\cdot\mathbf{k}}{q}\rho_{\mathbf{q}-\mathbf{k}}$ and $\{g_{\mathbf{q}}, \langle\rho_{-\mathbf{k}}\rangle\} = 0$, where $\{\dots\}$ denotes the Poisson brackets, let us calculate the first term on the r.h.s. of equation (4.24):

$$\begin{aligned}
\overline{\langle i\mathscr{L} g_{\mathbf{q}} B_{-\mathbf{q},-\mathbf{k}}\rangle} &= k_B T \overline{\langle\{g_{\mathbf{q}}, B_{-\mathbf{q},-\mathbf{k}}\}\rangle} \\
&= k_B T \left(\overline{\langle\{g_{\mathbf{q}}, \delta\rho_{-\mathbf{k}}\}\delta\rho_{-\mathbf{q}+\mathbf{k}}\rangle} + \overline{\langle\{g_{\mathbf{q}}, \delta\rho_{-\mathbf{q}+\mathbf{k}}\}\delta\rho_{-\mathbf{k}}\rangle}\right) \\
&= ik_B T\frac{\mathbf{q}}{q}\cdot\left[\mathbf{k}\overline{\langle\rho_{\mathbf{q}-\mathbf{k}}\delta\rho_{-\mathbf{q}+\mathbf{k}}\rangle} + (\mathbf{q}-\mathbf{k})\overline{\langle\rho_{\mathbf{k}}\delta\rho_{-\mathbf{k}}\rangle}\right] \\
&= iNqk_B T\left[\frac{\mathbf{q}\cdot\mathbf{k}}{q^2}S^c(|\mathbf{q}-\mathbf{k}|) + \frac{\mathbf{q}\cdot(\mathbf{q}-\mathbf{k})}{q^2}S^c(k)\right].
\end{aligned}$$

And similarly for equation (4.25):

$$\begin{aligned}
\overline{\langle i\mathscr{L} g_{\mathbf{q}} C_{-\mathbf{q},-\mathbf{k}}\rangle} &= k_B T\overline{\langle\{g_{\mathbf{q}}, C_{-\mathbf{q},-\mathbf{k}}\}\rangle} = k_B T\overline{\langle\{g_{\mathbf{q}}, \delta\rho_{-\mathbf{k}}\}\langle\rho_{-\mathbf{q}+\mathbf{k}}\rangle\rangle} \\
&= ik_B T\frac{\mathbf{q}}{q}\cdot\mathbf{k}\overline{\langle\rho_{\mathbf{q}-\mathbf{k}}\rangle\langle\rho_{-\mathbf{q}+\mathbf{k}}\rangle} \\
&= iNqk_B T\frac{\mathbf{q}\cdot\mathbf{k}}{q^2}S^d(|\mathbf{q}-\mathbf{k}|).
\end{aligned}$$

Terms of the form $\overline{\langle\delta\rho_{\mathbf{q}}\delta\rho_{-\mathbf{k}}\delta\rho_{-\mathbf{q}+\mathbf{k}}\rangle}$ are three body structure factors. Using the convolution approximation, these complex quantities can be expressed as products of two body structure factors that were defined in chapter 2:

$$\overline{\langle\delta\rho_{\mathbf{q}}\delta\rho_{-\mathbf{k}}\delta\rho_{-\mathbf{q}+\mathbf{k}}\rangle} = NS^c(q)S^c(k)S^c(|\mathbf{q}-\mathbf{k}|), \tag{4.26}$$

$$\overline{\langle\delta\rho_{\mathbf{q}}\delta\rho_{-\mathbf{k}}\rangle\langle\rho_{-\mathbf{q}+\mathbf{k}}\rangle} = NS^c(q)S^c(k)S^d(|\mathbf{q}-\mathbf{k}|). \tag{4.27}$$

The second terms on the r.h.s. of equation (4.24) and (4.25) is calculated as

$$\begin{aligned}
\overline{\langle i\mathscr{P}\mathscr{L} g_{\mathbf{q}} B_{-\mathbf{q},-\mathbf{k}}\rangle} &= \overline{\langle i\mathscr{L} g_{\mathbf{q}}\delta\rho_{-\mathbf{q}}\rangle}N^{-1}S^c(q)^{-1}\overline{\langle\delta\rho_{\mathbf{q}}\delta\rho_{-\mathbf{k}}\delta\rho_{-\mathbf{q}+\mathbf{k}}\rangle} \\
&= iNqk_B TS^c(k)S^c(|\mathbf{q}-\mathbf{k}|),
\end{aligned} \tag{4.28}$$

$$\begin{aligned}
\overline{\langle i\mathscr{P}\mathscr{L} g_{\mathbf{q}} C_{-\mathbf{q},-\mathbf{k}}\rangle} &= \overline{\langle i\mathscr{L} g_{\mathbf{q}}\delta\rho_{-\mathbf{q}}\rangle}N^{-1}S^c(q)^{-1}\overline{\langle\delta\rho_{\mathbf{q}}\delta\rho_{-\mathbf{k}}\langle\rho_{-\mathbf{q}+\mathbf{k}}\rangle\rangle} \\
&= iNqk_B TS^c(k)S^d(|\mathbf{q}-\mathbf{k}|),
\end{aligned} \tag{4.29}$$

using that

$$\overline{\langle i\mathscr{L} g_{\mathbf{q}}\delta\rho_{-\mathbf{q}}\rangle} = \overline{\langle\dot{g}_{\mathbf{q}}\delta\rho_{-\mathbf{q}}\rangle} = -\overline{\langle g_{\mathbf{q}}\delta\dot{\rho}_{-\mathbf{q}}\rangle} = \frac{iq}{m}\overline{\langle g_{\mathbf{q}}g_{-\mathbf{q}}\rangle} = iNqk_B T.$$

We define the vertices $V^{(2)}(\mathbf{q},\mathbf{k})$ and $V^{(1)}(\mathbf{q},\mathbf{k})$ as

$$V^{(2)}(\mathbf{q},\mathbf{k}) = \overline{\langle R_{\mathbf{q}}B_{-\mathbf{q},-\mathbf{k}}\rangle}G(\mathbf{q},\mathbf{k}), \tag{4.30}$$

$$V^{(1)}(\mathbf{q},\mathbf{k}) = \overline{\langle R_{\mathbf{q}}C_{-\mathbf{q},-\mathbf{k}}\rangle}H(\mathbf{q},\mathbf{k}), \tag{4.31}$$

such that

$$\mathcal{P}R_{\mathbf{q}} = {\sum_{\mathbf{k}}}' V^{(2)}(\mathbf{q},\mathbf{k}) B_{\mathbf{q},\mathbf{k}} + \sum_{\mathbf{k}} V^{(1)}(\mathbf{q},\mathbf{k}) C_{\mathbf{q},\mathbf{k}}, \tag{4.32}$$

which can now be computed:

$$\begin{aligned}
V^{(2)}(\mathbf{q},\mathbf{k}) =& \frac{iqk_BT}{N}\left[\frac{\mathbf{q}\cdot\mathbf{k}}{q^2}S^c(|\mathbf{q}-\mathbf{k}|) + \frac{\mathbf{q}\cdot(\mathbf{q}-\mathbf{k})}{q^2}S^c(k) - S^c(k)S^c(|\mathbf{q}-\mathbf{k}|)\right] \\
& S^c(k)^{-1}S^c(|\mathbf{q}-\mathbf{k}|)^{-1} \\
=& \frac{iqk_BT}{N}\left[\frac{\mathbf{q}\cdot\mathbf{k}}{q^2}S^c(k)^{-1} + \frac{\mathbf{q}\cdot(\mathbf{q}-\mathbf{k})}{q^2}S^c(|\mathbf{q}-\mathbf{k}|)^{-1} - 1\right] \\
=& -\frac{iqk_BT}{N}\rho\left[\frac{\mathbf{q}\cdot\mathbf{k}}{q^2}c^c(k) + \frac{\mathbf{q}\cdot(\mathbf{q}-\mathbf{k})}{q^2}c^c(|\mathbf{q}-\mathbf{k}|)\right], \\
V^{(1)}(\mathbf{q},\mathbf{k}) =& \frac{iqk_BT}{N}\sum\left[\frac{\mathbf{q}\cdot\mathbf{k}}{q^2}S^d(|\mathbf{q}-\mathbf{k}|) - S^c(k)S^d(|\mathbf{q}-\mathbf{k}|)\right] S^c(k)^{-1}S^d(|\mathbf{q}-\mathbf{k}|)^{-1} \\
=& \frac{iqk_BT}{N}\left[\frac{\mathbf{q}\cdot\mathbf{k}}{q^2}S^c(k)^{-1} - 1\right] \\
=& -\frac{iqk_BT}{N}\rho\left[\frac{\mathbf{q}\cdot\mathbf{k}}{q^2}c^c(k) + \frac{\mathbf{q}\cdot(\mathbf{q}-\mathbf{k})}{q^2}\frac{1}{\rho}\right].
\end{aligned}$$

We have now the expression of $\mathcal{P}R_{\mathbf{q}}$,

$$\begin{aligned}
\mathcal{P}R_{\mathbf{q}} = -\frac{iqk_BT}{N}\rho{\sum_{\mathbf{k}}}'\sum\left[\frac{\mathbf{q}\cdot\mathbf{k}}{q^2}c^c(k) + \frac{\mathbf{q}\cdot(\mathbf{q}-\mathbf{k})}{q^2}c^c(|\mathbf{q}-\mathbf{k}|)\right] B_{\mathbf{q},\mathbf{k}} \\
- \frac{iqk_BT}{N}\rho\sum_{\mathbf{k}}\sum\left[\frac{\mathbf{q}\cdot\mathbf{k}}{q^2}c^c(k) + \frac{\mathbf{q}\cdot(\mathbf{q}-\mathbf{k})}{q^2}\frac{1}{\rho}\right] C_{\mathbf{q},\mathbf{k}},
\end{aligned} \tag{4.33}$$

and we can complete the calculation of $M^{(\mathrm{MC})}(q,t)$,

$$M^{(\mathrm{MC})}(q,t) = \frac{\overline{\langle \mathcal{P}R_{\mathbf{q}}(t)\,\mathcal{P}R_{-\mathbf{q}}\rangle}}{Nk_BTm}, \tag{4.34}$$

which can be split into two parts,

$$M^{(\mathrm{MC})}(q,t) = M^{(2)}(q,t) + M^{(1)}(q,t), \tag{4.35}$$

with

$$\begin{aligned}
M^{(2)}(q,t) = \frac{1}{2}\rho\frac{q^2k_BT}{m}\frac{1}{V}\sum_{\mathbf{k}}\left[\frac{\mathbf{q}\cdot\mathbf{k}}{q^2}c^c(k) + \frac{\mathbf{q}\cdot(\mathbf{q}-\mathbf{k})}{q^2}c^c(|\mathbf{q}-\mathbf{k}|)\right]^2 \\
F(k,t)F(|\mathbf{q}-\mathbf{k}|,t)
\end{aligned} \tag{4.36}$$

and

$$M^{(1)}(q,t) = \rho \frac{q^2 k_B T}{m} \frac{1}{V} \sum_{\mathbf{k}} \left[\frac{\mathbf{q}\cdot\mathbf{k}}{q^2} c^c(k) + \frac{\mathbf{q}\cdot(\mathbf{q}-\mathbf{k})}{q^2} \frac{1}{\rho} \right]^2 F(k,t) S^d(|\mathbf{q}-\mathbf{k}|). \quad (4.37)$$

Dividing the generalized Langevin equation (4.15) by $S^c(q)$, we get the equation for the normalized ISF $\phi(q,t)$:

$$\ddot{\phi}(q,t) + \Omega(q)^2 \phi(q,t) + \Omega(q)^2 \int_0^t d\tau m(q,t-\tau)\dot{\phi}(q,\tau) = 0, \quad (4.38)$$

with initial conditions $\phi(q,0) = 1$ and $\dot{\phi}(q,0) = 0$, and

$$\Omega(q)^2 = \frac{q^2 k_B T}{m S^c(q)}. \quad (4.39)$$

Taking advantage of the fact that the long time dynamics predicted by the MCT are essentially independent from the short time dynamics, the overdamped limit (Franosch *et al.*, 1997a; Fuchs *et al.*, 1998; Franosch *et al.*, 1997b) is adopted for simplicity. It allows for a rewriting of the generalized Langevin equation applied to the case of the Brownian dynamics, effectively ruling out the friction coefficient as a parameter of the equation:

$$\tau(q)\dot{\phi}(q,t) + \phi(q,t) + \int_0^t d\tau m(q,t-\tau)\dot{\phi}(q,\tau) = 0, \quad (4.40)$$

with initial condition $\phi(q,0) = 1$ and

$$\tau_q = \frac{S^c(q)}{D_0 q^2}, \quad (4.41)$$

where D_0 is the short time diffusivity, and the memory functions:

$$m^{(2)}(q,t) = \frac{1}{2}\rho S^c(q) \frac{1}{V} \sum_{\mathbf{k}} \left[\frac{\mathbf{q}\cdot\mathbf{k}}{q^2} c^c(k) + \frac{\mathbf{q}\cdot(\mathbf{q}-\mathbf{k})}{q^2} c^c(|\mathbf{q}-\mathbf{k}|) \right]^2 S^c(k) S^c(|\mathbf{q}-\mathbf{k}|)\phi(k,t)\phi(|\mathbf{q}-\mathbf{k}|,t), \quad (4.42)$$

$$m^{(1)}(q,t) = \rho S^c(q) \frac{1}{V} \sum_{\mathbf{k}} \left[\frac{\mathbf{q}\cdot\mathbf{k}}{q^2} c^c(k) + \frac{\mathbf{q}\cdot(\mathbf{q}-\mathbf{k})}{q^2} \frac{1}{\rho} \right]^2 S^c(k) S^d(|\mathbf{q}-\mathbf{k}|)\phi(k,t). \quad (4.43)$$

Often in the case of dynamical slowing down, one might be interested in the infinite time limit of the ISF. As it will be explicited in chapter 5, by giving the simple picture of the

fully relaxed fluid, this quantity is used to define its phase, and ultimately draw a phase diagram. The infinite time limit of the ISF is denoted by

$$f(q) = \lim_{t\to\infty} \phi(q,t), \tag{4.44}$$

which can be expressed, by manipulating equation (4.40), as

$$\frac{f(q)}{1-f(q)} = \lim_{t\to\infty} m(q,t) = m(q). \tag{4.45}$$

4.2 Self dynamics

4.2.1 Generalized Langevin Equation

The case of the self dynamics, or tagged particle dynamics, can be a particularly illuminating one, bringing informations about the phenomena happening at the scale of one specific particle rather than the whole fluid. Furthermore, the self ISF is the basis for the development of more complex dynamical quantities, such as the mean squared displacement (MSD), the local exponent and the non-Gaussian parameter, which will be used to characterize the dynamics in the following chapter.

One possible development of a GLE for this type of quantity follows the same path as for the collective ISF, considering the tagged particle density instead of the collective one, for a particle of the same species as previously:

$$\rho^s_{\mathbf{q}}(t) = e^{i\mathbf{q}\mathbf{r}(t)}, \tag{4.46}$$

and

$$g^s_{\mathbf{q}}(t) = \frac{\mathbf{q}}{q}\cdot\mathbf{p}(t)e^{i\,\mathbf{q}\,\mathbf{r}(t)}, \tag{4.47}$$

where $\mathbf{r}$ is the position of the tagged particle and $\mathbf{p}$ is its momentum.

We obtain the Fourier transforms of the total correlation functions as

$$\overline{\langle \rho^s_{\mathbf{q}}\delta\rho_{-\mathbf{q}}\rangle} = \rho h^c(q),$$
$$\overline{\langle \rho^s_{\mathbf{q}}\langle\rho_{-\mathbf{q}}\rangle\rangle} = \rho h^d(q).$$

The self density fluctuation autocorrelation function (or self ISF) is expressed as

$$\phi^s(q,t) = \overline{\langle \rho^s_{\mathbf{q}}(t)\rho^s_{-\mathbf{q}}\rangle}, \tag{4.48}$$

and finally, the GLE is obtained as

$$\ddot{\phi}^s(q,t) + \omega^2(q)\phi^s(q,t) + \int_0^t d\tau M^s(q,t-\tau)\dot{\phi}^s(q,\tau) = 0, \tag{4.49}$$

with initial conditions $\phi^s(q,0)=1$, $\dot{\phi}^s(q,0)=0$, and

$$\omega^2(q)=\frac{q^2k_BT}{m}.$$

The memory function $M^s(q,t)$ is given by

$$M^s(q,t)=\frac{\overline{\langle r_{\mathbf{q}}(t)\, r_{-\mathbf{q}}\rangle}}{mk_BT},$$

where

$$r_{\mathbf{q}}(t)=e^{i\mathscr{Q}_s\mathscr{L}_s\mathscr{Q}_st}i\mathscr{Q}_s\mathscr{L}_sg^s_{\mathbf{q}}$$

is the random force. $\mathscr{L}_s$ is the Liouville operator of the system and $\mathscr{Q}_s$ is the projector on the space of the fast variables, i.e., orthogonal to $\rho^s_{\mathbf{q}}$ and $g^s_{\mathbf{q}}$:

$$\mathscr{Q}_sr_{\mathbf{q}}=\mathscr{I}-\overline{\langle r_{\mathbf{q}}\rho^s_{-\mathbf{q}}\rangle}\rho^s_{\mathbf{q}}-\frac{\overline{\langle r_{\mathbf{q}}g^s_{-\mathbf{q}}\rangle}}{mk_BT}g^s_{\mathbf{q}},$$

where $\mathscr{I}$ is the identity operator.

4.2.2 Mode coupling Theory

We define the quadratic terms in form of

$$\begin{aligned} b_{\mathbf{q},\mathbf{k}}&=\rho^s_{\mathbf{k}}\delta\rho_{\mathbf{q}-\mathbf{k}},\\ c_{\mathbf{q},\mathbf{k}}&=\rho^s_{\mathbf{k}}\langle\rho_{\mathbf{q}-\mathbf{k}}\rangle. \end{aligned} \tag{4.50}$$

The random force $r_{\mathbf{q}}$ and quadratic variables have similar symmetry properties and might therefore be coupled.
Knowing that within the mode-coupling approximation, $\mathcal{P}_s$ is diagonal in $\mathbf{k}$ and that the subspaces spanned by the bs and cs are orthogonal, the corresponding slow part of $r_{\mathbf{q}}$ can be obtained using the projector operator $\mathcal{P}_s$:

$$\mathcal{P}_sr_{\mathbf{q}}=\sum_{\mathbf{k}}\overline{\langle r_{\mathbf{q}}b_{-\mathbf{q},-\mathbf{k}}\rangle}g(\mathbf{q},\mathbf{k})b_{\mathbf{q},\mathbf{k}}+\sum_{\mathbf{k}}\overline{\langle r_{\mathbf{q}}c_{-\mathbf{q},-\mathbf{k}}\rangle}h(\mathbf{q},\mathbf{k})c_{\mathbf{q},\mathbf{k}}$$

The matrices $g(\mathbf{q},\mathbf{k})$ and $h(\mathbf{q},\mathbf{k})$ insure normalization:

$$\begin{aligned} \mathcal{P}_sb_{\mathbf{q},\mathbf{k}}&=b_{\mathbf{q},\mathbf{k}},\\ \mathcal{P}_sc_{\mathbf{q},\mathbf{k}}&=c_{\mathbf{q},\mathbf{k}}. \end{aligned} \tag{4.51}$$

A mode coupling approximation is performed by setting

$$\begin{aligned} \overline{\langle e^{i\mathscr{Q}_s\mathscr{L}_s\mathscr{Q}_st}b_{\mathbf{q},\mathbf{k}}b_{-\mathbf{q},-\mathbf{k}}\rangle}&=NS^c(|\mathbf{q}-\mathbf{k}|)\phi^s(k,t)\phi(|\mathbf{q}-\mathbf{k}|,t),\\ \overline{\langle e^{i\mathscr{Q}_s\mathscr{L}_s\mathscr{Q}_st}c_{\mathbf{q},\mathbf{k}}c_{-\mathbf{q},-\mathbf{k}}\rangle}&=NS^d(|\mathbf{q}-\mathbf{k}|)\phi^s(k,t). \end{aligned}$$

This allows to calculate $g(\mathbf{q},\mathbf{k})$ and $h(\mathbf{q},\mathbf{k})$,

$$g(\mathbf{q},\mathbf{k}) = [NS^c(|\mathbf{q}-\mathbf{k}|)]^{-1},$$
$$h(\mathbf{q},\mathbf{k}) = [NS^d(|\mathbf{q}-\mathbf{k}|)]^{-1}.$$

It remains to obtain

$$\overline{\langle r_{\mathbf{q}} b_{-\mathbf{q},-\mathbf{k}}\rangle} = \overline{\langle i\mathscr{Q}_s\mathscr{L}_s g^s_{\mathbf{q}} b_{-\mathbf{q},-\mathbf{k}}\rangle} = \overline{\langle i\mathscr{L}_s g^s_{\mathbf{q}} b_{-\mathbf{q},-\mathbf{k}}\rangle} - \overline{\langle i\mathscr{P}_s\mathscr{L}_s g^s_{\mathbf{q}} b_{-\mathbf{q},-\mathbf{k}}\rangle}, \tag{4.52}$$
$$\overline{\langle r_{\mathbf{q}} c_{-\mathbf{q},-\mathbf{k}}\rangle} = \overline{\langle i\mathscr{Q}_s\mathscr{L}_s g^s_{\mathbf{q}} c_{-\mathbf{q},-\mathbf{k}}\rangle} = \overline{\langle i\mathscr{L}_s g^s_{\mathbf{q}} c_{-\mathbf{q},-\mathbf{k}}\rangle} - \overline{\langle i\mathscr{P}_s\mathscr{L}_s g^s_{\mathbf{q}} c_{-\mathbf{q},-\mathbf{k}}\rangle}. \tag{4.53}$$

Using that $\{g^s_{\mathbf{q}}, \rho^s_{-\mathbf{k}}\} = i\frac{\mathbf{q}\cdot\mathbf{k}}{q}\rho^s_{\mathbf{q}-\mathbf{k}}$ and $\{g^s_{\mathbf{q}}, \delta\rho_{-\mathbf{k}}\} = \{g^s_{\mathbf{q}}, \langle\rho_{-\mathbf{k}}\rangle\} = 0$, we calculate the first term on the r.h.s. of equations (4.52) and (4.53):

$$\begin{aligned}
\overline{\langle i\mathscr{L}_s g^s_{\mathbf{q}} b_{-\mathbf{q},-\mathbf{k}}\rangle} &= k_BT\overline{\langle\{g^s_{\mathbf{q}}, b_{-\mathbf{q},-\mathbf{k}}\}\rangle} = k_BT\left(\overline{\langle\{g^s_{\mathbf{q}}, \rho^s_{-\mathbf{k}}\}\delta\rho_{-\mathbf{q}+\mathbf{k}}\rangle} + \overline{\langle\{g^s_{\mathbf{q}}, \delta\rho_{-\mathbf{q}+\mathbf{k}}\}\rho^s_{-\mathbf{k}}\rangle}\right)\\
&= ik_BT\frac{\mathbf{q}\cdot\mathbf{k}}{q}\overline{\langle\rho^s_{\mathbf{q}-\mathbf{k}}\delta\rho_{-\mathbf{q}+\mathbf{k}}\rangle} = iqk_BT\rho\frac{\mathbf{q}\cdot\mathbf{k}}{q^2}h^c(|\mathbf{q}-\mathbf{k}|),\\
\overline{\langle i\mathscr{L}_s g^s_{\mathbf{q}} c_{-\mathbf{q},-\mathbf{k}}\rangle} &= k_BT\overline{\langle\{g^s_{\mathbf{q}}, c_{-\mathbf{q},-\mathbf{k}}\}\rangle} = k_BT\overline{\langle\{g^s_{\mathbf{q}}, \rho^s_{-\mathbf{k}}\}\langle\rho_{-\mathbf{q}+\mathbf{k}}\rangle\rangle}\\
&= iqk_BT\rho\frac{\mathbf{q}\cdot\mathbf{k}}{q^2}h^d(|\mathbf{q}-\mathbf{k}|).
\end{aligned}$$

And using that $\overline{\langle i\mathscr{L}_s g^s_{\mathbf{q}}\rho^s_{-\mathbf{q}}\rangle} = \overline{\langle\dot{g}^s_{\mathbf{q}}\rho^s_{-\mathbf{q}}\rangle} = -\overline{\langle g^s_{\mathbf{q}}\dot{\rho}^s_{-\mathbf{q}}\rangle} = \frac{iq}{m_s}\overline{\langle g^s_{\mathbf{q}} g^s_{-\mathbf{q}}\rangle} = iqk_BT$, we calculate the second terms as well:

$$\begin{aligned}
\overline{\langle i\mathscr{P}_s\mathscr{L}_s g^s_{\mathbf{q}} b_{-\mathbf{q},-\mathbf{k}}\rangle} &= \overline{\langle i\mathscr{L}_s g^s_{\mathbf{q}}\rho^s_{-\mathbf{q}}\rangle}\cdot\overline{\langle\rho^s_{\mathbf{q}}\rho^s_{-\mathbf{k}}\delta\rho_{-\mathbf{q}+\mathbf{k}}\rangle} = iqk_BT\rho h^c(|\mathbf{q}-\mathbf{k}|),\\
\overline{\langle i\mathscr{P}_s\mathscr{L}_s g^s_{\mathbf{q}} c_{-\mathbf{q},-\mathbf{k}}\rangle} &= \overline{\langle i\mathscr{L}_s g^s_{\mathbf{q}}\rho^s_{-\mathbf{q}}\rangle}\cdot\overline{\langle\rho^s_{\mathbf{q}}\rho^s_{-\mathbf{k}}\langle\rho_{-\mathbf{q}+\mathbf{k}}\rangle\rangle} = iqk_BT\rho h^d(|\mathbf{q}-\mathbf{k}|).
\end{aligned}$$

We define the vertices

$$v^{(2)}(\mathbf{q},\mathbf{k}) = \overline{\langle r_{\mathbf{q}} b_{-\mathbf{q},-\mathbf{k}}\rangle}g(\mathbf{q},\mathbf{k}),$$
$$v^{(1)}(\mathbf{q},\mathbf{k}) = \overline{\langle r_{\mathbf{q}} c_{-\mathbf{q},-\mathbf{k}}\rangle}h(\mathbf{q},\mathbf{k}),$$

such that

$$\mathcal{P}_s r_{\mathbf{q}} = \sum_{\mathbf{k}} v^{(2)}(\mathbf{q},\mathbf{k})b_{\mathbf{q},\mathbf{k}} + \sum_{\mathbf{k}} v^{(1)}(\mathbf{q},\mathbf{k})c_{\mathbf{q},\mathbf{k}}.$$

They can be computed as

$$v^{(2)}(\mathbf{q},\mathbf{k}) = iqk_BT\frac{1}{V}\left[\frac{\mathbf{q}\cdot\mathbf{k}}{q^2} - 1\right]\frac{h^c(|\mathbf{q}-\mathbf{k}|)}{S^c(|\mathbf{q}-\mathbf{k}|)}$$
$$v^{(1)}(\mathbf{q},\mathbf{k}) = iqk_BT\frac{1}{V}\left[\frac{\mathbf{q}\cdot\mathbf{k}}{q^2} - 1\right]\frac{h^d(|\mathbf{q}-\mathbf{k}|)}{S^d(|\mathbf{q}-\mathbf{k}|)},$$

and one completes the calculation of $M^{s(\mathrm{MC})}(q,t)$, which can be split into two parts:

$$M^{s(\mathrm{MC})}(q,t) = M^{s(2)}(q,t) + M^{s(1)}(q,t).$$

The quadratic part $M^{s(2)}(q,t)$ is given by

$$M^{s(2)}(q,t) = \frac{q^2 k_B T \rho}{m} \frac{1}{V} \sum_{\mathbf{k}} \left[\frac{\mathbf{q}\cdot(\mathbf{q}-\mathbf{k})}{q^2} \right]^2 \frac{[h^c(|\mathbf{q}-\mathbf{k}|)]^2}{S^c(|\mathbf{q}-\mathbf{k}|)} \phi(|\mathbf{q}-\mathbf{k}|,t)\phi^s(k,t),$$

and the linear part $M^{s(1)}(q,t)$ by

$$M^{s(1)}(q,t) = \frac{q^2 k_B T}{m} \frac{1}{V} \sum_{\mathbf{k}} \left[\frac{\mathbf{q}\cdot(\mathbf{q}-\mathbf{k})}{q^2} \right]^2 h^d(|\mathbf{q}-\mathbf{k}|)\phi^s(k,t).$$

Now, using the replica Ornstein-Zernike equations, defined in chapter 2, we can write the kernels as

$$M^{s(2)}(q,t) = \frac{q^2 k_B T \rho}{m} \frac{1}{V} \sum_{\mathbf{k}} \left[\frac{\mathbf{q}\cdot(\mathbf{q}-\mathbf{k})}{q^2} c^c(|\mathbf{q}-\mathbf{k}|) \right]^2 S^c(|\mathbf{q}-\mathbf{k}|)\phi(|\mathbf{q}-\mathbf{k}|,t)\phi^s(k,t)$$

and

$$M^{s(1)}(q,t) = \frac{q^2 k_B T}{m} \frac{1}{V} \sum_{\mathbf{k}} \left[\frac{\mathbf{q}\cdot(\mathbf{q}-\mathbf{k})}{q^2} \right]^2 h^d(|\mathbf{q}-\mathbf{k}|)\phi^s(k,t).$$

Applying the overdamped limit to equation (4.49), its Brownian version reads

$$\tau^s(q)\dot{\phi}^s(q,t) + \phi^s(q,t) + \int_0^t d\tau m^s(q,t-\tau)\dot{\phi}^s(q,\tau) = 0, \tag{4.54}$$

where $\tau^s(q) = 1/D_0 q^2$ and the memory kernels are

$$m^{s(2)}(q,t) = \rho \frac{1}{V} \sum_{\mathbf{k}} \left[\frac{\mathbf{q}\cdot(\mathbf{q}-\mathbf{k})}{q^2} c^c(|\mathbf{q}-\mathbf{k}|) \right]^2 S^c(|\mathbf{q}-\mathbf{k}|)\phi(|\mathbf{q}-\mathbf{k}|,t)\phi^s(k,t)$$

and

$$m^{s(1)}(q,t) = \frac{1}{V} \sum_{\mathbf{k}} \left[\frac{\mathbf{q}\cdot(\mathbf{q}-\mathbf{k})}{q^2} \right]^2 h^d(|\mathbf{q}-\mathbf{k}|)\phi^s(k,t).$$

Finally, the infinite time limit of the self ISF can be computed as

$$\frac{f^s(q)}{1-f^s(q)} = \lim_{t\to\infty} m^s(q,t) = m^s(q), \tag{4.55}$$

where

$$f^s(q) = \lim_{t\to\infty} \phi^s(q,t). \tag{4.56}$$

4.3 Mean squared and quartic displacements

We start with equation (4.48) for the self-dynamics, where the self ISF can actually be expanded in the following way, in the limit of $q \to 0$:

$$\phi^s(q,t) = 1 - \frac{q^2}{6}\delta r^2(t) + \frac{q^4}{120}\delta r^4(t) + o(q^4), \tag{4.57}$$

where $\delta r^2(t)$ is the MSD, and $\delta r^4(t)$ is the mean quartic displacement (MQD). These two quantities allow the evaluation of the non-Gaussian parameter (NGP) as

$$\alpha = \frac{3}{5}\frac{\delta r^4(t)}{(\delta r^2(t))^2} - 1. \tag{4.58}$$

The NGP and the MSD are two very important indicators of the diffusivity regime of the system, and will be at the core of the understanding of the results presented in chapter 5.

The point of the following is to be able to expand the memory function in the limit of $q \to 0$ as well in order to adapt the GLE, and by suitably identifying the terms, derive a GLE that, within the MCT framework will allow for a calculation of the MSD, the MQD and the NGP. We define the quantity $M^s(q,t) = q^2 m^s(q,t)$, and get

$$M^s(q,t) = q^2 \int_{\mathbf{k}} \left[v^{(2)}(\mathbf{q},\mathbf{k})\phi^s(k,t)\phi(|\mathbf{q}-\mathbf{k}|,t) + v^{(1)}(\mathbf{q},\mathbf{k})\phi^s(k,t) \right], \tag{4.59}$$

such that

$$\begin{aligned} M^s(q,t) =& q^2 \int_{\mathbf{k}} \left\{ \rho \left[\frac{\mathbf{q}\cdot(\mathbf{q}-\mathbf{k})}{q^2} \right]^2 [c^c(|\mathbf{q}-\mathbf{k}|)]^2 S^c(|\mathbf{q}-\mathbf{k}|)\phi^s(k,t)\phi(|\mathbf{q}-\mathbf{k}|,t) \right. \\ & \left. + \left[\frac{\mathbf{q}\cdot(\mathbf{q}-\mathbf{k})}{q^2} \right]^2 h^d(|\mathbf{q}-\mathbf{k}|)\phi^s(k,t) \right\} \\ =& q^2 \int_{\mathbf{k}} \left[\frac{\mathbf{q}\cdot(\mathbf{q}-\mathbf{k})}{q^2} \right]^2 \left\{ \rho \left[c^c(|\mathbf{q}-\mathbf{k}|) \right]^2 S^c(|\mathbf{q}-\mathbf{k}|)\phi(|\mathbf{q}-\mathbf{k}|,t) \right. \\ & \left. + h^d(|\mathbf{q}-\mathbf{k}|) \right\} \phi^s(k,t). \end{aligned} \tag{4.60}$$

By exchanging $\mathbf{k}$ and $\mathbf{q}-\mathbf{k}$, we get

$$\begin{aligned} M^s(q,t) &= \int_{\mathbf{k}} \left[\frac{\mathbf{q}\cdot\mathbf{k}}{q} \right]^2 \left\{ \rho \left[c^c(k) \right]^2 S^c(k)\phi(k,t) + h^d(k) \right\} \phi^s(|\mathbf{q}-\mathbf{k}|,t) \\ &= \int_{\mathbf{k}} (\mathbf{e}_\mathbf{q}\cdot\mathbf{k})^2 \left\{ \rho \left[c^c(k) \right]^2 S^c(k)\phi(k,t) + h^d(k) \right\} \phi^s(|\mathbf{q}-\mathbf{k}|,t) \\ &= \int_{\mathbf{k}} (\mathbf{e}_\mathbf{q}\cdot\mathbf{e}_\mathbf{k})^2 W(k,t)\phi^s(|\mathbf{q}-\mathbf{k}|,t), \end{aligned} \tag{4.61}$$

with $W(k,t) = k^2 \left\{ \rho \left[c^c(k)\right]^2 S^c(k) \phi(k,t) + h^d(k) \right\}$.
The integral on the r.h.s. of equation (4.61) presents the term $\phi^s(|\mathbf{q}-\mathbf{k}|,t)$, that we need to expand in the limit $q \to 0$, in order to expand $M^s(q,t)$ as well:

$$\begin{aligned}\phi^s(|\mathbf{q}-\mathbf{k}|,t) =& \phi^s(|\mathbf{k}-\mathbf{q}|,t) = \phi^s\left(\sqrt{\sum_\gamma (k_\gamma - q_\gamma)^2}, t\right) \\ =& \phi^s(k,t) + \sum_\alpha (-q_\alpha) \frac{\partial \phi^s(k,t)}{\partial k_\alpha} + \frac{1}{2}\sum_\alpha \sum_\beta q_\alpha q_\beta \frac{\partial^2 \phi^s(k,t)}{\partial k_\alpha \partial k_\beta} + o(q^2).\end{aligned} \tag{4.62}$$

Using that $\dfrac{\partial k}{\partial k_\alpha} = \dfrac{k_\alpha}{k}$, we get

$$\frac{\partial \phi^s(k,t)}{\partial k_\alpha} = \frac{\partial k}{\partial k_\alpha}\frac{\partial \phi^s(k,t)}{\partial k} = \frac{k_\alpha}{k}\frac{\partial \phi^s(k,t)}{\partial k}, \tag{4.63}$$

$$\begin{aligned}\frac{\partial^2 \phi^s(k,t)}{\partial k_\alpha \partial k_\beta} &= \frac{\partial}{\partial k_\alpha}\left[\frac{k_\beta}{k}\frac{\partial \phi^s(k,t)}{\partial k}\right] \\ &= \left[\frac{\delta_{\alpha\beta}}{k} - \frac{k_\beta}{k^2}\frac{\partial k}{\partial k_\alpha}\right]\frac{\partial \phi^s(k,t)}{\partial k} + \frac{k_\beta}{k}\frac{\partial}{\partial k_\alpha}\frac{\partial \phi^s(k,t)}{\partial k} \\ &= \left[\frac{\delta_{\alpha\beta}}{k} - \frac{k_\alpha k_\beta}{k^3}\right]\frac{\partial \phi^s(k,t)}{\partial k} + \frac{k_\beta}{k}\frac{\partial k}{\partial k_\alpha}\frac{\partial^2 \phi^s(k,t)}{\partial k^2} \\ &= \left[\frac{\delta_{\alpha\beta}}{k} - \frac{k_\alpha k_\beta}{k^3}\right]\frac{\partial \phi^s(k,t)}{\partial k} + \frac{k_\alpha k_\beta}{k^2}\frac{\partial^2 \phi^s(k,t)}{\partial k^2},\end{aligned} \tag{4.64}$$

which allows one to compute $\phi^s(|\mathbf{q}-\mathbf{k}|,t)$:

$$\begin{aligned}&\phi^s(|\mathbf{q}-\mathbf{k}|,t) = \\ &\quad \phi^s(k,t) - \sum_\alpha q_\alpha \frac{k_\alpha}{k}\frac{\partial \phi^s(k,t)}{\partial k} \\ &\quad + \frac{1}{2}\sum_\alpha \sum_\beta q_\alpha q_\beta \left\{ \left[\frac{\delta_{\alpha\beta}}{k} - \frac{k_\alpha k_\beta}{k^3}\right]\frac{\partial \phi^s(k,t)}{\partial k} + \frac{k_\alpha k_\beta}{k^2}\frac{\partial^2 \phi^s(k,t)}{\partial k^2} \right\} + o(q^2) \\ &= \phi^s(k,t) - \frac{\mathbf{q}\cdot\mathbf{k}}{k}\frac{\partial \phi^s(k,t)}{\partial k} \\ &\quad + \frac{1}{2}\left\{ \left[\frac{q^2}{k} - \frac{(\mathbf{q}\cdot\mathbf{k})^2}{k^3}\right]\frac{\partial \phi^s(k,t)}{\partial k} + \frac{(\mathbf{q}\cdot\mathbf{k})^2}{k^2}\frac{\partial^2 \phi^s(k,t)}{\partial k^2} \right\} + o(q^2) \\ &= \phi^s(k,t) - q\mathbf{e_q}\cdot\mathbf{e_k}\frac{\partial \phi^s(k,t)}{\partial k} \\ &\quad + \frac{1}{2}q^2\left[\frac{1-(\mathbf{e_q}\cdot\mathbf{e_k})^2}{k}\frac{\partial \phi^s(k,t)}{\partial k} + (\mathbf{e_q}\cdot\mathbf{e_k})^2\frac{\partial^2 \phi^s(k,t)}{\partial k^2}\right] + o(q^2),\end{aligned} \tag{4.65}$$

that we can insert into equation (4.61):

$$\begin{aligned}
M^s(q,t) =& \int_{\mathbf{k}} (\mathbf{e_q}\cdot\mathbf{e_k})^2 W(k,t)\left\{\phi^s(k,t) - q\mathbf{e_q}\cdot\mathbf{e_k}\frac{\partial\phi^s(k,t)}{\partial k}\right.\\
&\left.+\frac{1}{2}q^2\left[\frac{1-(\mathbf{e_q}\cdot\mathbf{e_k})^2}{k}\frac{\partial\phi^s(k,t)}{\partial k} + (\mathbf{e_q}\cdot\mathbf{e_k})^2\frac{\partial^2\phi^s(k,t)}{\partial k^2}\right] + o(q^2)\right\}\\
=&\frac{1}{D}\int_{\mathbf{k}} W(k,t)\phi^s(k,t) + \frac{1}{2}q^2\int_{\mathbf{k}} W(k,t)\left[\left(\frac{1}{D} - \frac{3}{D(D+2)}\right)\frac{1}{k}\frac{\partial\phi^s(k,t)}{\partial k}\right.\\
&\left.+\frac{3}{D(D+2)}\frac{\partial^2\phi^s(k,t)}{\partial k^2}\right] + o(q^2)\\
=&\frac{1}{D}\int_{\mathbf{k}} W(k,t)\phi^s(k,t) + \frac{1}{2}q^2\frac{1}{D(D+2)}\int_{\mathbf{k}} W(k,t)\left[\frac{D-1}{k}\frac{\partial\phi^s(k,t)}{\partial k}\right.\\
&\left.+3\frac{\partial^2\phi^s(k,t)}{\partial k^2}\right] + o(q^2)\\
=&M^0(t) + \frac{1}{2}q^2M^2(t) + o(q^2),
\end{aligned} \tag{4.66}$$

where D is the dimensionality of the system, here set to $D = 3$.
Finally, putting together equations (4.66) and (4.57), setting the right value for the dimensionality, and simplifying a bit, we get

$$\ddot{\delta r^2}(t) + \frac{k_BT}{m}\int_0^t d\tau\, M^0(t-\tau)\dot{\delta r^2}(\tau) = 6\frac{k_BT}{m},$$

$$\ddot{\delta r^4}(t) + \frac{k_BT}{m}\int_0^t d\tau\, M^0(t-\tau)\dot{\delta r^4}(\tau) = 20\frac{k_BT}{m}\delta r^2(t) + 10\frac{k_BT}{m}\int_0^t d\tau\, M^2(t-\tau)\dot{\delta r^2}(\tau).$$

Both equations might be integrated once,

$$\dot{\delta r^2}(t) + \frac{k_BT}{m}\int_0^t d\tau\, M^0(t-\tau)\delta r^2(\tau) = 6\frac{k_BT}{m}t,$$

$$\begin{aligned}
\dot{\delta r^4}(t) + \frac{k_BT}{m}\int_0^t d\tau\, M^0(t-\tau)\delta r^4(\tau) =& 20\frac{k_BT}{m}\int_0^t d\tau\,\delta r^2(\tau)\\
&+10\frac{k_BT}{m}\int_0^t d\tau\, M^2(t-\tau)\delta r^2(\tau).
\end{aligned}$$

Moving to Brownian dynamics by taking the overdamped limit, as previously, we arrive at

$$\dot{\delta r^2}(t) + D_0\int_0^t d\tau\, M^0(t-\tau)\dot{\delta r^2}(\tau) = 6D_0, \tag{4.67}$$

$$\dot{\delta r^4}(t) + D_0\int_0^t d\tau\, M^0(t-\tau)\dot{\delta r^4}(\tau) = 20D_0\delta r^2(t) + 10D_0\int_0^t d\tau\, M^2(t-\tau)\dot{\delta r^2}(\tau), \tag{4.68}$$

and

$$\delta r^2(t) + D_0 \int_0^t d\tau\, M^0(t-\tau)\delta r^2(\tau) = 6D_0 t, \tag{4.69}$$

$$\delta r^4(t) + D_0 \int_0^t d\tau\, M^0(t-\tau)\delta r^4(\tau) = 20D_0 \int_0^t d\tau\, \delta r^2(\tau) + 10D_0 \int_0^t d\tau\, M^2(t-\tau)\delta r^2(\tau). \tag{4.70}$$

Chapter 5

Phase diagrams and dynamical scenarios

Understanding the dynamics of the system heretofore described is at the core of this work. The structural functions are calculated in the aim of being able to process the Mode Coupling Theory, which can give us insights about the phenomena responsible for the dynamical slow down. This chapter is dedicated to the results of this very crucial part. The approach taken here is to go in more and more depth as for the precision and complexity of the tools used to explore the dynamics. The first section will review the phase diagrams, and explore the many scenarios one can imagine when simply looking at the broad picture they offer. The phase diagrams only offer a view of what the system is at infinite time, and a lot of information is therefore missed, but a general look is very useful. Then, the intermediate scattering function and the mean squared displacement will be analyzed, in order to understand the relaxation process the fluid is going through before reaching its final state. And finally, the local exponent and the non-Gaussian parameter will be discussed, in the hope to get a bit more insight about the complex phenomena in play during relaxation.

5.1 Phase diagrams

A phase diagram is a summary of the different phases the system can be in, delimited by transition lines. Crossing a transition line by increasing one or the other parameter leads the system to a new state, in essence different from the first one. A phase transition thus characterizes an essential change in the nature of the fluid. The usual phase transition that is encountered in a bulk system is characterized by a sudden and discontinuous change in the long time limit of the Intermediate Scattering Function (ISF), and is due to the system reaching a critical density at which the particles are in dynamical arrest, due to the steric hindering of the other particles. However, the presence of a disordered

potential as described in chapter 2 leads to a change of the structure of the equations of the Mode Coupling Theory (MCT), and more precisely of the memory functions: new phases and transition types are therefore to be encountered in the following.

5.1.1 Defining the phases and transition lines

The whole problematic in defining a phase transition is how to distinguish the different phases. From the point of vue of the structural functions, no distinction can be made: both in the case of the liquid, the localized phase and the glass, no long range order can be detected, which is an essential hallmark of fluids.
The difference between these phases lies in the dynamical correlations the fluid is able to keep at long, or virtually infinite times, which is measured by the long time behavior of the self and collective ISF that have been defined in chapter 4. Their behavior is obtained by solving iteratively the structural integral equations, followed by a numerical resolution of the MCT equations. The development of the equations, and a discussion about the theory has been made in chapter 2 for the structural functions and the approximations used to calculate them, and in chapter 4 for the dynamical variables and the discussion around the MCT framework. Calculating the infinite time value of the ISF can be done in a straightforward way by manipulating the equations of MCT, and directly calculating $\lim_{t\to\infty} \phi(q,t) = f(q)$ Götze (1991, 2009); Franosch (2014).

The liquid phase is characterized by an ergodic behavior of the fluid at long times. From the perspective of the MCT, this means that a density fluctuation at infinite time has lost all correlations with its initial value. Thus, the collective ISF eventually reaches zero in the liquid phase:

$$\lim_{t\to\infty} \phi(q,t) = f(q) = 0. \tag{5.1}$$

Another variable commonly used to characterize the phase of a system is the MSD. In a diffusive or liquid phase, the MSD increases linearly with time. In other words, if its slope is equal to one at very long times, the system is in a diffusive phase. A slope that presents a higher value defines a system in a superdiffusive state, which is characteristic for example of the ballistic regime appearing at very small times. A slope lower than one means a system in a subdiffusive state, which is characteristic of a system with a high density, a quenched-annealed system, or in general systems that present any kind of hindering.

On the other hand, if the collective ISF does not reach zero at infinite time, the system is assumed to be in a glass phase:

$$\lim_{t\to\infty} \phi(q,t) = f(q) \neq 0. \tag{5.2}$$

This can be understood as the density fluctuation keeping correlations with its initial time *ad infinitum*. In that case, the system stopped being ergodic at one point of the relaxation process and is in a state of dynamical arrest, which is the definition of a glass. In that phase, the MSD reaches a plateau at infinite times: the subdiffusion is such that the slope is equal to zero.

The liquid and the glass phase are the two common phases a fluid can adopt, but mainly due to the presence of a new vertex in the equations of MCT, an intermediate phase can be found for fluids in disorder: the localized phase. Finding the limit between liquid, glass and the localized phase requires to look at the self ISF as well as the collective one. The localized phase is defined by the fact that the self dynamics have reached an arrested state while the collective dynamics are still in an ergodic (i.e., liquid) state, meaning that

$$\begin{aligned} \lim_{t\to\infty} \phi(q,t) &= f(q) = 0, \\ \lim_{t\to\infty} \phi^s(q,t) &= f^s(q) \neq 0, \end{aligned} \tag{5.3}$$

which naturally defines the localized phase as an intermediate state between liquid and glass. As has been quickly stated in the introduction, the localized phase can be thought of as many pockets of fluid trapped and isolated by deep minima created by the potential. The particles constituting these isolated populations are trapped, a fact made clear by the nonzero value of $f^s(q)$. However the collective dynamics are still globally ergodic meaning that the accessible space is explored constantly and that even though the fluid is localized, no real dynamical arrest has yet occurred.

The phase diagram lies in the three dimensional space defined by (ρ, δ, σ), but in order to show a comprehensible diagram, one parameter has to be kept constant. In the experimental work (Evers *et al.*, 2013a,b; Bewerunge *et al.*, 2016b; Bewerunge and Egelhaaf, 2016; Bewerunge *et al.*, 2016a), the most difficult parameter to stabilize and measure is the correlation length of the potential σ, due to the technical difficulty of generating a controlled laser speckle. The correlation length of the potential is thus consistently chosen as a parameter for the theoretical phase diagrams, ρ and δ being considered as variables. In order to stay consistent with the experimental reference work, in which the correlation length is measured as about half the diameter of a particle, we first choose to set $\sigma = 0.50$, i.e., half the diameter of a particle. However, a study of the effect of a variation of the correlation length has been undertaken, with very interesting results, and is presented in section 5.2.

The choice of the closure relation is of course another variable that has to be taken into account, the dynamics being dependent on the structural functions in the MCT framework, as can be clearly seen from the construction of the memory function in particular.

An extensive comparison of the closure relations will be made and critically discussed as well. For now, the choice has been made to consider HNC as the most realistic closure relation, for the reasons exposed in chapter 3 and reasons that will become obvious later on. Thus, keeping the value of σ constant, and choosing an adequate closure relation, the phase diagram consists of transition lines in the two-dimensional space of the couple of variables (ρ, δ) that delimit the liquid $(f(q) = 0, f^s(q) = 0)$, the localized phase $(f(q) = 0, f^s(q) \neq 0)$ and the glass $(f(q) \neq 0, f^s(q) \neq 0)$.

5.1.2 What phase diagrams can tell us about the dynamics

Figure 5.1 is a phase diagram calculated for a value of $\sigma = 0.5$, and structural functions calculated using the HNC closure relation. Because all the scenarios that we will discuss take place in the variable space spanned in figure 5.1, it will be taken as a basis for the discussions concerning the dynamical scenarios discussed hereafter.

A few things are immediately noticeable from the phase diagram.
If we look at the simple behavior of the system when no potential is involved (i.e., $\delta = 0$) and the density increases (which is equivalent to tracing a horizontal line at the bottom of the phase diagram, and is represented by a dashed gray arrow on figure 5.1), we notice that the system stays in a liquid phase until it reaches a density of about $\rho = 1.0$ and undergoes a discontinuous phase transition to the glass phase. This obviously describes the behavior of the bulk system, and the discontinuous liquid-glass transition occurs at the critical packing fraction. The phenomenon responsible for the phase transition here is called the cage effect: at high density, particles find themselves trapped inside cages created by the body of other particles. At the critical value of the density, the particles are trapped so tightly, any Brownian motion is prohibited, leading to what is called a glass phase. The discontinuous transition line, even though still being present in the case of a system with a disordered potential is mainly still caused by the cage effect. Interplay between the potential and the local density of the fluid causes the increase of the amplitude to have a small but noticeable effect on this transition line, as it will be explicited later on. The fact that, compared to the continuous and the diffusion-localization transitions lines, the discontinuous one is very vertical indicates the rather small influence of the potential on the effects causing it. This further justifies the attribution of the cage effect as a main cause to this transition line.

At zero density, meaning that only one particle is placed in the disordered potential, an increase of the amplitude (which is represented by a dashed gray line on figure 5.1) leads to crossing the continuous and the diffusion-localization transition lines together at the same value of $\delta_c = 1.143$. This fact can be understood by noticing that when the fluid consists of only one particle, the self and collective dynamics are obviously overlapping: $\phi(q, t) = \phi^s(q, t)$. Thus, a change in the self dynamics automatically means a change in

the collective dynamics as well. From a more intuitive point of vue, if the fluid is made out of only one particle, a localization of this particle means a nonergodic system, which in this case means a glass phase.

A second thing that we may notice is the nonmonotonic behavior of the continuous and the diffusion-localization transition lines. Indeed, if the system is set at a constant value of the amplitude, for example $\delta = 1$, and the density is steadily increased, the first thing to happen is that the diffusion-localization line pulls away. This means that the system is less likely to be localized as the density increases. Then, at higher values of the density, the diffusion-localization line experiences a reentrance until its junction with the discontinuous transition line. Therefore, it seems that as the density increases, the system first experiences an acceleration of its dynamics (recession of the diffusion-localization line), and at high values of the density, a slowing down (reentrance of the line). In a bulk hard-sphere fluid, when the density is increased, the dynamics are slowing down more and more, due to the cage effect and steric interactions, until an eventual dynamical arrest occurs at a critical density. Why is this not the case when a disordered potential is present?

In order to understand this rather strange phenomenon, one has to look at the potential in an other way. Figure 5.2 shows a Gaussian random potential with a Gaussian correlation function, generated for the Monte-Carlo simulations. For obvious reasons, the picture has to be presented as a two dimensional potential, but one has to keep in mind that this work concerns three dimensional particles and a three dimensional disordered potential. It seems that the external random field actually takes the form of spots of positive and negative potential, which effectively represent the random light spots created by a speckle pattern. The particles are attracted by the spots of negative potential (in blue) and repulsed by the spots of positive potential (in red).
If only one particle is present in the system (i.e., the case of $\rho = 0$ explored previously), a given value of the amplitude may localize the particle, and lead though the continuous transition line to the glass phase. However, as the density increases, particles start to have interactions with one another. At low values of the density, the hard-sphere interactions allow particles to exchange kinetic energy. This happens by collision, and may contribute to dislodge a particle trapped in a minimum of the potential, thus effectively accelerating the dynamics. Then, as the density increases towards higher values, another phenomenon may take place: the steric hindering starts to have a big importance on the dynamics of the system as a whole. The presence of the potential might lead to several particles being trapped inside a minimum with other particles, leading them to be closer in average, and therefore experience more collisions. But this time, the system is overcrowded in general, and more collisions do not simply mean more kinetic energy, but rather a higher influence of the cage effect, which explains also that as the amplitude increases, the discontinuous transition line recesses in density.

The phase diagram is built as lines separating different long time (typically infinite) behaviors. The domains that these lines separate (liquid, localized and glass) can be linked to isodiffusivity lines, in which the fluid will have a given value of the diffusion coefficient. An isodiffusivity diagram is the closest an experimental picture can get to a theoretical phase diagram. Luckily, this has been done by Jörg Bewerunge as part of his PhD thesis (Bewerunge, 2016), and is shown in figure 5.3. The system studied in the experimental work has been presented in chapter 1. It is very similar to the one studied in this work, with the notable difference however that the experimental work is in two dimensions. This can lead the comparison to be tricky, as any discrepancy can be attributed either to the dimensionality, to the experimental uncertainties, or to possible artifacts of the theory. However, any similarity between the results can be seen as a good validation of both the theory and the experiment.
Comparing figure 5.3 with the phase diagram presented in figure 5.1 (the correlation length of the speckle light spots has been consistently measured to be close to 0.5), we can see one major similarity: the isodiffusivity lines, as well as the transition lines both increase with the density. This corroborates the point stated earlier: an increase of the density leads to an exchange of kinetic energy between particles, allowing trapped populations to escape energy minima, and therefore accelerates the dynamics. The reentrance of the isodiffusivity line is however not observed, but the densities scanned may not allow for this observation to happen. There is an other quantity that can give us insights about the reentrance: the long time diffusion coefficient itself. This quantity is inversely proportional to the distance to the diffusion-localization line in the context of the theory, and to the isodiffusivity lines in the experimental context. Therefore, a reentrance of the diffusion-localization line will be accompanied by a reentrance of the long time diffusion coefficient.

This quantity can be calculated, through the MSD as

$$D_L = \lim_{t\to\infty} \frac{\delta r^2(t)}{6t}, \tag{5.4}$$

where D_L is the long time diffusion coefficient and $\delta r^2(t)$ is the MSD. For the sake of comparison with the experiments, D_L has been calculated by taking constant values of the amplitude, and varying the density regularly until reaching the phase transition. Both the calculated and experimental long time diffusion coefficients are presented in figure 5.4.
The comparison here is quite straightforward, as the figures are very similar: as the amplitude of the potential increases, the long time diffusion coefficient globally decreases. A same reentrant behavior is observed as well on all the curves, which hints at the probable presence of a reentrant behavior concerning the isodiffusivity lines as well, that potential future experiments done at high values of the density will probably observe.

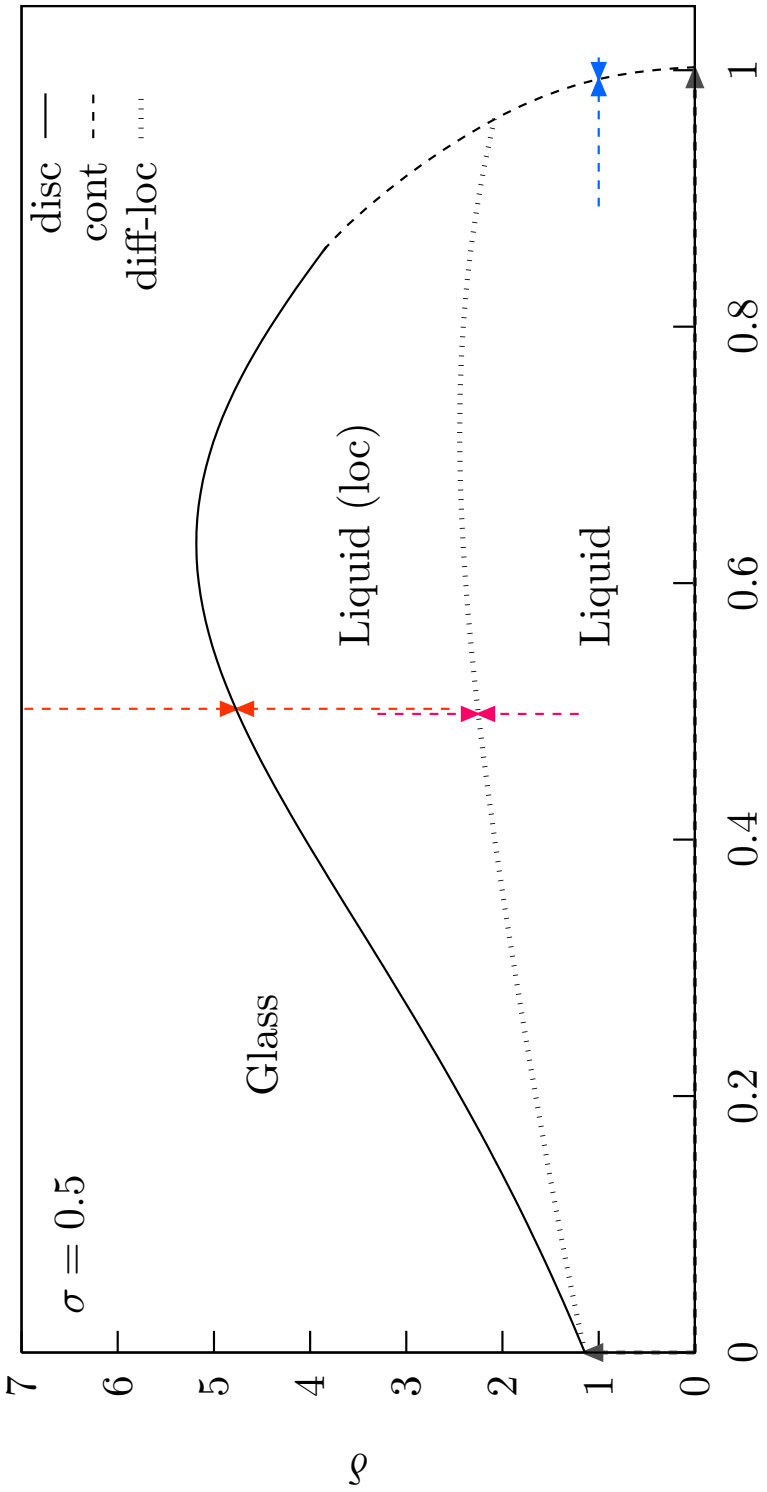

Figure 5.1: Phase diagram of a fluid of hard spheres of density ρ, in a Gaussian random potential with Gaussian correlation function. The relative amplitude of the potential is noted δ and its correlation length chosen as $\sigma = 0.5$. The structure has been calculated using the OZ equation together with the HNC closure relation. The arrows are guidelines for following results.

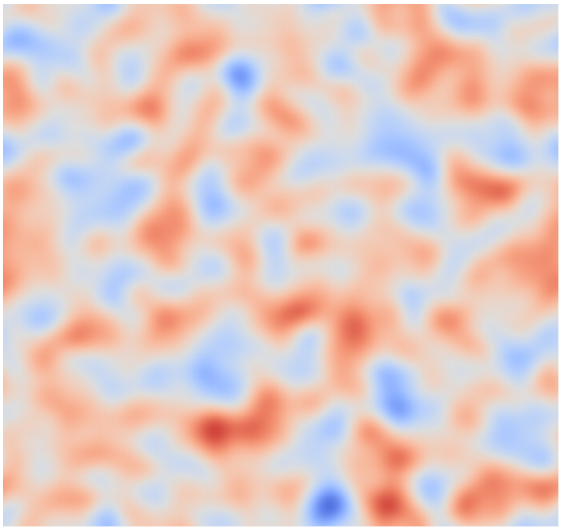

Figure 5.2: 10×10 (unit is the size of a particle) box containing a two dimensional Gaussian random potential with Gaussian correlation function. An arbitrary amplitude has been chosen, and a correlation length of $\sigma = 0.5$. The blue spots represent negative areas and the red spots represent positive areas. Periodic boundary conditions have been applied.

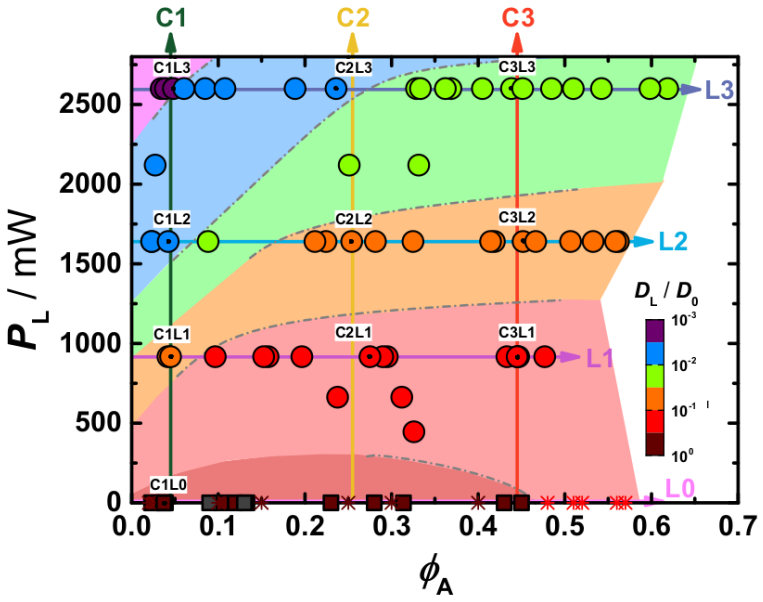

Figure 5.3: Long-term diffusion coefficient D_L of a Brownian fluid of packing fraction Φ_A in a two-dimensional random Potential Energy Landscape (rPEL) of power P_L (equivalent to the amplitude of the potential δ). Filled circles and squares are measured conditions in the presence and absence of a rPEL, respectively. The values of D_L are represented by a color scale, where the gradient from purple to dark red indicates increasing values. Grey dash-dotted lines indicate possible iso-diffusivity lines between suggested colored iso-diffusivity areas. Reproduced from Bewerunge (2016).

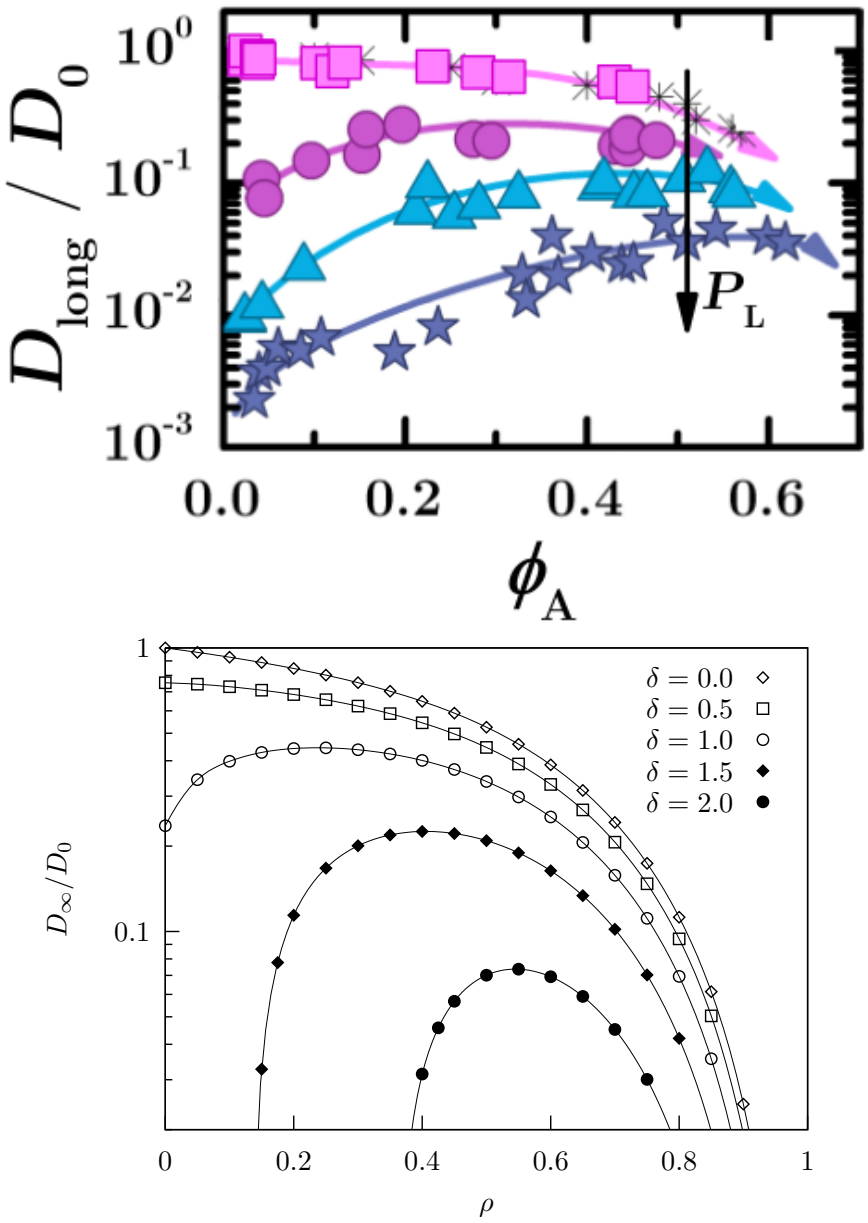

Figure 5.4: **(left panel)** Normalized long-time diffusion coefficient $D_{\rm long}/D_0$ shown for increasing strength of a two-dimensional speckle potential, indicated by magenta squares, purple circles, light blue triangles and dark blue stars, respectively. Experimental data corresponding to the case of no potential and taken from (Ma *et al.*, 2013) is included as black crosses. Lines are guides to the eye. **(right panel)** Normalized long-time diffusion coefficient of a three-dimensional hard-sphere fluid of density ρ, in a Gaussian random field with Gaussian covariance of amplitude δ, and given correlation length $\sigma = 0.5$. The lines are guides for the eye.

5.2 Influence of the correlation length

For a matter of consistency with the experiments, most of the calculations and qualitative studies have been made in a system with a potential that presented a correlation length of half the size of the particle, this being roughly the value that has been calculated in the experiments. However, increasing or decreasing the value of σ may be interesting from a theoretical point of vue. It might also give a guideline to experimentalists on how to trust the determined value of the correlation length. In order to see the effect of the variation of the correlation length on the overall dynamics, a full phase diagram has to be drawn. But testing a continuum of values for σ is near impossible, and anyway probably useless. Thus, a constant step of $\Delta\sigma = 0.25$ has been taken, and a phase diagram calculated for each value of the correlation length. The result concerning the HNC closure relation is presented in figure 5.5.
By many aspects the phase diagrams are similar, but one thing they do not share is their height, i.e., the critical set of variables (ρ_c, δ_c) at which the continuous or discontinuous glass transitions occur. Except for the extremes of the phase diagrams, all the critical amplitudes are increasing dramatically with the increase of the correlation length.
This can be easily explained in the following way: a bigger correlation length means bigger positive and negative spots. Thus, with an increase of σ, more particles fit inside the attractive spots, which means more collisions between them, and subsequently a higher amplitude is required to trap the particles in the potential, and reach a complete dynamical arrest.

Some differences can be noticed between the shapes of the phase diagrams at different values of the correlation length as well. First, the variation of the junction between the continuous and the discontinuous transition lines: between $\sigma = 0.25$ and $\sigma = 0.50$, this junction seems to occur at higher density as the correlation length increases, but between $\sigma = 0.50$ and $\sigma = 1.00$, the junction recesses in density as the correlation length increases. In other words, as we increase the correlation length, the cage effect and steric phenomena play a role at lower and lower density in creating a glass transition. This can be seen more easily by plotting the density at the junction between the continuous and the discontinuous transition $\rho_{\perp^{\text{cont-disc}}}$ as a function of the correlation length σ, as shown in figure 5.6.
How can this behavior be explained? As often in the framework of the MCT, giving a precise quantitative explanation for such a phenomenon is difficult, as the equations do not provide information about the specific phenomena occurring at the level of a particle, but rather give information about the behavior of the fluid as a whole. We can only postulate some scenarios and hope to be one day able to verify them using experimental setups or simulations.

As for the behavior of the continuous-discontinuous junction, the following scenario can be imagined: an increase in σ means an increase of the size of the positive and negative

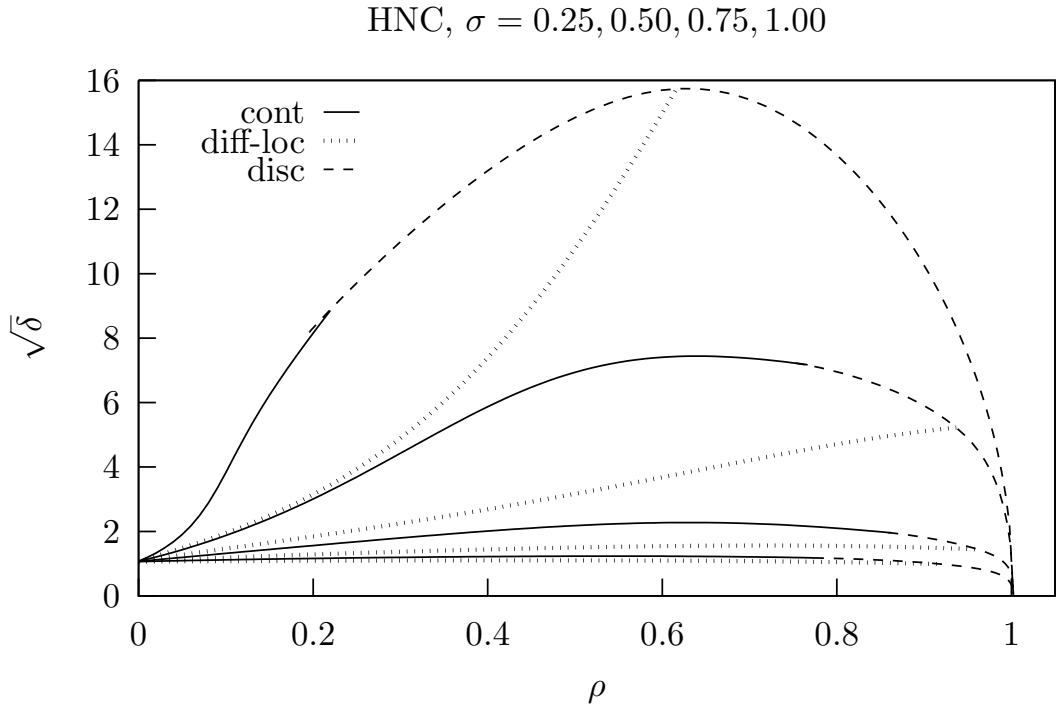

Figure 5.5: Phase diagrams of hard-sphere fluids of density ρ in a Gaussian random potential with Gaussian correlation function of amplitude δ and correlation length σ. Each phase diagram corresponds to a value of the correlation length of the potential σ (from bottom to top one has $\sigma = 0.25, 0.50, 0.75, 1.00$). The structural correlation functions have been calculated using the OZ equation together with the HNC closure relation, and the transition lines have been calculated using MCT.

spots that the potential is essentially made out of. Here, we need to recall that only the center of the particle interacts with the potential, its bulk only preventing it from penetrating other particles.

To make the understanding easy, some schematic dynamical scenarios have been drawn in figure 5.7. By looking at the top left panel of this figure (corresponding to $\sigma = 0.25$), one can see that the size of the spots is quite small compared to that of a particle, which in turn leads to the fact that when a particle sits in a favorable position, the whole attractive spot is covered by the bulk of the particle, leaving no room for another one. Thus, around $\sigma = 0.25$, an increase in δ does not lead to more particles sitting close to each other, but rather that each particle is more and more pinned in one precise position, which is the location of the lowest point of the minimum. In turn, the pinning of the particles leads to a system very close to a quenched-annealed one, where some particles sit in the favorable positions and are immobile, and some particles wander in the matrix of these quenched particles. Thus, the change of the density here needs to

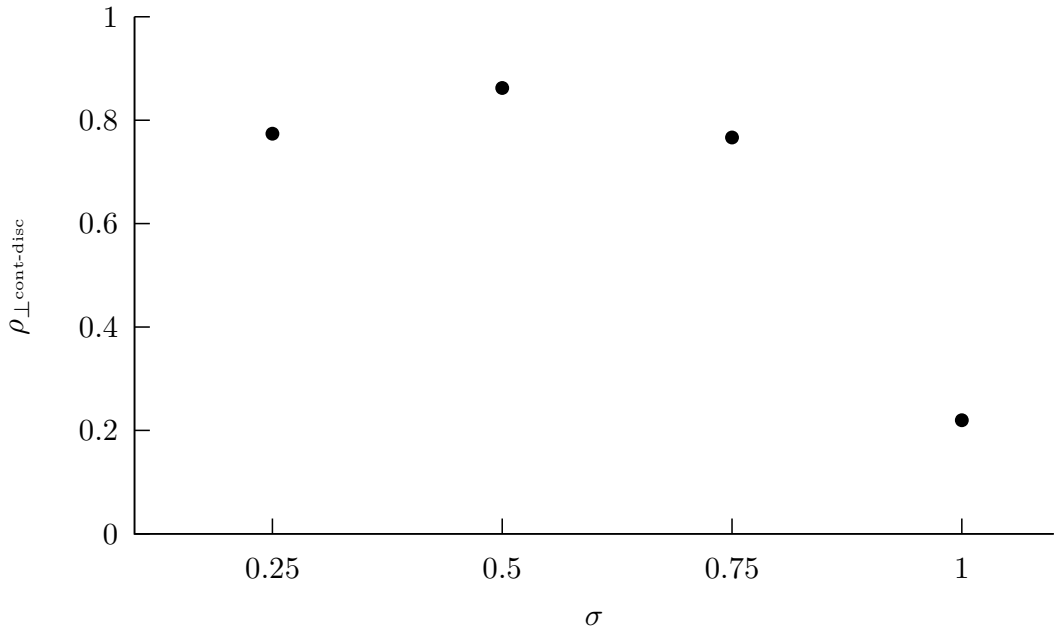

Figure 5.6: Fluid density $\rho_{\perp\,\text{cont-disc}}$ at which the junction between the continuous and the discontinuous glass transition lines happens, as a function of the correlation length σ of the Gaussian random potential with a Gaussian correlation function.

be very important to see any effect, an increase of the amplitude of the potential having the only effect of pinning more and more the already quite quenched particles.
However, starting from $\sigma = 0.50$, up until $\sigma = 1.00$, the junction between these continuous and discontinuous lines occurs at a lower density as σ increases. This can be explained using the same arguments the other way around: starting from $\sigma = 0.50$ more than one particle start to fit inside a minimum. Therefore, as δ increases, these small populations of particles get isolated from the rest of the system, and the size of the populations increases with the correlation length. This probably means that they will experience a lot more collisions between themselves, than with the surrounding particles, a phenomenon that increases with δ. Thus, at high values of the correlation length, increasing the amplitude of the potential will lead to cage-effect-induced glass transitions at low densities, due to this property that the potential has, to group two or more particles inside one minimum.

While this dramatic influence of the correlation length on the shape of the phase diagrams can seem surprising at first, a more intuitive explanation can be given by considering that the correlation length is a defining lengthscale of the system. Hence, we temporarily take it as the unit of length and plot the data of figure 5.5 using $\rho\sigma^3$ as the x-axis. The effects coming from the different values of the correlation length are then accounted for in a more specific picture.

As one can see on figure 5.8, by simply introducing this change, the diffusion-localization transition lines seem to follow a very similar trend, with the only difference of the length of the transition lines. This seems to put the previous problem of the shape of the phase diagrams in function of the correlation length of the potential in a more natural and understandable shrine.

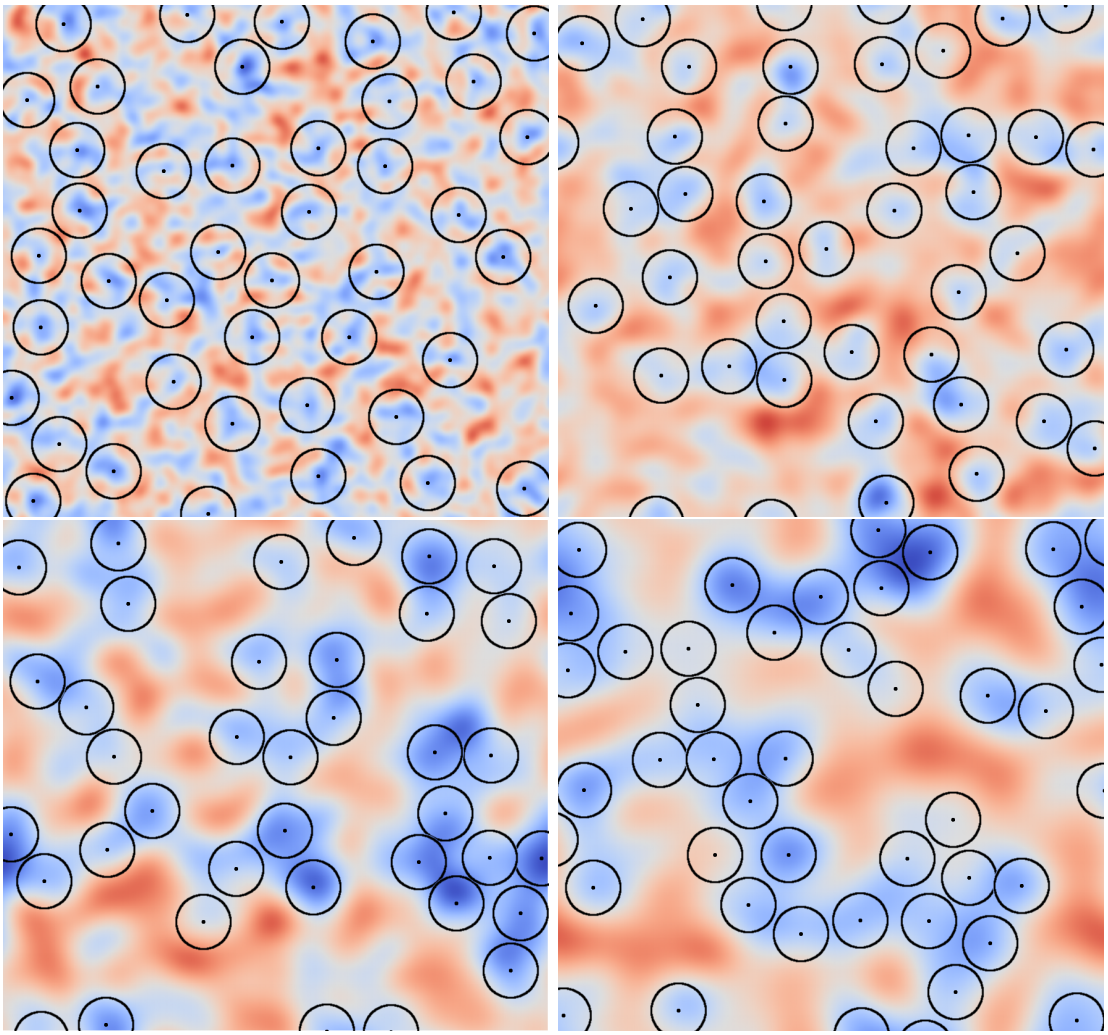

Figure 5.7: Gaussian random potentials with a Gaussian correlation function, generated using the method described in chapter 7. The original potential has been generated in a three dimensional box of $10 \times 10 \times 10$, and the present picture is a cross section of the middle of the box. Particles have been represented in a schematic fashion, not accounting for their respective position on the z-axis. Correlation length is taken as $\sigma = 0.25, 0.50, 0.75, 1.00$ from left to right and top to bottom. Red parts represent high values of the potential, and blue parts low values, the amplitude having been chosen arbitrarily.

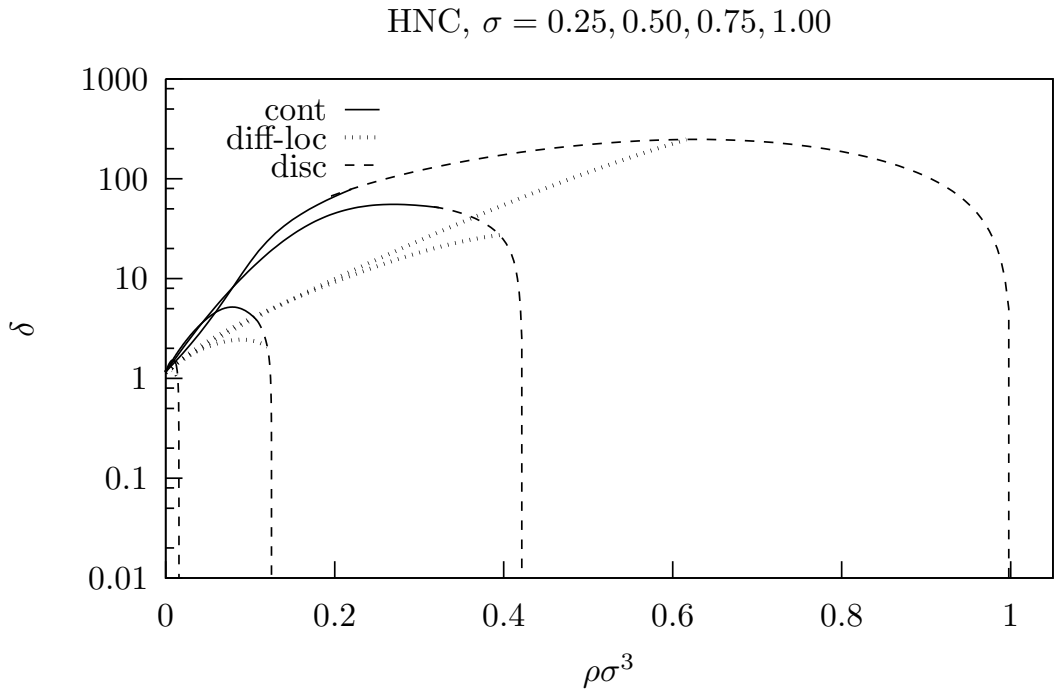

Figure 5.8: Phase diagrams of hard-sphere fluids of density ρ in a random Gaussian potential with Gaussian correlation function of amplitude δ and correlation length σ. Each phase diagram corresponds to a value of the correlation length of the potential σ (from bottom to top one has $\sigma = 0.25, 0.50, 0.75, 1.00$). The x-axis has been chosen as $\rho\sigma^3$, and y-axis is plotted using a logarithmic scale. The structural correlation functions have been calculated using the OZ equation together with the HNC closure relation, and the transition lines have been calculated using MCT.

5.3 Influence of the closure relation

5.3.1 Building upon sand

Due to the structure of the vertices in the MCT framework, the dynamics of the system is fully determined by the structural functions calculated using the Ornstein-Zernike and the closure relations. The latter being the only approximation at that level, it can be considered as a parameter as well. Indeed, closure approximations exist in many flavors, and those that have been tested have been quickly developed and discussed in chapter 3. A quick comparison of these closure relations can be seen in figure 5.9.
First and foremost, only the HNC and MSA closure relations allow for the calculation of a full phase diagram. Concerning PY and EXP, the calculations either could not converge, found new and unphysical solutions to the MCT or outright crashed. The reasons for this have been detailed in chapter 3, and are the result of the closure relations bringing up unphysical solutions, in the form of negative structure factors needed to calculate the dynamics. As a result, as PY fails at low densities, only the discontinuous transition line could be calculated, and EXP failing at high densities allows for a calculation of only the continuous transition.

However, by looking at the shape of the diagrams, it seems that we can separate them into two classes: on one hand, HNC and EXP lead to phase diagrams of low heights, while PY and MSA have overall higher critical parameters. It seems interesting that the closure relations are separated in two classes in this way, and further study of other relations would probably give insights about a fundamental reason for this. Anyway, comparison can be made between the MSA and HNC based phase diagrams, assuming that the PY and EXP respectively would behave in similar ways.

5.3.2 Mean Spherical Approximation

Figure 5.10 shows the phase diagrams of a fluid in a disordered potential, with the structural functions calculated using the MSA closure relation, defined in chapter 2. As reported in chapter 3, the MSA closure relation treats the correlations, both coming from the density and from the potential, in a much lighter way compared to HNC. This leads to the phase diagram being excessively higher concerning the parameter δ.
Another thing one might notice is the fact that the junction between the continuous and the discontinuous transition lines does not lead to the end of the discontinuous transition line, which might extend beyond this point. This is not a perk of the MSA closure relation, and can be observed in the phase diagrams based on HNC as well, although concerning HNC, the overtaking is much smaller, and therefore invisible without zooming. This effect increases with the correlation length of the potential. By crossing the discontinuous transition line while being already in the glass phase, the system un-

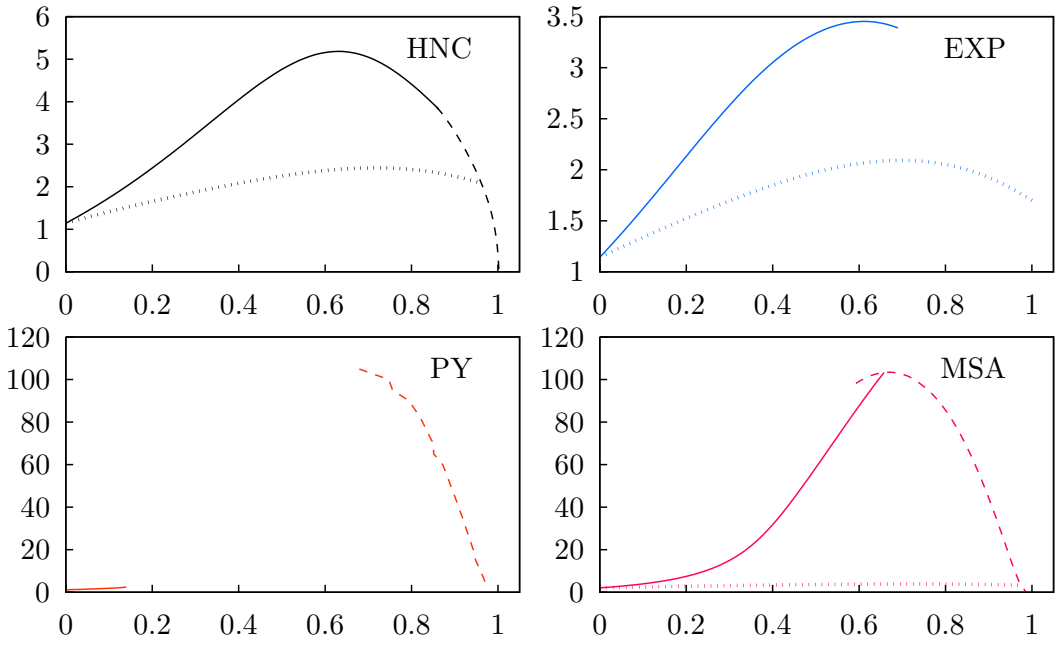

Figure 5.9: Phase diagrams of a fluid in a Gaussian random potential with Gaussian correlation function, calculated using the OZ equation together with the HNC, EXP, PY and MSA closure relations. The x-axis represents the density of the fluid ρ, the y-axis is the amplitude of the potential δ, and the correlation length is taken as a constant for all the phase diagrams as $\sigma = 0.5$.

dergoes a transition between two glass phases. This is shown hereafter in the section dedicated to explicit analysis of the dynamic variables.

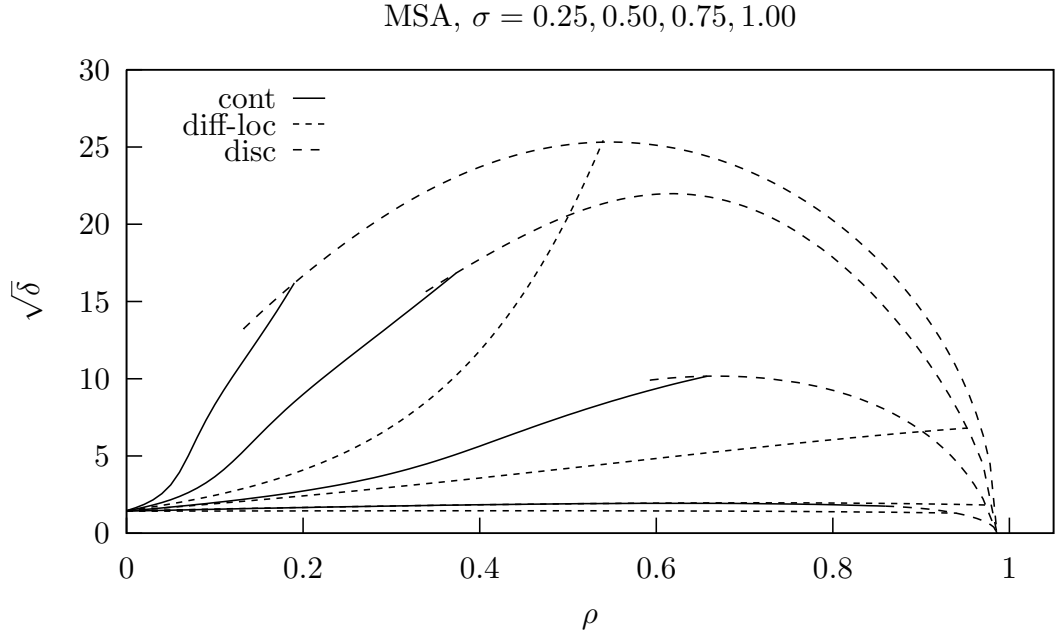

Figure 5.10: Phase diagrams of hard-sphere fluids of density ρ in a Gaussian random potential with Gaussian correlation function of amplitude δ and correlation length σ. Each phase diagram corresponds to a value of the correlation length of the potential σ (from bottom to top one has $\sigma = 0.25, 0.50, 0.75, 1.00$). The structural correlation functions have been calculated using the OZ equation together with the MSA closure relation, and the transition lines have been calculated using MCT.

5.4 Intermediate scattering function and mean squared displacement

While the phase diagram can lead to some interesting results and lead us to imagine general scenarios based on the behavior of the transition lines, a lot of information is missed by not looking at the actual behavior of the ISF, whose infinite time limit only is used to generate a transition line. The collective and self ISF, the MSD and other related parameters as the local exponent and the non-Gaussian parameter can all lead us to scenarios of how the dynamics of the fluid actually behaves *before* total relaxation to either liquid, localized or glass phase. In the following, the phase diagram of figure 5.1 will be taken as a reference for the results exposed. This phase diagram can be considered as a mere map, but the interesting part of the journey is revealed by looking at the road itself.

In the following, dynamical variables will be traced, so to frame a given transition line and highlight the critical phenomena taking place in its vicinity. As the critical phenomena

appear more clearly when looking at the dynamical variable very close to the transition line, and on both sides, one of the variables (ρ or δ) will be taken constant, the other one varied in the following way:

$$\begin{aligned} &\gamma_i = \gamma_c(1+\epsilon), \\ &\gamma = \rho \veebar \delta, \\ &\epsilon = \pm 10^{-n/3}, n \in \mathbb{N}, \end{aligned} \tag{5.5}$$

where γ is either δ or ρ, γ_i is the value at which the given curve is plotted, and γ_c is the critical value of the parameter, at which the phase transition happens. Choosing $\epsilon < 0$ or $\epsilon > 0$ will lead to values respectively below and above the critical amplitude, and a higher value of n allows for arbitrary refinement. The value of this parameter will be typically chosen in the range $n \in [1, 3, 6, 9, 12]$. This scheme has been taken from Franosch *et al.* (1997a). The following results will take this route, and as a guide, one can refer to figure 5.1, where dashed colored arrows have been traced to hint to the exact locations on the phase diagram where the calculations have been performed.

One can refer to chapter 4 for the theoretical developments, and to chapter 6 for the actual implementation of the MCT equations.

5.4.1 Around the diffusion-localization transition line

Let us start in the liquid phase, and explore the variable space around the diffusion-localization line. The density of the system is kept constant at $\rho = 0.5$, and the values of the amplitude have been varied following equation (5.5).
First, one has to look at the curves traced for $\epsilon < 0$, which are located in the liquid phase. In that case, the ISF tends to zero at long times, which is the principal characteristic of the liquid phase. Another characteristic is the behavior of the MSD. At short times, the MSD presents a slope of one, which signifies that the system is totally diffusive. This is the case for all the curves, and is a characteristic of the short time dynamics: the particles are simply exploring their immediate environment, and no interaction with other objects has yet happened. At intermediate times, this slope decreases and the system experiences a subdiffusive regime: the particles interact with their environment, either by collisions with other particles, or with the potential. If the system is in a liquid phase, it eventually goes back to diffusive again at long times. As the amplitude of the potential increases, the ISF takes more and more time to reach zero, and the MSD more and more time to reach its final slope.

The critical amplitude is represented by the red line, above which the behavior of the MSD changes: after a period of subdiffusion, it reaches a plateau at long times, which means that the system does not explore anymore space, which is a characteristic of

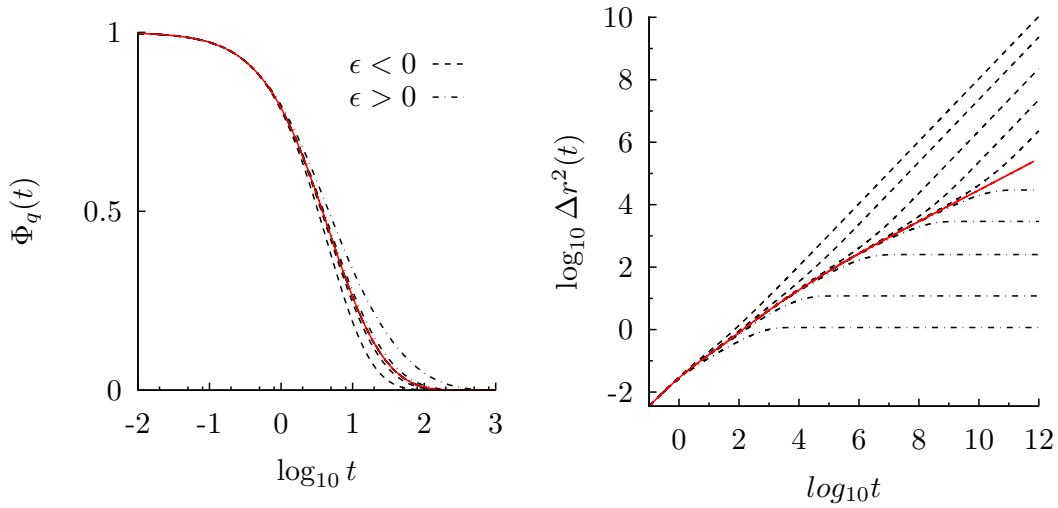

Figure 5.11: **(left)** collective ISF and **(right)** MSD of a fluid of density $\rho = 0.5$, in a Gaussian random potential with Gaussian correlation function of amplitude δ and correlation length $\sigma = 0.5$. The amplitude has been chosen, following equation (5.5), to frame the diffusion-localization transition line (see the pink arrows on figure 5.1). The red curve is taken at the critical amplitude $\delta = \delta_c$ $(n \to \infty)$. The structural correlation functions have been calculated using the OZ equation together with the HNC closure relation.

a localized system. On the other hand, the collective ISF still reaches zero, which is characteristic of a liquid.

This paradoxical state of the fluid is called the localized phase: the fluid as a whole is still ergodic, but the full space is not explored anymore by individual particles. One possible explanation of this state is that the minima of the potential are so deep that the populations of particles trapped inside them are virtually isolated from one another. However, the amplitude is not high enough so to create a dynamical arrest, which would be the case in a glass phase. Therefore, inside these pockets created by the potential the system is still relaxing, but the area explored is limited to the pocket itself.

Further increase of the amplitude of the potential leads to a decrease of the value of the plateau of the MSD. The ISF on the other hand takes more and more time to reach zero. These two facts mean that the dynamics of the liquid become slower as the amplitude increases: the potential localizes and further restrains the space available to the particles.

5.4.2 Around the continuous transition line

Increasing again the amplitude of the potential from the localized phase eventually leads the system to the glassy phase, by crossing the continuous transition line at densities

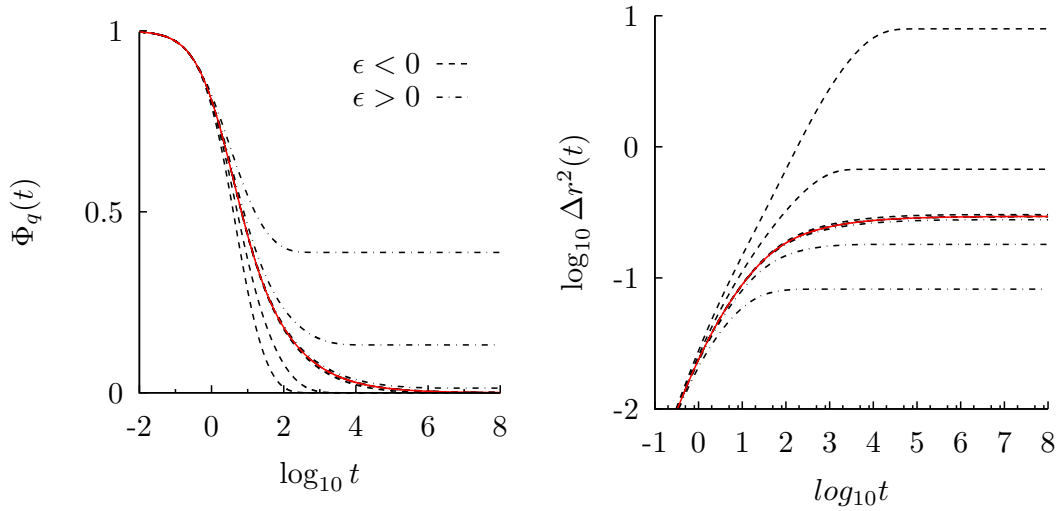

Figure 5.12: **(left)** collective ISF and **(right)** MSD of a fluid of density $\rho = 0.5$, in a Gaussian random potential with Gaussian correlation function of amplitude δ and correlation length $\sigma = 0.5$. The amplitude has been chosen, following equation (5.5), to frame the continuous transition line (see the orange arrows on figure 5.1). The red curve is taken at the critical amplitude $\delta = \delta_c$ ($n \to \infty$). The structural correlation functions have been calculated using the OZ equation together with the HNC closure relation.

lower that $\rho \approx 0.90$. Figure 5.12 shows the collective ISF and the MSD in the process of crossing the continuous transition line from a localized liquid to a glass.
This time, the ISF is the interesting observable, the MSD having reached its plateau does not fundamentally change its behavior, except for a further lowering of the value of this plateau, which means a further localization of the particles. In the localized phase ($\epsilon < 0$) the collective ISF reaches zero, but as we approach the continuous transition line, the time taken to reach that value is longer and longer. On the transition line, represented by the red line, the time taken to reach zero is infinite, and above it the collective ISF does reach a nonzero plateau instead. The ISF therefore continuously transitions from one regime ($\lim_{t\to\infty} \phi(q,t) = 0$) to another ($\lim_{t\to\infty} \phi(q,t) \neq 0$). This last regime is the characteristic of a fluid in dynamical arrest: a glass.

5.4.3 Around the discontinuous transition line

The continuous transition line gives way to the discontinuous transition line around $\rho = 0.90$. This is expected, and has been treated previously with the scenarios coming from the shape of the phase diagrams. The behavior of the ISF and the MSD when crossing the discontinuous transition line is showed in figure 5.13, where the amplitude of the potential has been kept constant at $\delta = 1.0$, and the density varied in the same

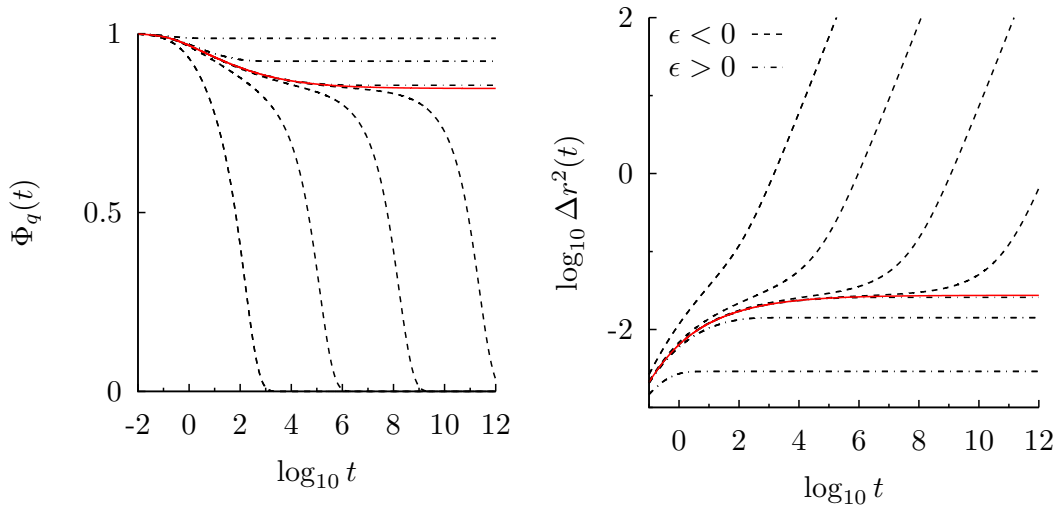

Figure 5.13: Collective ISF **(left)** and **(right)** MSD of a fluid of density ρ, in a Gaussian random potential with Gaussian correlation function of amplitude $\delta = 1.0$ and correlation length $\sigma = 0.5$. The density has been chosen, following equation (5.5), to frame the discontinuous transition line (see the blue arrows on figure 5.1). The red curve is taken at the critical density $\rho = \rho_c$ $(n \to \infty)$. The structural correlation functions have been calculated using the OZ equation together with the HNC closure relation.

way as previously done, around the transition line.
The behavior of the collective ISF here is fundamentally different from the continuous case. In the liquid phase, the ISF still reaches zero at long times, meaning that the relaxation of the system brings it in an ergodic state eventually. However at intermediate times, the ISF develops a plateau, that lasts longer and longer as the critical density is approached. The discontinuous transition line takes its name from the fact that the dynamical variables are undergoing a sudden and discontinuous change in their behavior when crossing that line. Therefore, when the critical density is reached, the plateau developed by the ISF lasts for an infinite amount of time leading to a nonzero value for the long time limit of the ISF. The difference with the case of the continuous transition line of figure 5.12 is that the nonzero value of $f(q)$ is reached in a discontinuous way, as a sudden plateau appearing after a precise value of the density is crossed. A further increase of the density leads to the value of the plateau tending towards one.

The MSD behaves in a related way: in the liquid state eventually the slope of the function reaches one which characterizes a diffusive regime, after passing through a longer and longer subdiffusive regime as the density gets close to ρ_c. After having reached a critical density represented by the red curve, the MSD reaches a plateau at infinite time, meaning that the particles are trapped. If the density is increased further, the plateau of the MSD

decreases, which means that the particles are more and more localized. Conversely, the value of the long time ISF gets closer to one meaning that the system is at an almost complete dynamical arrest.

5.4.4 A glass-glass discontinuous transition line?

One special feature that the MCT predicts is the possibility for the system to undergo a glass-glass transition. This has been introduced earlier with the phase diagram calculated using the MSA closure relation, on which the discontinuous transition line dramatically extends beyond its junction with the continuous transition line. This perk is not specific to the MSA closure relation, but can be observed using basically all the closure relations. MSA however has the property to lead to almost excessively big phase diagrams, and this phenomenon can be observed more easily in this case. This has not been observed experimentally, the power necessary to generate a speckle that would create a liquid-glass transition having not yet been achieved. However, theory leaves us free to postulate the consequences of this phenomenon, which will hopefully be observed in future experiments.

A discontinuous transition line extending in the glass phase means that by crossing that line, the fluid can go from one type of glass to another. This has been represented in figure 5.14, where the density is kept constant at $\rho = 0.6$, and the amplitude of the potential varied so to frame closely that transition line, using (5.5) as previously.
It so happens that some of the curves have been set in the localized phase, below the continuous transition line, which is therefore traced in dashed red line. In this case, what has been said for figure 5.12 still holds: the ISFs calculated below the continuous transition line reach zero at long times, but as the amplitude is increased this time increases as well, and the continuous transition line is met when the time taken to reach zero is infinite. When the amplitude is increased further, the values of the ISF at long time increase, and seem to converge towards a limit. This limit is overcame when the discontinuous transition line is crossed, at which the long time value of the ISF jumps discontinuously from one limit to a higher value. Further increase of the amplitude leads this value to increase as well, seemingly without limit. This also happens concerning the MSD: even though the system is in a glassy phase a limit seems to be reached. This limit is overcame with an increase of the amplitude of the potential, causing a discontinuous jump for the long time values of the MSD as well.

This indicates that there are two types of glasses present in this system: the one that is located between the continuous and the discontinuous transition line, and the one that is located above the latter. By nature, these two types of glasses do not seem to differ: they both lead the ISF and the MSD to a nonzero plateau at long times, except the value of the plateau is different. The system could go from one type of glass to another by

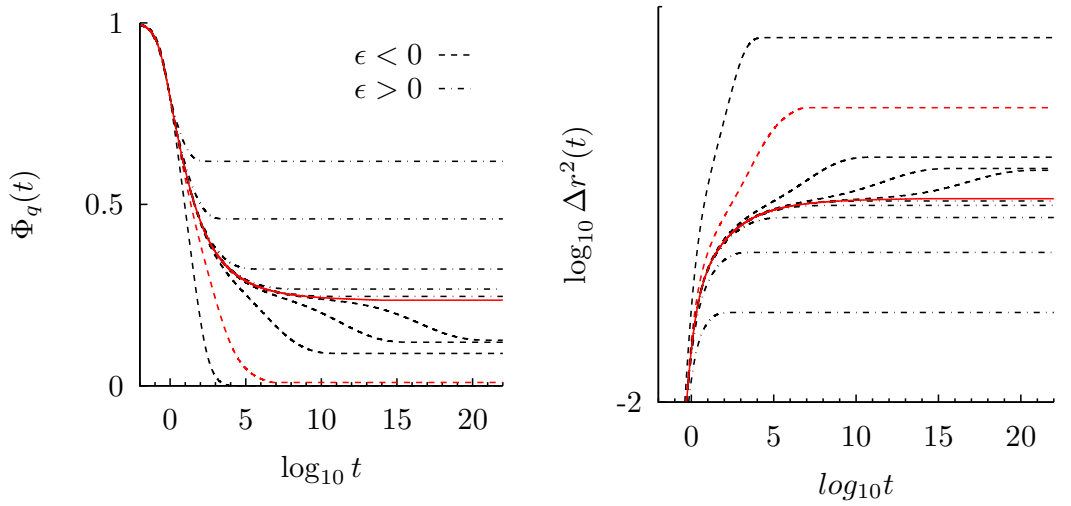

Figure 5.14: **(left)** collective ISF and **(right)** MSD of a fluid of density $\rho = 0.6$, in a Gaussian random potential with Gaussian correlation function of amplitude δ and correlation length $\sigma = 0.5$. The amplitude has been chosen, following equation (5.5), to frame the discontinuous transition line (see figure 5.10). The red curve is taken at the critical amplitude $\delta = \delta_c$ $(n \to \infty)$. The structural correlation functions have been calculated using the OZ equation together with the MSA closure relation.

simply circumventing the discontinuous transition line. In that case, we would observe that the plateaus of the ISF and the MSD undergo a continuous variation to the new value. The ISF and the MSD do not seem to offer much insights about the nature of these two glasses, and they indeed seem of a similar nature, but more complex dynamical observables could highlight some differences between them. The local exponent and the non-Gaussian parameter will be traced as well, after some discussion, in the following.

5.5 Local exponent and non-Gaussian parameter

A normal diffusion is characterized by two features: the MSD increases linearly with time, and the mean distance from the origin of the particles after a given time follows a Gaussian distribution, whose width is given by the MSD. Therefore, the probability of finding a given particle at a distance r away from its origin at time t follows the rule

$$P(r,t) \propto e^{-\vec{r}^2/2\delta r^2(t)}. \tag{5.6}$$

Starting from this fact, there are several ways one can analyze an anomalous diffusion by looking at its time and space variations. This leads to the definition of more refined tools compared to the ISF and the MSD. However, more refined tools means more difficult analysis, the following will therefore consist of surface analysis, with a few conjectures.

The first one of these tools is the local exponent: by defining the MSD as a function of time, its slope can be considered as an indicator of the way the diffusion of the system varies in time. The MSD can be written as

$$\delta r^2(t) = t^{\mu(t)}, \tag{5.7}$$

where $\mu(t)$ is called the local exponent, and in the case of a normal diffusion is equal to one. The local exponent can be extracted by taking the logarithmic derivative of the MSD as

$$\mu(t) = \frac{d \log \delta r^2(t)}{d \log t}. \tag{5.8}$$

This function informs about the specific way the diffusion is changing in time, and might give insights about behavior that are missed by simply looking at the large picture the MSD gives us. In case of subdiffusion, the local exponent presents a value lower than one, and in case of superdiffusion (which will not be encountered here), it presents a value higher than one.

The second parameter we may look at is the Non-Gaussian Parameter (NGP). Recalling that a normal diffusion leads the distance of the constituent particles from their origin to follow a Gaussian distribution, any deviation from this may be an interesting characteristic of anomalous diffusion. The development of the MCT specialized to the NGP has been done in chapter 4, and requires the calculation of the mean quartic displacement as well as the mean squared displacement. The NGP is then obtained as

$$\alpha(t) = \frac{3}{5} \frac{\delta r^4(t)}{(\delta r^2(t))^2} - 1, \tag{5.9}$$

where $\alpha(t)$ is the NGP, and $\delta r^4(t)$ is the mean quartic displacement.

To sum up, the local exponent gives clues about the way anomalous diffusion unfolds in time, and the NGP informs about how it unfolds in space. However, a slowing down of the dynamics (lower values of $\mu(t)$) does not automatically lead to a lower distance traveled by the particles (lower values of $\alpha(t)$) and vice versa. Therefore, while these two parameters are related to the gaussianity of the diffusion, they may not be correlated, leading to a rather cumbersome interpretation.

5.5.1 Around the diffusion-localization transition line

Figure 5.15 shows the local exponent and the NGP around the diffusion-localization line, at a constant density of $\rho = 0.5$, and amplitude of the potential varied in the same way as in figure 5.11, framing the transition line.
Let us first look at the local exponent, for which the first curve on the top is located far in the liquid phase at an amplitude of $\delta = 1.2$. At short times (of which most has been

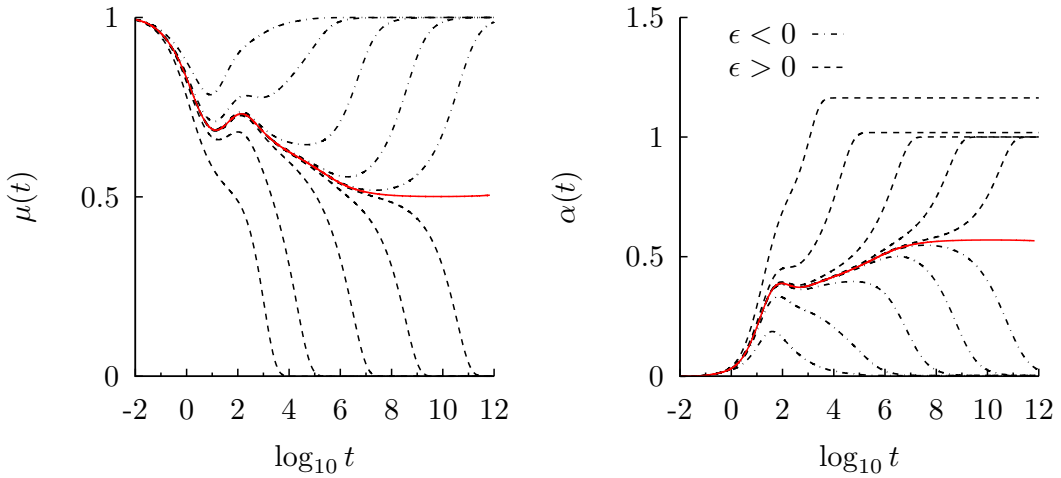

Figure 5.15: **(left)** local exponent and **(right)** NGP of a fluid of density $\rho = 0.5$, in a Gaussian random potential with Gaussian correlation function of amplitude δ and correlation length $\sigma = 0.5$. The amplitude has been chosen, following equation (5.5), to frame the diffusion-localization transition line (see the pink arrows on figure 5.1). The red curve is taken at the critical amplitude $\delta = \delta_c$ $(n \to \infty)$. The structural correlation functions have been calculated using the OZ equation together with the HNC closure relation.

cut) we have $\mu(t) = 1.0$, which is a common characteristic of all the curves, and of short time dynamics in general. At intermediate times, the first curve shows a minimum that appears around $t = 1$ hinting to a subdiffusive behavior, which then resorbs leading to $\mu(t) = 1.0$ at long times: the system is diffusive and therefore in a liquid phase.

However as the amplitude of the potential increases, a new minimum starts to appear around $t = 10^4$. The width of this minimum increases with the increase of the amplitude, which means that the particles are slowing down more and for longer times, until the diffusion-localization line at which the width of the minimum is infinite. The value reached by the local exponent here is known in the framework of MCT to be exactly $\lim_{t\to\infty} \mu(t) = 0.5$.

The emergence of this new minimum does not lead the first one to disappear however. The first minimum being present at low values of the amplitude, we may postulate that the subdiffusive regime it hints at is due to the cage effect and density related phenomena. The second minimum, emerging and deepening with the increase of the amplitude, can be thought to be caused by the external disordered potential. As this last minimum leads into the diffusion-localization line, we can assess for sure that the phase transition is here cause mainly by the potential.

With a further increase of δ, the time taken to reach zero is reduced, meaning that the

time until localization of the fluid is shorter, the potential being deeper and trapping the particles more easily.

Two things are to be learnt from this. First, the density related subdiffusive phenomena and the potential related phenomena are two separate things. The interplay between the two phenomena exists however, as it can be seen from the deepening of the first minimum with the increase of the potential, but the effect seems overall small. Second the density related phenomena occur *before* the potential related ones. This latter fact is furthermore systematic: all local exponent examples show the same behavior.

The NGP, though not being an easy-to-understand variable, might anyway give some insights about the subdiffusion phenomena. Looking at the lowest curve, corresponding to the highest for the local exponent, we can see that it starts at zero, then grows a peak around $t = 10^2$, to finally go back to zero. This means that the diffusion is at short times a Gaussian one, which is expected at short times. Around intermediate times the particles start to travel further as we can see from the higher value of the NGP, before eventually going back to a Gaussian diffusion again. As the amplitude increases, the said peak grows, and another one starts to appear, very much like the second minimum of the local exponent does. The times are however not exactly corresponding, and we cannot assess for sure that a specific non-Gaussianity of the diffusion is related to a specific subdiffusive regime, but the temptation is big. Again, in the same way than for the local exponent, the second peak appearing only when the amplitude increases, the potential can be thought to be its main cause, and the first peak therefore seems to be caused by density related effects. At the diffusion-localization transition, the width of the second peak is infinite, leading to a discontinuous jump of the infinite time NGP to a nonzero value. In the framework of the MCT, the value reached by the NGP at the very critical amplitude δ_c is known to be $\lim_{t\to\infty} \alpha(t)|_{\delta=\delta_c} = \frac{\pi}{2} - 1$. A further increase of δ leads to another discontinuous jump of the infinite value of the NGP towards $\lim_{t\to\infty} \alpha(t)|_{\delta\to\delta_c^+} = 1$.

5.5.2 Around the discontinuous transition line

From the perspective of the local exponent and the NGP, crossing the continuous transition line is rather uninteresting. Both these variables are dependent on the MSD, whose essential changes of regime occur when the fluid exits the liquid phase, either to the localized phase through the diffusion-localization transition line, or to the glass phase through the discontinuous transition line. The continuous transition case will therefore not be shown here, bringing no interesting features nor discussions. The case of the discontinuous transition line is shown in figure 5.16, where the local exponent and the NGP have been plotted at a constant value of $\delta = 1.0$, and density framing the transition line in the way adopted previously.

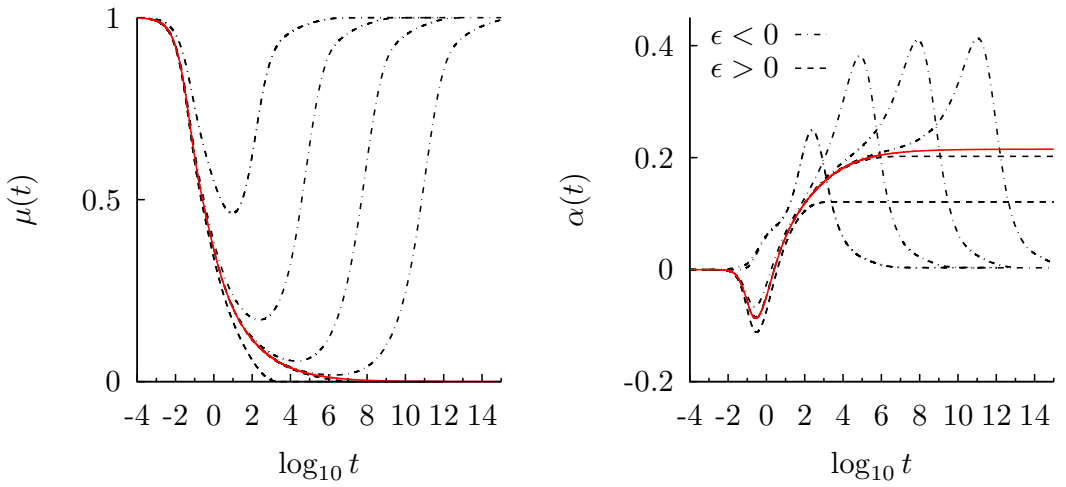

Figure 5.16: **(left)** local exponent and **(right)** NGP of a fluid of density ρ, in a Gaussian random potential with Gaussian correlation function of amplitude $\delta = 1.0$ and correlation length $\sigma = 0.5$. The density has been chosen, following equation (5.5), to frame the discontinuous transition line (see the blue arrows on figure 5.1). The red curve is taken at the critical density $\rho = \rho_c$ $(n \to \infty)$. The structural correlation functions have been calculated using the OZ equation together with the HNC closure relation.

The first curve of the local exponent on the top is located in the liquid phase at a quite high density of $\rho = 0.89$. At short times, as in figure 5.15, this function equals one meaning that the system is diffusive. At intermediate times, a minimum develops around $t = 10^2$ which, as the density increases, broadens, deepens, and shifts to the right. This indicates that the system develops a subdiffusive regime that intensifies and lasts for longer and longer time with an increase of the density. When the discontinuous transition line is met, the minimum reaches zero and its width is infinite. The system has therefore reached a nondiffusive state at long times: the system is in a state of dynamical arrest, the glass phase. Subsequent increase of the density leads the local exponent to reach zero earlier.

In comparison with figure 5.15, only one minimum is present in this case, which by looking at the apparition time, can be identified to the density related one. Furthermore, this minimum increases as a result of the increase of the density, and is the one leading to the dynamical arrest through the discontinuous transition line, which corroborates the latter fact.

The case of the NGP here is somewhat trickier to analyze. All the curves of the NGP present a value of zero at short times, meaning that the distribution of the particles around their initial position follows a Gaussian distribution. At a density of $\rho = 0.89$

(the first curve), the NGP starts to increase at $t = 1$ and reaches a peak around $t = 10^3$, times at which the particles travel further compared to a normal distribution. The system being in the liquid phase, this peak is followed by a decrease to zero at long times. As the density increases towards the discontinuous transition line, the peak described previously shifts to the longer times, while a minimum appears at short to intermediate times. At the transition line, the second peak disappears, leaving only a plateau, and with subsequent increase of the density, the value of the plateau shifts down. In this case, we can assume that the said peak has simply shifted towards infinite time. The sudden apparition of a minimum at short times seems to indicate a change of regime of the system, that persists after the phase transition. This minimum cannot be correlated to a change in the local exponent, nor in the ISF or the MSD, so any attempt of interpretation would lead to unclear conclusions. We hope that in the future experimental studies would observe this phenomenon and trace it back to a probable cause, is there is any.

5.5.3 Around the glass-glass transition

The case of the glass-glass transition mentioned earlier left a quit unsatisfying taste, the conclusions from the study of the ISF and the MSD being that even though this strange phenomenon happens, no real distinction can be made between the two types of glasses. However, tracing the local exponent and the NGP at the same set of parameters leads to interesting observations. This is shown in figure 5.17, where the density has been kept at a constant value of $\rho = 0.6$, and the amplitude varied following equation (5.5).
Many phenomena are at play in this case: the continuous transition line is very close and probably influencing the dynamics a lot, and the transition from one glass to another seems to bring a lot of complex phenomena to play, concerning both the local exponent and the NGP. Therefore, no interpretation will be attempted.

At low values of the amplitude, the local exponent has a bump, seemingly inherited from the continuous transition, that shifts to the right as the amplitude increases. On the other hand, the NGP develops a minimum at short times, that converges towards a limit as the amplitude increases. As the discontinuous transition line is approached, a plateau forms at intermediate times, before the value goes up at infinite time to another plateau. At the transition line, the plateau jumps to a lower value, indicating a new regime.

This time, by looking at more complex values like the local exponent and the NGP, it seems clear that the dynamical phenomena leading to the two glasses are different in nature. However, these scenarios are extremely complex, and the times very long. Observing these phenomena in experiments is therefore very improbable.

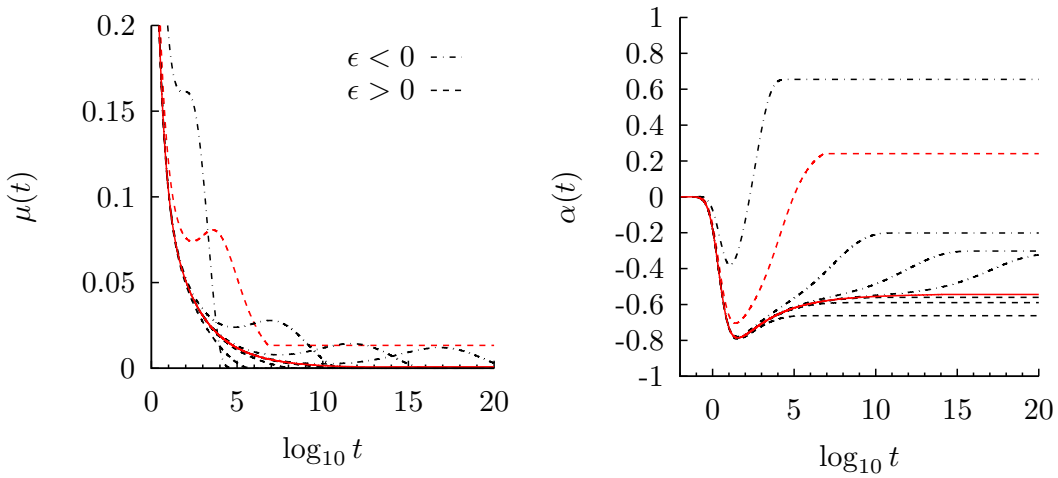

Figure 5.17: **(left)** local exponent and **(right)** NGP of a fluid of density $\rho = 0.6$, in a Gaussian random potential with Gaussian correlation function of amplitude δ and correlation length $\sigma = 0.5$. The amplitude has been chosen, following equation (5.5), to frame the discontinuous transition line (see figure 5.10). The red curve is taken at the critical amplitude $\delta = \delta_c$ ($n \to \infty$). The structural correlation functions have been calculated using the OZ equation together with the MSA closure relation.

5.5.4 Unusual shape of the local exponent

The last phenomenon that we may discuss in this work concerns the shape of the second minimum observed in the local exponent. As it has been dicussed earlier, this minimum finds its origin in the action of the potential on the dynamical slowing down of the dynamics, and it systematically happens at a later time than the minimum caused by the cage effect. The shape of this minimum has been observed to be quite characteristic of this type of phenomenon, however no in-depth discussion has been undertaken. Figure 5.18, top panel, shows the local exponent at zero density for a correlation length of $\sigma = 0.75$, and an increasing amplitude of the potential until δ_c, where the liquid gives way to the glass by crossing both the continuous and diffusion-localization transition lines at the same time. The bottom panel shows a simulation result from Schnyder *et al.* (2015) where a single tracer is set to move in a two-dimensional landscape of quenched particles with a Weeks-Chandler-Andersen (WCA) potential.

First, looking at the top panel of figure 5.18, we can see that as the amplitude of the potential increases, a minimum of the local exponent appears at intermediate to long times, as described previously. This minimum however seems to be the sum of two minima located at different times. The first one appears at $\delta = 0.0^+$ around $t = 10^1$, while the second one appears at higher values of δ around $t = 10^2$ and shifts to later times as δ increases. At high values of δ, and as we approach the transition line, the

second minimum takes over the first one and eventually leads to the transition. The first minimum is then reduced to a simple shoulder on the left side of the second one. The presence of these two minima hints to the existence of two distinct dynamical phenomena that are both linked to the presence of the external disordered potential.

At first, the presence of these two minima has been mistaken for a mere artifact of the MCT, but the simulation study of which a picture is presented on the bottom panel of figure 5.18 hints to physical reality. On this figure the curves are plotted for increasing values of the reduced number density n^*_{WCA}. As this parameter increases, a minimum first appears around $t = 10^1$, and the second one appears at higher values of the reduced number density at later times and shifts in the same way as described for the second minimum seen on the top panel. The WCA potential is a Lennard-Jones like type of potential and provides therefore with a smooth interaction between the quenched particles and the tracer. Similarly, the disordered potential studied throughout this work creates a smooth energy landscape for the hard spheres that constitute the fluid. Therefore, despite many differences (namely the dimensionality, the nature of the potential and the method of study) the two systems have in common the fact that the potential experienced by the particle is smooth. The existence of two minima, linked to the action of two distinct dynamical phenomena, can be thought to be a characteristic of dynamics with smooth interactions. The very nature of the dynamical phenomena is yet to be uncovered, and we hope that future simulation studies could pinpoint the causes of this complex behaviour.

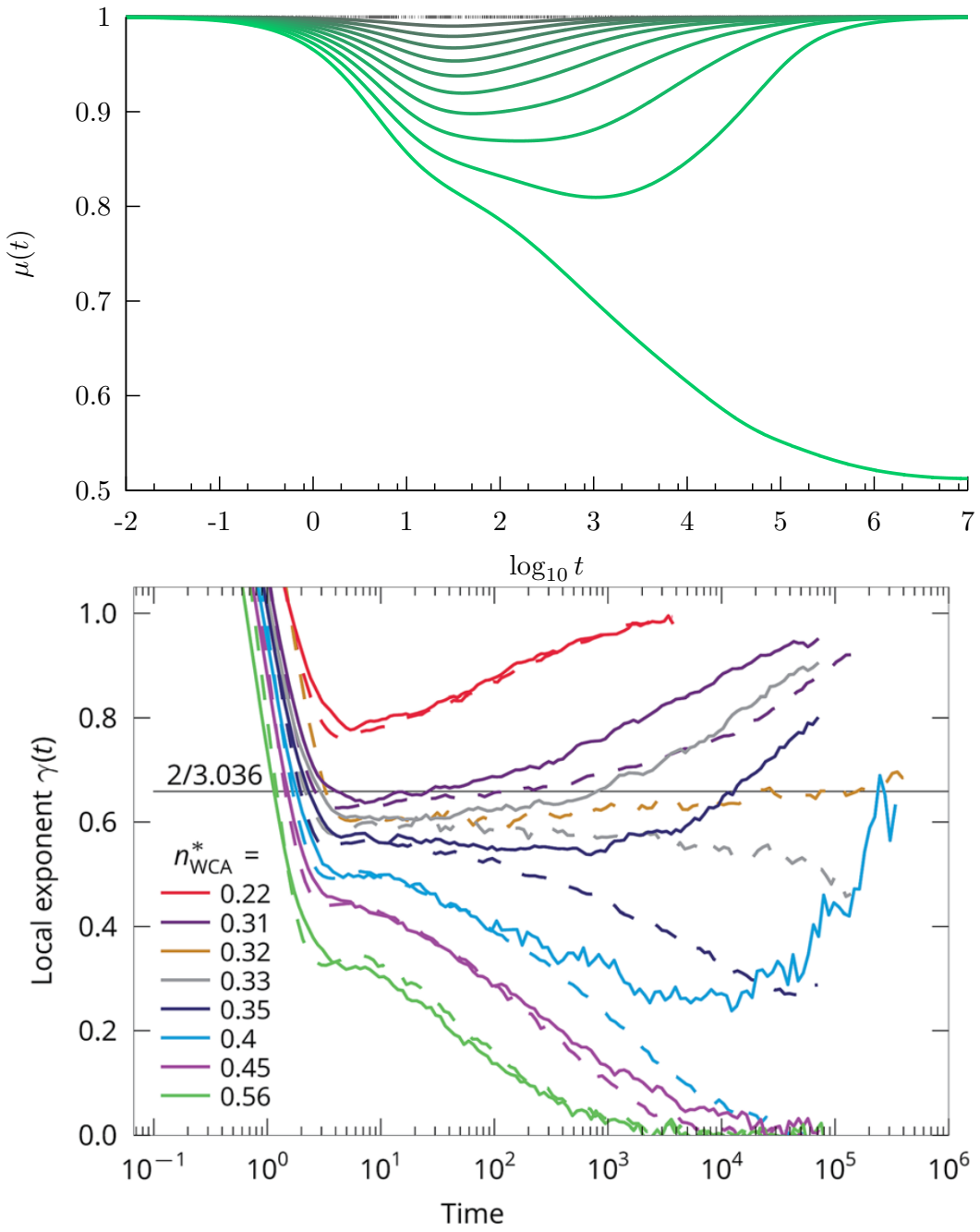

Figure 5.18: **(top)** Local exponent of a fluid at zero density, in a Gaussian random potential with Gaussian correlation function of amplitude δ and correlation length $\sigma = 0.75$. The amplitude has been steadily increased so that ten curves are traced between $\delta = 0.0$ and $\delta = \delta_c$. The value of the amplitude is proportionnal to the saturation of the colors. **(bottom)** Local exponent of a single particle in a quenched matrix of particles with a WCA potential. The parameter n^*_{WCA} defines both the density of the quenched particles and the range of their potential. Reproduced from Schnyder *et al.* (2015).

Chapter 6

Numerical details

6.1 Structural calculations

6.1.1 Description of the algorithm

The calculation of the structural functions is done using the Ornstein-Zernike equations, together with a chosen closure relation. The developments leading to the suited equations have been presented in chapter 2, but the actual implementation and solving of these equations requires methods and precisions that are the point of this very chapter.

We recall the form of the OZ equations:

$$\begin{cases} h(r) = c(r) + \rho \int c(r)h(r) - \rho \int c^d(r)h^d(r), \\ h^d(r) = c^d(r) + \rho \int c(r)h^d(r) + \rho \int c^d(r)h(r) - 2\rho \int c^d(r)h^d(r), \end{cases} \tag{6.1}$$

$$\begin{cases} h(q) = c(q) + \rho c(q)h(q) - \rho c^d(q)h^d(q), \\ h^d(q) = c^d(q) + \rho c(q)h^d(q) + \rho c^d(q)h(q) - 2\rho c^d(q)h^d(q), \end{cases} \tag{6.2}$$

where equations (6.1) are the OZ relations in real space and equations (6.2) are in reciprocal space. By working in the reciprocal space, the terms on the r.h.s of the equations which are convolutions in real space become simple products. This has the advantage of both simplifying the structure of this very important function and making the numerical evaluation far simpler. Therefore during the calculation, a back and forth trip is done at each iteration between the real and the reciprocal space.

The numerical calculation of the structural functions h, h^d, c and c^d, from which one can compute all the other structural functions, needs the definition of an intermediate term, as

$$\begin{aligned} \gamma(r) &= h(r) - c(r), \\ \gamma^d(r) &= h^d(r) - c^d(r), \end{aligned} \tag{6.3}$$

$$\begin{aligned}\gamma(q) = h(q) - c(q) &= \frac{c^c(q)}{1-\rho c^c(q)} + \frac{c^d(q)}{(1-\rho c^c(q))^2} - c(q),\\ \gamma^d(q) = h^d(q) - c^d(q) &= \frac{c^d(q)}{(1-\rho c^c(q))^2} - c^d(q).\end{aligned} \tag{6.4}$$

thence respectively defined in real and reciprocal space. γ and γ^d are simply expressed as functions of the total and the direct correlation functions.

Using what has just been defined, the algorithm to calculate iteratively the structural functions is

1. Find reasonable guesses $c(r) = c_{\text{guess}}(r)$ and $c^d(r) = c^d_{\text{guess}}(r)$ for the direct correlation functions.

2. Fourier transform to get $c(q)$ and $c^d(q)$.

3. Calculate $\gamma(q)$ and $\gamma^d(q)$ using equation 6.4.

4. Inverse Fourier transform to get $\gamma(r)$ and $\gamma^d(r)$.

5. Calculate $c_{\text{new}}(r)$ and $c^d_{\text{new}}(r)$ using a closure relation.

6. Mix the new function with the previous one using $c_{\text{new}}(r) = \alpha c_{\text{new}}(r) + (1-\alpha)c(r)$ and $c^d_{\text{new}}(r) = \alpha c^d_{\text{new}}(r) + (1-\alpha)c^d(r)$ with $\alpha \in [0,1]$.

7. Go back to 2, unless $||c_{\text{new}}(r) - c(r)|| < \epsilon$ and $||c^d_{\text{new}}(r) - c^d(r)|| < \epsilon$ where ϵ is small.

The step number 6 of the algorithm incorporates a mixing parameter α that has the purpose of keeping the stability of the calculated functions in the process of convergence. At each iteration, a certain percentage of the newly calculated function is mixed with the old one, and this allows the spontaneous changes in the shape of the functions not to have a too dramatic effect on the calculation, while still being taken into account. This is done at the expense of calculation time.

6.1.2 Practical details

All the structural calculations have been performed using FORTRAN 90 and storing the real numbers in double precision type variables, whose precision reaches the fifteenth digit. For calculation time reasons, the choice has been made to use a well tested Fast Fourier Transform (FFT) subroutine to do the back and forth route in the reciprocal space. This subroutine has the particularity, on top of being very efficient, of being only

able to process arrays with a number of cells that follows the rule $N_{\text{struct}} = 2^p$ where $p \in \mathbb{N}^+$. This number has been chosen as $p = 12$, leading to arrays of $N_{\text{struct}} = 2^{12} = 4096$ cells. The distance between two values has been chosen as $\Delta r = 0.01$. We therefore have $\Delta q = \frac{\pi}{dr \times N_{\text{struct}}} \approx 0.077$.

The mixing parameter is chosen as $\alpha = 0.05$, a quite low value that has proved to keep the convergence on tracks. Furthermore, the calculation of the structural functions is extremely fast compared to the dynamical functions. Therefore, a little more time allocated to make sure the structural calculation are performed correctly every time, does not fundamentally change the overall calculation time. Finally, the convergence parameter as been chosen as $\epsilon = 10^{-12}$.

6.2 Phase diagrams

6.2.1 Description of the algorithm

We start with the expression that allows the calculation of the infinite time limit of the ISF, $f(q) = \lim_{t\to\infty} \phi(q,t)$:

$$\frac{f(q)}{1-f(q)} = m(q; V^{(2)}, V^{(1)}, f(q)), \tag{6.5}$$

where $m(q; V^{(2)}, V^{(1)}, f(q))$ is the memory function, in which the dependence on the vertices $V^{(2)}$ and $V^{(1)}$ as well as $f(q)$ has been made explicit. As explained in chapter 5, the different phases of the fluid are characterized by different values of $f(q)$ (in the case of the liquid and the glass) and $f^s(q)$ (in the case of the localized phase). The general example of $f(q)$ will be taken in the following, but everything is applicable to $f^s(q)$ as well.

$f(q)$ is the parameter defining the phase of the system, otherwise called the order parameter. The limit between two phases or domains corresponds to critical values of the infinite time ISF $f^c(q)$ and of the vertices $V^{(2),c}$ and $V^{(1),c}$, so that the following equation presents at least one singular solution:

$$\frac{f^c(q)}{1-f^c(q)} = m^c(q)(V^{(2),c}, V^{(1),c}, f^c(q)), \tag{6.6}$$

and the condition of singularity of the Jacobian matrix is met:

$$\det\left[\frac{1}{(1-f^c(q_i))^2}\delta_{ij} - \frac{\partial m(q_i)}{\partial f(q_j)}(V^{(2),c}, V^{(1),c}, f^c(q))\right] = 0. \tag{6.7}$$

Let us approach the liquid-glass transition line from the glass phase, i.e., the system is set in a state $(V^{(2)}, V^{(1)}) = (V^{(2),c} + v^{(2)}, V^{(1),c} + v^{(1)})$ so that the solution $f(q)$ to

equation (6.5) is nonzero. We set $f(q_i) = f^c(q_i) + (1 - f^c(q_i))^2 g(q_i)$, inject it in equation (6.5) and perform a Taylor expansion in the following way:

$$\sum_j [\delta_{ij} - \frac{\partial m(q_i)}{\partial f(q_j)}(v^{(2)}, v^{(1)}, f^c(q))(1 - f^c(q_i))^2 \Big] g(q_j) = m(q_i)(v^{(2)}, v^{(1)}, f^c(q)) - (1 - f^c(q_i))g(q_i)^2 + \frac{1}{2}\sum_{j,k} \frac{\partial^2 m(q_i)}{\partial f(q_j) f(q_k)}(v^{(2)}, v^{(1)}, f^c(q))(1 - f^c(q_j))^2 (1 - f^c(q_k))^2 g(q_j) g(q_k) + O(v^{(2)} g, v^{(1)} g, g^3). \tag{6.8}$$

The matrix on the l.h.s. is equivalent to the Jacobian of equation (6.5), and has therefore a unique zero eigenvalue. We define the two eigenvectors $e(q_i)$ and $\hat{e}(q_i)$ respectively on the right and on the left of this matrix, and both associated to the zero eigenvalue. We apply them the following constraints:

$$e(q_i) > 0 \quad \hat{e}(q_i) > 0 \quad \sum_i \hat{e}(q_i) e(q_i) = 1 \quad \sum_i \hat{e}(q_i)(1 - f^c(q_i)) e(q_i)^2 = 1. \tag{6.9}$$

A solution exists only if

$$\sum_i \hat{e}(q_i) \Big[\, m(q_i)(v^{(2)}, v^{(1)}, f^c(q)) - (1 - f^c(q_i)) g(q_i)^2 + \frac{1}{2} \frac{\partial^2 m(q_i)}{\partial f(q_j) f(q_k)}(v^{(2)}, v^{(1)}, f^c(q))(1 - f^c(q_j))^2 (1 - f^c(q_k))^2 g_j g_k \Big] = 0. \tag{6.10}$$

This solution is of the form $g(q_i) = e(q_i) g$ at the main order.
Finally, we define λ as

$$\lambda = \frac{1}{2} \sum_{i,j,k} \hat{e}(q_i) \frac{\partial^2 m(q_i)}{\partial f(q_j) f(q_k)}(v^{(2)}, v^{(1)}, f^c(q))(1 - f^c(q_j))^2 (1 - f^c(q_k))^2 e(q_j) e(q_k) \tag{6.11}$$

This parameter is called the exponent parameter and is extremely important in the calculation of the transition lines. When this parameter is calculated on a transition line, its value defines the way the dynamical variables decay towards their final value. Furthermore, and this is the feature that will be interesting in the case of the calculation of the phase diagram, the value of λ indicates the end of a transition line. Usually, this parameter is expected to be $0 \leq \lambda \leq 1$ for a continuous or diffusion-localization transition line, and $0.5 \leq \lambda \leq 1$ for a discontinuous transition line. In any cases, when $\lambda = 1$, the transition line is known to reach its end.

A phase diagram consists of transition lines separating the different phases the fluid can adopt, and the calculation of the transition lines is done by evaluating the infinite time limit of the ISF $f(q)$, and subsequent calculations of the eigenvalue of the Jacobian and of the parameter λ to quantify the position on the transition line.

Concerning the phase diagrams presented in chapter 5, the x-axis has been chosen as the density of the fluid ρ, and the y-axis as the amplitude of the potential δ, and the correlation length of the potential taken as a constant. Therefore due to the way they behave, the continuous and the localization transition lines were created by varying δ at constant values of ρ and of the correlation length of the potential σ. This example will be taken in the following, but the procedure is applicable to the discontinuous transition line as well by varying the density instead of the amplitude.

The algorithm used to calculate the transition lines is a dichotomy over the value of a varying parameter, here taken as δ for the example :

Initialization

1 For a given value of ρ, make an educated guess of a value of δ that is likely to be close to the critical value δ^c.

2 Calculate the vertices, and by an iteration process evaluate both the memory function and the order parameter $f(q)$.

3 Use power iteration to calculate the eigenvalue E of the Jacobian of the system.

4 If $E < 0$ (resp. $E > 0$) we have $\delta < \delta^c$ (resp. $\delta > \delta^c$). Increment (resp. decrement) δ by an arbitrary value and repeat step 2 until $E > 0$ (resp. $E < 0$). The two values of δ that are respectively below and above δ^c are denoted δ^{liq} and δ^{glass}.

Refinement

5 Set $\delta = \frac{\delta^{\text{liq}}+\delta^{\text{glass}}}{2}$ and calculate the vertices, memory function, order parameter and finally the eigenvalue E.

6 If $E < 0$ (resp. $E > 0$) set $\delta^{\text{liq}} = \delta$ (resp. $\delta^{\text{glass}} = \delta$) and go back to step 4 until $|E| < \epsilon$ where ϵ is chosen small.

7 Evaluate the value of λ. If $\lambda > 1$, the end of the transition line has been met and the calculation is stopped. Otherwise, increment ρ and start over at step 1. A refinement of the position of the end of the transition line can be done after the whole transition line has been drawn.

6.2.2 Practical details

The evaluation of $f(q)$, $f^s(q)$, the eigenvalue, and λ has been performed using FORTRAN 90 and double precision type variables for the evaluation of the real numbers and arrays.

The number of iterations, especially to calculate the value of the order parameter $f(q)$ can be huge, this part of the calculation is one of the most time-consuming ones. Therefore,

in order to make the calculations faster, and as concern for memory consumption, all the functions have been stored and calculated on arrays of $N^d = 300^d$ cells, where d is the dimension of the array. Knowing that the structural functions have been evaluated on arrays of $N_{\text{dynamics}} = 4096$ cells, calculating the vertices is done with an obvious loss of information. Every two values until $N_{\text{structure}} = 600$ is sampled out to calculate the vertices in order to account for the short distance correlations, which contain most of the information.

The iteration over $f(q)$ is done until $|f^i(q) - f^{i+1}(q)| \leq \epsilon_f$ where i denotes the iteration and we choose $\epsilon_f = 10^{-12}$. The continuous and diffusion-localization transition lines are calculated by varying ρ regularly by steps of $\Delta\rho = 0.01$, and for each value of ρ, the critical amplitude δ^c is framed using dichotomy until $|E^{\text{liquid}} - E^{\text{glass}}| \leq 10^{-6}$ where E^{liquid} and E^{glass} are respectively the eigenvalues calculated in the liquid and the glass side of the transition line.

The discontinuous transition is calculated by first varying δ regularly and choosing the number of steps according to the expected height of the phase diagram, until $|E^{\text{liq}} - E^{\text{glass}}| \leq 10^{-4}$. The calculation of the transition line is stopped when the value of $\lambda = 1$ is reached. When the transition line becomes horizontal for certain closure relations and values of σ (typically the high values), the discontinuous transition line is calculated by varying the density.

Due to the structure of the solutions, two types of junctions are expected to happen between the continuous and the discontinuous transition lines. The first way these two lines can intersect is by connecting at the very point where $\lambda = 1$ for both of them, which is only encountered in this work for the low values of the correlation length. Most of the time however, the discontinuous transition line cuts through the continuous one, which is discarded beyond this point. The reasons for this lies again in the structure of the solutions and the demonstration will not be explicited here. The discontinuous transition line always prevails over the continuous transition line.

The precision chosen to frame the discontinuous transition line is much lower compared to the continuous case, because the convergence of $f(q)$ is slower, and becomes even slower as the point $\lambda = 1$ is approached. The typical convergence of a calculation when the point is taken in the liquid phase is very different from the case of the glass phase, and both are represented in figure 6.1.

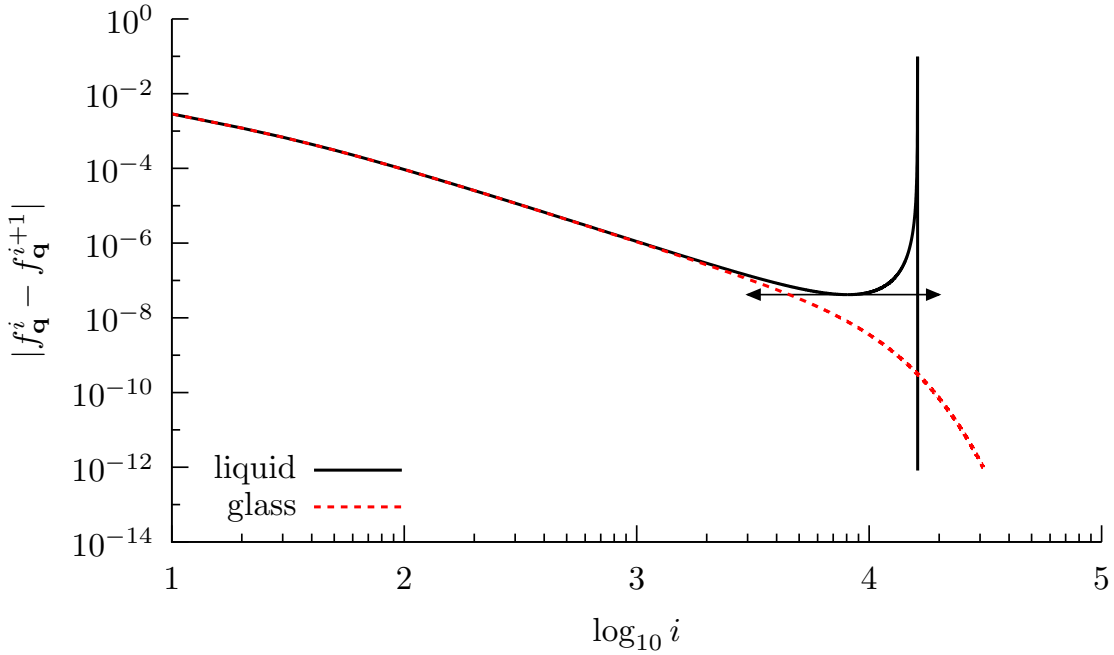

Figure 6.1: Convergence of the calculation of the location of a critical value ρ_c at a value of the amplitude $\delta = 1.0$ in the liquid phase (plain black line) and the glass phase (dashed red line) as a function of the number of iterations. The double arrow indicates a turning point.

In the glass, the difference between $f^i(q)$ ad $f^{i+1}(q)$ decreases steadily until convergence is reached, while the pattern in the case of the liquid phase presents a minimum followed quickly by a maximum and a fast decrease to convergence. The main difference lies in the fact that the convergence in the liquid phase presents a turning point, which is pinpointed in figure 6.1 by a tangent line. In the course of the calculation, this turning point can be very easily found. Since it is a feature of only the liquid phase, a convergence process can be stopped as soon as a turning point is found, and the phase of the fluid determined on this sole criteria, which speeds up the calculation of the transition line.

Moreover, taking the value of the $f(q)$ array on the turning point to calculate the vertices and the eigenvalue allows for a greater precision on the calculation of λ than usual convergence. This allows for a very good refinement of this important parameter without the cost of carrying a calculation to full convergence.

6.3 Dynamical functions

6.3.1 Description of the algorithm

The calculation of the dynamical variables such as the intermediate scattering function (ISF), the mean squared displacement (MSD), and the non-Gaussian parameter is done by iteratively solving the MCT equations presented in chapter 4, using standart methods developped in (Fuchs *et al.*, 1991; Franosch *et al.*, 1997b; Fuchs *et al.*, 1998). The evaluation of these functions goes through the evaluation of the memory kernel, which in turn is defined in terms of the structural functions presented in chapter 2. For calculation time reasons, the dynamical functions have been defined on arrays of $N_{\text{dynamics}} = 300$ cells. The structural functions therefore have to be sampled on the same array, and this can be therefore only done by loosing information, the initial structural functions being sampled on a $N_{\text{structure}} = 4096$ array. Therefore, one of two values has been taken, effectively stopping the sampling at $N_{\text{structure}} = 600$, which did not seem to create numerical discrepancies.

The calculation of the dynamical variables has been made as follows.

Let us consider the following generalized Langevin equation for the collective ISF, as described in chapter 4:

$$\tau(q)\dot{\phi}(q,t) + \phi(q,t) + \int_0^t m(q,t-\tau)\dot{\phi}(q,\tau)d\tau = 0. \tag{6.12}$$

The following will focus first on a discretization of this equation, followed by the description of the iterative algorithm used to solve it. This is done for the example with the generalized Langevin equation for the collective ISF, but the same scheme can be applied to solve its self counterpart, and the mean squared and quartic displacements, whose equations follow similar rules.

We can rewrite this equation in the following way:

$$\phi(q,t) = m(q,t) - \frac{d}{dt}\int_0^t m(q,\tau)\phi(q,t-\tau)d\tau - \tau(q)\dot{\phi}(q,t). \tag{6.13}$$

First we rewrite the integral $I(q,t) = \frac{d}{dt}\int_0^t m(q,\tau)\phi(q,t-\tau)d\tau$, introducing $T \approx t/2$:

$$I(q,t) = m(q,T)\phi(q,t-T) + \int_0^{t-T} \dot{m}(q,t-\tau)\phi(q,\tau)d\tau + \int_0^T \dot{\phi}(q,t-\tau)m(q,\tau)d\tau \tag{6.14}$$

Defining $t_1 < t_2 < t$ and developing at the third order for any two dummy variables $A(q,t)$ and $B(q,t)$:

$$\int_{t_1}^{t_2} \dot{A}(t-\tau)B(\tau)d\tau \approx \frac{A(t-t_1) - A(t-t_2)}{t_2 - t_1}\int_{t_1}^{t_2} B(\tau)d\tau, \tag{6.15}$$

which allows to rewrite equation (6.14) in a way that can be discretized. We define $t = nh$, $T = Nh$ and $t_k = kh$, where $n, N, k \in \mathbb{N}^+$, and $h \in \mathbb{R}^+$. This allows to represent all the functions we want to compute on arrays of N values, where n and k label cells of the arrays and h is to be chosen small in order to have a good precision. We define the discretized ISFs as follows:

$$\begin{aligned} \phi_k &= \phi(q, kh), \\ \Phi_k &= \frac{1}{h}\int_{(k-1)h}^{kh} \phi(q,t)dt, \end{aligned} \tag{6.16}$$

and the discretized memory functions:

$$\begin{aligned} m_k &= m(q, kh), \\ M_k &= \frac{1}{h}\int_{(k-1)h}^{kh} m(t)dt. \end{aligned} \tag{6.17}$$

We apply (6.15) and use the notation just defined on (6.14):

$$I_n = m_N\phi_{n-N} + \sum_{k=1}^{N}(\phi_{n-k+1} - \phi_{n-k})M_k + \sum_{k=1}^{n-N}(m_{n-k+1} - m_{n-k})\Phi_k. \tag{6.18}$$

We define C_n as

$$C_n = m_N\phi_{n-N} - m_{n-1}\Phi_1 - \phi_{n-1}M_1 + \sum_{k=2}^{N}(\phi_{n-k+1} - \phi_{n-k})M_k + \sum_{k=2}^{n-N}(m_{n-k+1} - m_{n-k})\Phi_k, \tag{6.19}$$

and finally, we write (6.18) as

$$m_n - I_n = m_n(1 - \Phi_1) - \phi_n M_1 - C_n, \tag{6.20}$$

which is the first term on the r.h.s. of equation (6.13). In order to fully discretize this expression, we need to define the derivative of the ISF, using a common approximation:

$$\dot{\phi}_n = \frac{3\phi_n - 4\phi_{n-1} + \phi_{n-2}}{2h} \tag{6.21}$$

Finally, plugging these expressions in equation (6.13) and rearranging, we get

$$\phi_n = \frac{m_n(1 - \Phi_1) - D_n}{1 + M_1 + 3\frac{\tau(q)}{2h}}, \tag{6.22}$$

with

$$D_n = C_n - \frac{\tau(q)}{2h}(4\phi_{n-1} - \phi_{n-2}). \tag{6.23}$$

The times spanned by the relaxation of the dynamical variables is huge, usually of the order of 10^{12}, but sometimes longer, when the calculation is performed close to a transition line, where the dynamics of the system is by definition very slow. Storing all the values of $\phi(q,t)$ would require a quantity of memory that computer at the time this work is put together cannot support. Therefore, the calculation has to be done in an iterative manner, and information has to be lost carefully at each step.

Initialization

The ISF is stored on an array of $N = 2p$ cells, and the time step h_0 is chosen so that $t_0 = Nh_0 \ll \min_q \tau(q)$, where the subscript 0 indicates that the value of h is meant to change at each iteration. The first $N/2$ values of the array are initialized using a Taylor expansion of the ISF:

$$\phi(q,t) = 1 - \frac{t}{\tau(q)}, \tag{6.24}$$

and the integrals are calculated using the trapezoidal rule:

$$\begin{aligned} \Phi_k &= \frac{1}{2}(\phi_{k-1} + \phi_k), \qquad \text{with the initial condition } \phi_0 = 1, \\ M_k &= \frac{1}{2}(m_{k-1} + m_k), \qquad \text{where } m_0 \text{ has to be explicitly calculated.} \end{aligned} \tag{6.25}$$

Concerning the NGP, the first and the second derivatives of the self ISF with respect to the wavevector have to be calculated at this step for the initialized array, using simple numerical derivation:

$$\begin{aligned} \frac{d}{dq}\phi^s_{k,q} &= \frac{\phi^s_{k,q-1} - \phi^s_{k,q+1}}{2h_q}, \\ \frac{d^2}{d^2q}\phi^s_{k,q} &= \frac{\phi^s_{k,q-1} - 2\phi^s_{k,q} + \phi^s_{k,q+1}}{h_q^2}. \end{aligned} \tag{6.26}$$

The integrals and the derivatives have to be stored in N_{dynamics} sized arrays as well.

Propagation

The following propagation has to be done for $N/2 + 1 \leq k \leq N$, and sums up to calculating the values of the ISF and the memory function (possibly the derivatives of the self ISF in the case of the mean quartic displacement) for the second half of the array.

1. Calculate C_n and D_n, which requires values of the ISF and the memory functions and the integrals at times $1 \leq k \leq N/2$.

2. Take a guess ϕ^i_n, and calculate the memory function as

$$m^i_n(q_1) = \sum (q_1, q_2, q_3) V^{(2)}(q_1, q_2, q_3) \phi^i_n(q_2) \phi^i_n(q_3) + V^{(1)} \phi^i_n(q_2). \tag{6.27}$$

3. Calculate a new value of $\phi_n^{i+1}(q)$ using equation (6.22), which will be taken as a guess for the next iteration.

4. Start over at step 2 until $|\phi_n^i - \phi_n^{i+1}| < \epsilon$, where ϵ is a small real number.

5. Calculate $m_n^i(q_1)$ one last time.

The guess at the first step of this propagation is chosen as $\phi_n^i = \phi_{n-1}$. After the first propagation, the values calculated for $N/2+1 \leq k \leq N$ have to be written down.

Reduction

Because of the fact that C_n has to be calculated using *all* the previous values of the ISF and the memory function, one would need, in order to get a theoretically perfect calculation of the dynamical variables, to dynamically allocate the arrays after each first propagation. However as stated above, the times spanned by the MCT calculation are usually very long, due to the fact that the phenomena that we aim to observe happen at critical values of the parameters describing the system. Therefore, such a simple solution would lead to a huge amount of information to be stored, and therefore be impossible. We can however take advantage from the fact that the long time dynamics shows less and less dependence over the short time dynamics as the time increases: this second propagation aims to reduce the information in a smart way.

First, for all $1 \leq k \leq N/2$, we do the following:

$$\begin{aligned} \phi_k &= \phi_{2k}, \\ \Phi_k &= \frac{1}{2}(\Phi_{2k-1} + \Phi_{2k}), \\ m_k &= m_{2k}, \\ M_k &= \frac{1}{2}(M_{2k-1} + M_{2k}). \end{aligned} \tag{6.28}$$

Then, for all $N/2+1 \leq k \leq N$, we calculate the integrals using the Simpson formula:

$$\begin{aligned} \Phi_k &= \frac{\phi_{2k} + 4\phi_{2k-1} + \phi_{2k-1}}{6} \\ M_k &= \frac{m_{2k} + 4m_{2k-1} + m_{2k-1}}{6} \end{aligned} \tag{6.29}$$

and finally, we set $h' = 2h$ as the new time step. This whole process has the purpose of effectively doubling the time step h. Starting up again with a propagation will lead to a new series of values calculated in a much faster way. Propagation followed by reduction is to be applyied as much as needed, typically until convergence is met, or a certain number of values have been calculated.

6.3.2 Practical details

The calculation of the dynamical variables has been performed using FORTRAN 90 and double precision type variables for the evaluation of the real numbers and arrays. The functions have been stored in arrays of size $Q \times 2T$ where $Q = 300$ and $T = 200$. The functions are calculated for each value of q one time with the initialization and propagation steps, and are written down in files, followed by a reduction step. The propagation is performed again and the newly calculated values written down in the same files. This process is followed until $|\phi(\mathbf{q})^t - \phi(\mathbf{q})^{t+1}| < \epsilon$ with $\epsilon = 10^{-12}$.

Chapter 7

Preliminary simulation study

When working with the Mode Coupling Theory, the problem one immediately runs into is the comparison with experiments, which is something that could be done to an extent with the work of Evers *et al.* (2013a), Evers *et al.* (2013b), Bewerunge *et al.* (2016b), and Bewerunge (2016). Unfortunately, due to the difficulties pertaining to the difference in dimensionality, and the inability to span the very long and very short time scales experimentally, useful comparison was often considered only as a way to confirm the existence of general trends that MCT could sometimes capture. Moreover, it is unlikely that experiments could measure the critical dynamics happening at long times any soon, due to the technical difficulty of doing so.

When the MCT had seemingly been milked out of all meaningful results, the logical step forward has been clearing up the way for potential future results. These future results have to come from simulation studies which do have but little constrains on the time scales measured and the precision of the outcome, at least for not too extreme situations. As a way of simplifying the implementation, the method has been chosen to be a Monte Carlo method performed on hard spheres placed in a three-dimensional box with periodic boundary conditions, where the positions of the particles as well as the Gaussian random potential defined in chapters 1 and 2 are set on a fine grid.

The diameter of the particles is taken as unity, and the simulations done in a $L \times L \times L$ box with $L = 10$, divided into $P \times P \times P$ points with $P = 200$, over which N particles are placed. The arrangement of the particles at the beginning of the simulation is done by creating a crystal of N particles with lattice constant $d = \lfloor \frac{P^3}{N^{1/3}} \rfloor$. Placing the particles in this way requires a step of relaxation before starting any actual data collection, so that the rather practical but unrealistic starting crystal does not bring any contribution to final structural results.

7.1 Generation of a random potential

The reliability of the Monte-Carlo simulations stands on the quality of the potential generated, which contrary to the case of the theoretical work cannot be included in the study through its covariance alone. This time, the potential has to have a value on each point of the grid, which in part simplifies the problem by requiring only a finite number of well defined points, on which the potential has a known value that can be used throughout the entire calculation. The scheme developed by Bertschinger (2001) for cosmological large scale calculations provides an easy and quick way to generate such a potential on a grid that presents periodic boundary conditions. The potential is generated according to

$$\zeta(\mathbf{r}) = \int d^3\mathbf{k} e^{i\mathbf{k}.\mathbf{r}} T(k)\xi(\mathbf{k}), \tag{7.1}$$

where $\xi(\mathbf{k})$ is the Fourier transform of a Gaussian white noise, and $T(k)$ is related to the covariance of the random potential as

$$T(k) = \sqrt{K(k)}, \tag{7.2}$$

where $K(k)$ is the Fourier transform of the covariance of the potential, here chosen as a Gaussian function of the form

$$k(r) = \varepsilon^2 e^{-\left(\frac{r}{\sigma}\right)^2} \tag{7.3}$$

which can be Fourier transformed into

$$K(k) = \varepsilon^2(\pi\sigma^2)^{3/2} e^{-k^2\sigma^2/4}. \tag{7.4}$$

The discretized process starts with the generation of one random number per point of the grid, i.e., P^3 points. These random numbers have to follow a Gaussian distribution, and the Box-Muller algorithm gives a quick and efficient way to do this. First, two random numbers u and v are generated using a uniform random number generator. We then calculate $u' = 2u - 1$, $v' = 2v - 1$, and

$$w = u_1' + u_2', \tag{7.5}$$

and finally, a couple of Gaussian random numbers is generated as

$$\begin{aligned} z_1 &= u'\sqrt{\frac{-2\log w}{w}}, \\ z_2 &= v'\sqrt{\frac{-2\log w}{w}}. \end{aligned} \tag{7.6}$$

One such number is generated on each point of the grid. The variance of this Gaussian distribution has to be N^3 and therefore every random number is scaled accordingly.

Equation (7.1), which can be rewritten as a convolution product (Salmon, 1996), can be discretized as

$$\zeta(\mathbf{r}) = \sum_{\kappa} e^{\frac{i2\pi}{N}\kappa.\mathbf{r}} T(\kappa)\xi(\kappa), \tag{7.7}$$

where $\kappa = \frac{\mathbf{k}L}{2\pi}$ has three components, each in $[-N/2, N/2[$.
The correct generation of the disordered potential is at the core of the validity of the results, and is thus a step of major importance. Its validation will therefore be the object of the first results presented in this chapter.

7.2 Calculation of the disconnected structural quantities

The calculation of the total correlation function and associated quantities is done in a straightforward way, by sampling the positions of the particles on a regular basis during the calculation. However, separating the connected from the disconnected requires the use of a more sophisticated method, adapted from Meroni *et al.* (1996).

The disconnected total correlation function is expressed as a function of the two-point density correlation function $\Psi(\mathbf{r}_1, \mathbf{r}_2) = \langle\rho(\mathbf{r}_1)\rangle\langle\rho(\mathbf{r}_2)\rangle$. We note that in that expression only the ensemble average is taken. The disorder average is to be evaluated later on. In the context of a Monte Carlo simulation, the one-point density can be calculated as

$$\rho(\mathbf{R}) = \frac{1}{v}\sum_{i=1}^{N} \Delta_{\mathbf{R}-\mathbf{r}_i}, \tag{7.8}$$

where v is the volume of a single cell of the discretized box, and $\Delta_{\mathbf{R}-\mathbf{r}_i}$ acts like a Kronecker delta in the way that it equals 1 if $\mathbf{r}_i = \mathbf{R}$ and 0 otherwise. The two-point density correlation can be discretized as

$$\Psi(\mathbf{r}) = \frac{1}{N^3}\sum_{\mathbf{R}} \langle\rho(\mathbf{R}+\mathbf{r})\rangle\langle\rho(\mathbf{R})\rangle, \tag{7.9}$$

which can be evaluated by taking the inverse Fourier transform of the following expression:

$$\psi(\mathbf{k}) = \rho(\mathbf{k})^*\rho(\mathbf{k}), \tag{7.10}$$

with $\rho(\mathbf{k})$ the Fourier transform of $\langle\rho(\mathbf{R})\rangle$.
Taking the average over different disorder realizations allows one to recover to disorder averaged quantity, and finally $\Psi(r)$ is obtained by regrouping all $\Psi(\mathbf{r})$ with the same r. We eventually calculate the disconnected total correlation function $h^d(r)$ as

$$h^d(r) = \frac{\overline{\Psi(r)}}{\rho^2} - 1. \tag{7.11}$$

7.3 Some results

As a validation of the generation of the potential and as a way to introduce results from this simulation study, we may calculate the usual and disconnected total correlation functions $h(r)$ and $h^d(r)$. These functions were described in chapter 2, and in the case of a system with no hard core, i.e., an ideal gas, they are strictly equal. Furthermore, the exact result for these functions is known and coincides with the result of the HNC closure relation as $h(r) = h^d(r) = e^{\beta^2 k(r)} - 1$. Comparison between the simulated disconnected and usual total correlation functions, and the analytic result is presented in figure 7.1, for varying values of the relative amplitude from $\delta = 0.5$ to $\delta = 2.0$.

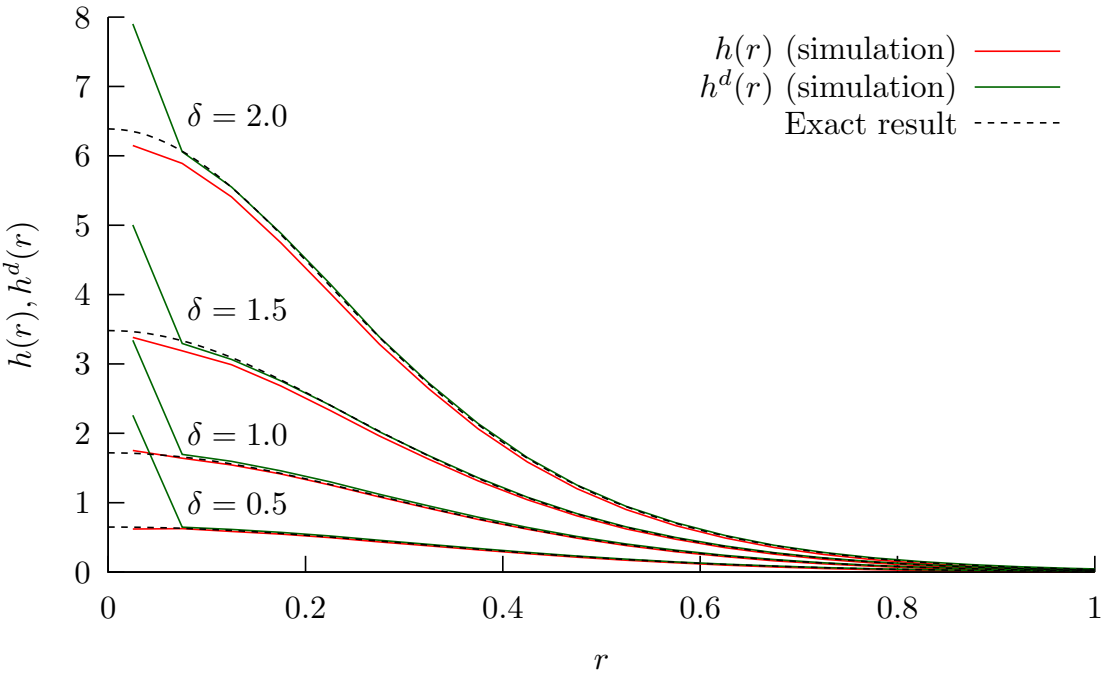

Figure 7.1: Disconnected (green curves) and usual (red curves) total correlation functions evaluated by a Monte Carlo simulation of an ideal gas (no interaction between the particles) in a Gaussian random potential with amplitude $\delta = 0.5, 1.0, 1.5, 2.0$ and correlation length $\sigma = 0.5$. 250000 Monte Carlo iterations have been performed, and the positions of the particles have been sampled every 50 iterations to calculate the correlation functions. 50 potentials have been generated with the same parameters to get the disorder averaged quantities. The dashed black curves represent the analytic result.

The simulated functions have not been calculated at $r = 0$, where they are prone to large normalization errors. Furthermore, it can be noticed that the result at $r = \Delta r$ concerning the disconnected total correlation function is very imprecise, compared to the

usual total correlation function. This is entirely an artifact of the method, due to the discretization of the simulation box, creating a self contribution of the two-point density correlation function at that distance. This contribution vanishes very slowly when the refinement of the discretization and the number of potentials sampled increase.

Clearly, apart from the discrepancy at short distance for the simulated disconnected total correlation function, the curves are very similar. This constitutes therefore both a confirmation of the proper generation of the potential, and of the algorithm used to evaluate $h(r)$ and $h^d(r)$. The curves are expected to approach the analytic solutions more and more, as more iterations are done, and more potentials are sampled.

As interesting as the ideal gas is in order to validate the generation of the potential and the calculation of the structural properties, the real interest lies in the study of a hard-sphere fluid at different densities. During the short time that the calculations could be ran, we managed to increase the density until $\rho = 0.2$ while keeping reasonable calculation times. Figure 7.2 shows a comparison of the usual and disconnected total correlation function for a hard-sphere fluid of densities $\rho = 0.1$ and $\rho = 0.2$. This short range of densities obviously does not constitute an extensive study, but it allows a few quick and general conclusions.

Concerning the usual total correlation function, a first conclusion is that the influence of the potential grows very slowly when the amplitude increases. Second, it appears that the total correlations are more important when the density is higher, due to the increased particle-particle interactions. This is all expected.

Concerning the disconnected total correlation function, the influence of the potential is much bigger, and grows very fast with the increase of the amplitude. We note the apparition of a negative peak around $r = 1$, a fact that can be seen in the theoretical calculations in chapter 3 as well. Comparing the cases of $\rho = 0.1$ and $\rho = 0.2$, we see that the potential has a greater influence on the disconnected correlations at lower values of the density. When the density increases, it seems that the density related correlations erase the potential related correlations, and this points to the reentrance of the diffusion-localization line observed in chapter 5. Which, as it has been discussed in that chapter, is caused exactly by this phenomenon. The reentrance, which has already been compared to experimental isodiffusivity lines, receives here a further confirmation. We therefore expect the disconnected correlations to collapse even more with an increase of the density, until a certain high value of the density where they would start to grow again.

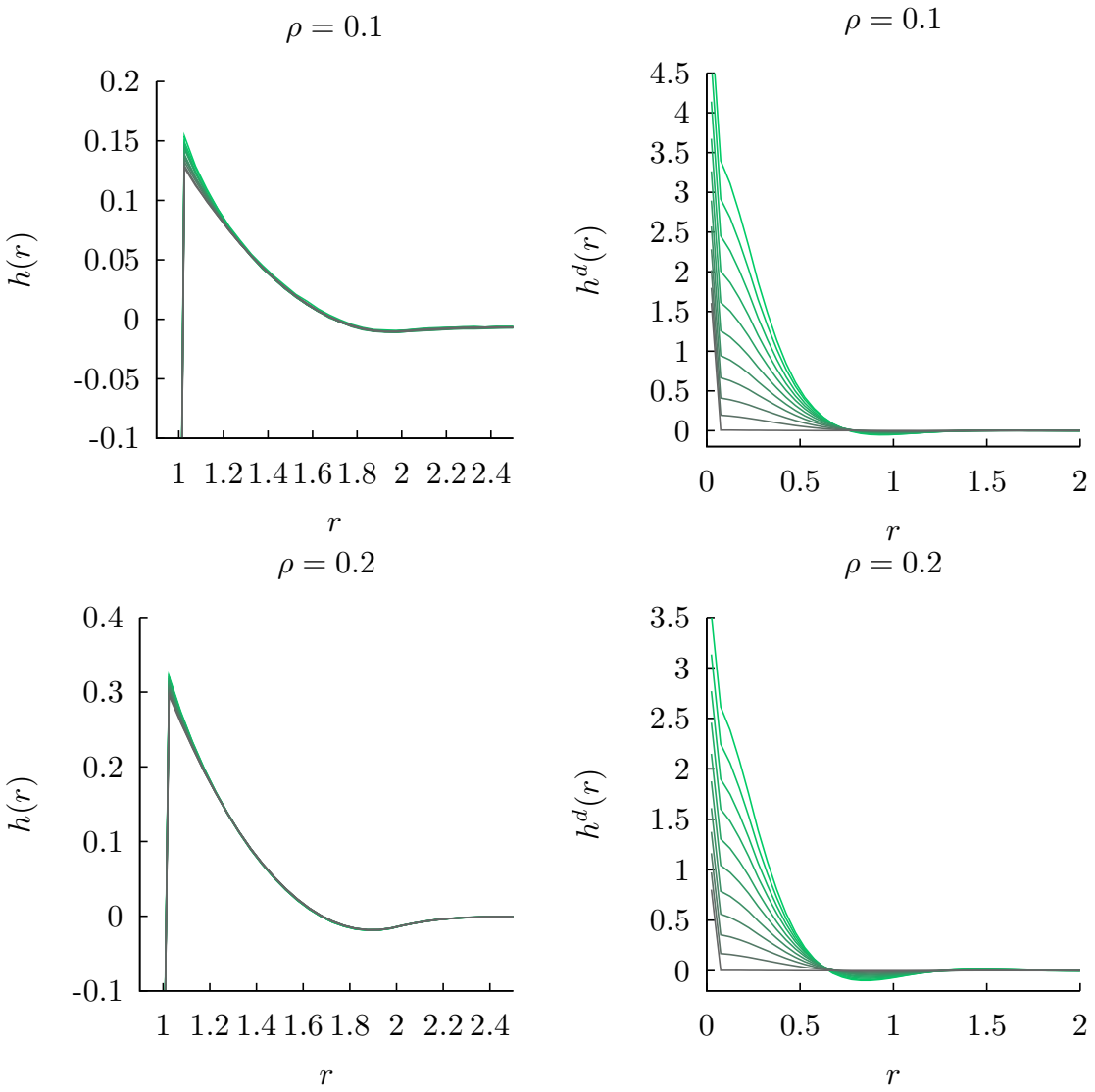

Figure 7.2: **(left)** Usual and **(right)** disconnected total correlation functions evaluated by a Monte Carlo simulation of a hard-sphere fluid in a Gaussian random potential with amplitude $\delta = 0.0$ to $\delta = 2.0$ and correlation length $\sigma = 0.5$. The amplitude of the potential is proportional to the saturation of the color of the curve. 250000 Monte-Carlo iterations have been performed, and the positions of the particles have been sampled every 50 iterations to calculate the correlation functions. 50 potentials have been generated with the same parameters to get the disorder averaged quantities.

Among the dynamical variables, the MSD is one that is very easy to evaluate in the context of a simulation, since it only needs the position of the particles with almost

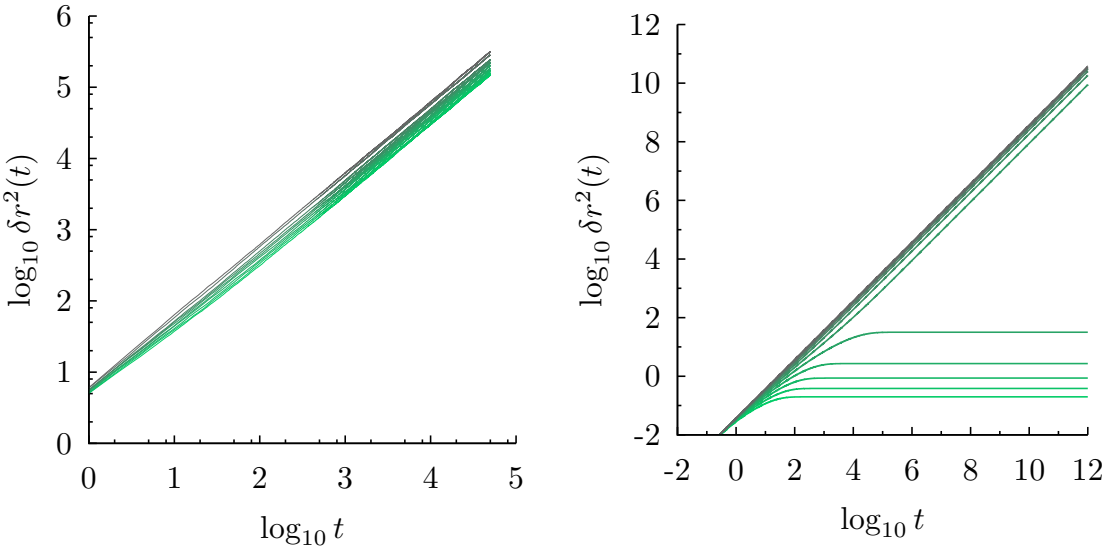

Figure 7.3: **(left)** MSD evaluated by a Monte Carlo simulation of an ideal gas in a Gaussian random potential with increasing amplitude $\delta = 0.0$ to $\delta = 2.0$ and correlation length $\sigma = 0.5$. 250000 Monte-Carlo iterations have been performed, and 50 potentials have been generated with the same parameters to get the disorder averaged MSD. **(right)** MSD calculated for the same parameters using MCT, and the OZ equation together with the HNC closure relation to get the structural correlation functions.

no treatment. Figure 7.3 shows a comparison between the simulated MSD and the one calculated using the MCT framework.
Quite strikingly, the two pictures show very different results for sets of parameters that are identical. Clearly, the shape of the MSD in the case of the MCT calculation is ruled by the presence of the diffusion-localization transition line, located at $\delta_c = 1.14$ at zero density, leading to the apparition of a plateau of the MSD at $\delta > \delta_c$. This informs us about the fact that MCT overestimates the correlations of the fluid, leading to an underestimation of the value of the critical values, a fact that is very well known concerning this theory. In the case of the simulated MSD, an increase of δ leads to the slight but noticeable apparition of a subdiffusive regime at intermediate times, followed by a return to a diffusive regime at long times, no plateau is observed. In this way, the simulation result better compares with the second panel of figure 1.3, which shows the experimental result from Evers *et al.* (2013a). Both in the case of the simulation and the experimental result, a simple subdiffusive regime followed by a return to normal diffusion is observed.

However, no quantitative comparison can be made, since the dimensionality is different, and it is unclear how the power of the laser used to generate the speckle and the theoret-

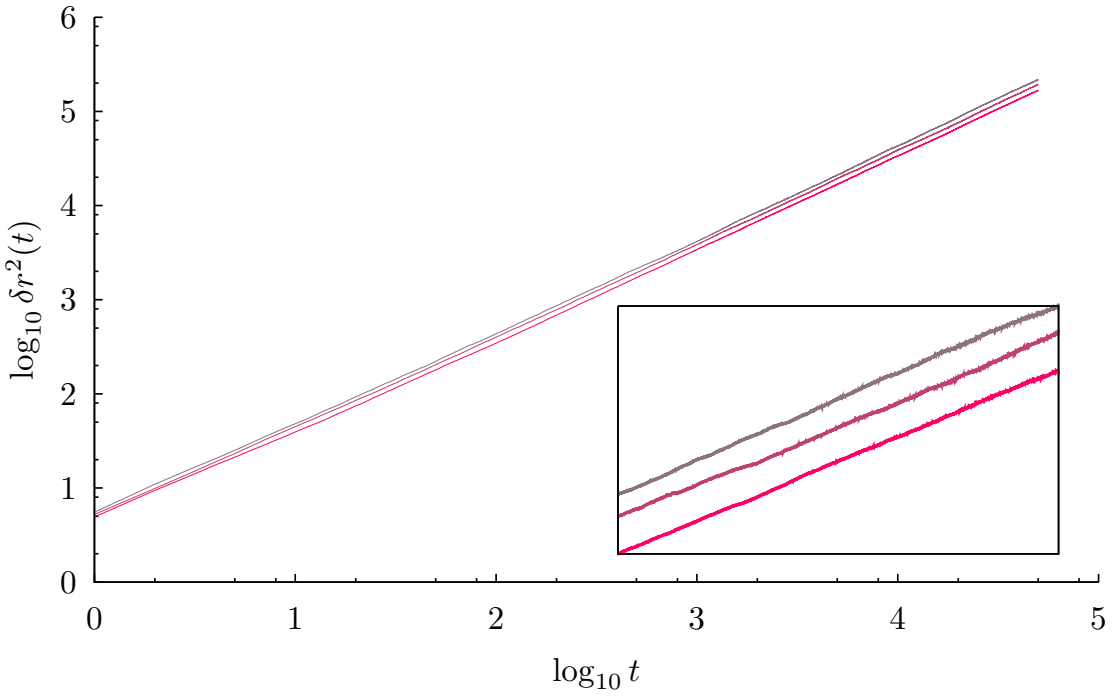

Figure 7.4: MSD evaluated by a Monte Carlo simulation of a hard-sphere fluid of density $\rho = 0.0, 0.1, 0.2$ in a Gaussian random potential of amplitude $\delta = 1.0$ and correlation length $\sigma = 0.5$. The value of the density is proportional to the saturation of the curve. 250000 Monte-Carlo iterations have been performed, and 50 potentials have been generated with the same parameters to get the disorder averaged MSD. The inset curve is a zoom.

ical parameter δ exactly relate to each other. In the future, exploration of higher values of the amplitude will be necessary, in order to eventually observe a transition to arrest, and a study of the links that δ and the laser power have will be necessary to get the full picture. The local exponent is too noisy to be exploited: a bigger set of potentials will have to be tested in order to create an exploitable picture.

Finally, the case of a hard-sphere fluid at low densities ($\rho = 0.0$ to $\rho = 0.2$) has been investigated, in an amplitude range identical to what has been done in figure 7.3. Figure 7.4 shows the MSD calculated at the same value of the amplitude $\delta = 1.0$, and increasing density $\rho = 0.0, 0.1, 0.2$.
As the density increases, the value of the MSD at a given time decreases, while keeping the slope of one, characteristic of a liquid phase. The density scanned here are very low, and no significant change was to be expected. However, the trend is good, and high densities will very probably yield to a liquid-glass transition through cage effect. It is furthermore expected that the density of transition decreases with an increase of δ. This

would be an indicator of the recession of the discontinuous transition line, as seen from the MCT calculations.

Building a full phase diagram in this way would be very difficult, as it appears that the critical amplitudes needed to create a continuous liquid-glass transition are very high. We postulate that the diffusion-localization transition line (see chapter 5) is the ultimate limit that an experiment or a simulation can reach, and that the amplitude and laser power needed to do so is very high. The reason for this is that in the context of Brownian dynamics, a particle is able to borrow virtually an infinite amount of energy from the bath. Therefore, a Gaussian potential will never be able to trap a particle for an infinite time, and dynamical arrest may never be possible for the same reason. However, it may be observed that a particle experiences trapping, and even a glass phase, for times that are, given any human consideration, infinite. Considering this, hope remains as for an experimental phase diagram can be one day built. In the mean time, simulation remains the best option, and we hope for interesting outcomes to be observed.

Chapter 8

Conclusion

Throughout this work, the focus has been set on finding a new way to explore the dynamics of a fluid plunged in a smooth disordered potential. The early theoretical research on the percolation transition and the development of experimental approaches to track and measure the diffusion of individual particles has led to the discovery of complex anomalous diffusion phenomena. These studies were supported by a few numerical experiments, but lacked a theoretical understanding, which is the point of the present work. Furthermore, the previous studies often only considered the case of a two-dimensional fluid. In this work, the system has been modeled as a hard-sphere fluid in a Gaussian random potential with Gaussian correlation function, in order to account for the size of the light spots in a real laser speckle. Furthermore the system is three-dimensional, a constraint inherent to the theory, that hopefully opens new perspectives in the field.

The first results account for the structural properties of the fluid, that have been calculated using the OZ equation and closure relations. General and expected results such as the increase of the disorder-induced and density-induced correlations with the increase of, respectively, the amplitude of the potential and the density of the system have been checked. It has been found that the correlation length of the potential plays a role in increasing the density correlations, which is interpreted in terms of structural scenarios. Furthermore, the disorder-induced correlations experience a change of regime at high values of the density, compared to low values. This result hints to a reentrant behaviour that is observed concerning the dynamics of this system. All these results have been obtained using the HNC closure relation, which has been, for many reasons, chosen as the most realistic one. In order to be complete, a comparison of the different closure relations that have been tried is necessary. Study shows surprisingly similar results between HNC, PY, MSA and EXP. As has been observed later on, the dynamics are quantitatively very different in these cases, which shows a great sensitivity of the latter to changes in the structure of the fluid. Finally, the major discrepancies of two of the closure relations, PY and EXP, have been studied. Due to uncontrolled approximations, the calculation

of the structural properties using these closure relations leads to unwanted nonphysical results at respectively low and high densities, and this for low values of the correlation length. These failures in the calculation of the structure will lead the calculation of the dynamics to undergo serious breakdowns, when EXP and PY are being used as a closure relation. HNC and MSA seemingly do not present any breakdowns at this level. The structural results, as interesting as they are, can only be fully interpreted with the associated dynamical results, which was the point of the second part of this work.

A full development of the MCT for fluids in randomness is presented, that allows the calculation of the collective and self ISF, the MSD, the non-Gaussian parameter, and the local exponent. These quantities have been computed and used to understand the dynamics and relaxation of the fluids in a speckle-like smooth disordered potential. First, phase diagrams have been created, which show in a general picture, transition lines separating the different phases the fluid can be in, as a result of steric interaction and/or perturbation by the potential. The shape of the phase diagrams is discussed and brings an overall understanding of the relaxation of the fluid. A particularly interesting feature consists in the reentrance of some of the transition lines. This nonmonotonic characteristic is an essential feature of this system and can be related to the change of regime of the correlation functions, as observed in the dedicated section. As expected, the dynamics calculated using the PY and EXP closure relations fail due to the aforementionned issues with the structural correlation functions. It has been found that HNC reaches a new branch of solutions at values of the correlation length of the order of the diameter of a particle. This new branch of solutions is non-physical, and leads the calculations to reach a dead end. However, since the experimental results focused on a correlation length of half a diameter, this issue does not undermine the fundamental comparison with reality inherent to every theoretical study. In order to be extensive, a quick overview of the phase diagrams calculated using MSA has been made, and compared with HNC. Next, the ISFs are calculated around the transition lines. This quantity allows for a study of the relaxation processes and a refinement of the scenarios developped by simply looking at the phase diagrams. Finally, the non-Gaussian parameter and the local exponent are studied and discussed as much as their complexity allows it. Throughout the chapter dedicated to the dynamics of the fluid, comparison with experiments has been made. Even though the differences between the theoretical results and the experimental counterpart can be dramatic (dimensionality, time scales, etc.), features such as the reentrance of the transition lines and the behavior of the long-time diffusion coefficient are very similar, and can be thought to be of some universality among systems of fluids in smooth disordered potential.

The end of this thesis is devoted to more down-to-earth considerations, as the numerical tricks and treatment of the structural and MCT equations are detailed. Around the end of the PhD, it seemed clear that the resources of pure theory had been exploited

extensively, and that the artifacts deeply built into the core of the MCT framework are a barrier to the full understanding of this complex system. Therefore, as a way of circumventing both the issues of theory and of experiments, a Monte-Carlo simulation tool has been developped. The preliminary results are presented at the very end and look promising for the future of the project. Many complex predictions made by the MCT are still waiting for a comparison, and hopefully, with enough time the precision and the timescales spanned by the Monte-Carlo calculations will allow for such a juxtaposition. Moreover, the simulations are not bound to their dimensionality. Therefore, simulations would allow for a comparison both with the theory and with the experiments, which would kill two birds with one stone.

As a concluding remark, we must say that the difficulty of the interpretation of the results could only be compared to the simplicity of the system from which they arise. It is probable that many more studies are to be undertaken before reaching a full understanding of all the phenomena at play both in the structure and the dynamics.

Bibliography

Alba-Simionesco C., Coasne B., Dosseh G., Dudziak G., Gubbins K.E., Radhakrishnan R. and Sliwinska-Bartkowiak M. (2006) Effects of confinement on freezing and melting, *J. Phys.: Condens. Matter* **18**, R15.

Alcoutlabi M. and McKenna G.B. (2005) Effects of confinement on material behaviour at the nanometre size scale, *J. Phys.: Condens. Matter* **17**, R461.

Andersen H.C., Chandler D. and Weeks J.D. (1972) Optimized cluster expansions for classical fluids. iii. applications to ionic solutions and simple liquids, *The Journal of Chemical Physics* **57**, 2626.

Ashkin A. (1997) Optical trapping and manipulation of neutral particles usinglasers, *Proceedings of the National Academy of Sciences* **94**, 4853.

Babič D., Schmitt C. and Bechinger C. (2005) Colloids as model systems for problems in statistical physics, *Chaos: An Interdisciplinary Journal of Nonlinear Science* **15**, 026114.

Bertschinger E. (2001) Multiscale Gaussian Random Fields for Cosmological Simulations, *The Astrophysical Journal Supplement Series* **137**, 1.

Bewerunge J. (2016) *Colloids in random potentials: Optical realization and characterization of rough laser light fields*, Ph.D. thesis, Heinrich-Heine-Universität Düsseldorf.

Bewerunge J. and Egelhaaf S.U. (2016) Experimental creation and characterization of random potential-energy landscapes exploiting speckle patterns, *Phys. Rev. A* **93**, 013806.

Bewerunge J., Ladadwa I., Platten F., Zunke C., Heuer A. and Egelhaaf S.U. (2016a) Time- and ensemble-averages in evolving systems: the case of brownian particles in random potentials, *Phys. Chem. Chem. Phys.* **18**, 18887.

Bewerunge J., Sengupta A., Capellmann R.F., Platten F., Sengupta S. and Egelhaaf S.U. (2016b) Colloids exposed to random potential energy landscapes: From particle

number density to particle-potential and particle-particle interactions, *J. Chem. Phys.* **145**, 044905.

Bouchaud J.P. and Georges A. (1990) Anomalous diffusion in disordered media: Statistical mechanisms, models and physical applications, *Phys. Rep.* **195**, 127.

Bowman R.W. and Padgett M.J. (2013) Optical trapping and binding, *Reports on Progress in Physics* **76**, 026401.

Chakraborty A.K., Bratko D. and Chandler D. (1994) Diffusion of ionic penetrants in charged disordered media, *J. Chem. Phys.* **100**, 1528.

Chudnovsky E.M. and Dickman R. (1998) Elastic lattice in a random potential, *Phys. Rev. B* **57**, 2724.

De Gennes P.G. (1975) Brownian motion of a classical particle through potential barriers. application to the helix-coil transitions of heteropolymers, *J. Stat. Phys.* **12**, 463.

De Masi A., Ferrari P.A., Goldstein S. and Wick W.D. (1989) An invariance principle for reversible Markov processes. applications to random motions in random environments, *J. Stat. Phys.* **55**, 787.

Dean D.S., Drummond I.T. and Horgan R.R. (2007) Effective transport properties for diffusion in random media, *J. Stat. Mech.: Theory Exp.* **2007**, P07013.

Dean D.S. and Touya C. (2008) A self-similar renormalization group applied to diffusion in non-Gaussian potentials, *J. Phys. A: Math. Theor.* **41**, 335002.

Deem M.W. and Chandler D. (1994) Classical diffusion in strong random media, *J. Stat. Phys.* **76**, 911.

Edwards S.F. and Anderson P.W. (1975) Theory of spin glasses, *J. Phys. F: Metal Phys.* **5**, 965.

Evers F., Hanes R., Zunke C., Capellmann R., Bewerunge J., Dalle-Ferrier C., Jenkins M., Ladadwa I., Heuer A., Castañeda-Priego R. and Egelhaaf S. (2013a) Colloids in light fields: Particle dynamics in random and periodic energy landscapes, *Eur. Phys. J. Special Topics* **222**, 2995.

Evers F., Zunke C., Hanes R., Bewerunge J., Ladadwa I., Heuer A. and Egelhaaf S. (2013b) Particle dynamics in two-dimensional random-energy landscapes: Experiments and simulations, *Phys. Rev. E* **88**, 022125.

Fallani L., Fort C. and Inguscio M. (2008) Bose-Einstein condensates in disordered potentials, *Adv. At. Mol. Opt. Phys.* **56**, 119.

Foffi G., Dawson K.A., Buldyrev S.V., Sciortino F., Zaccarelli E. and Tartaglia P. (2002) Evidence for an unusual dynamical-arrest scenario in short-ranged colloidal systems, *Phys. Rev. E* **65**, 050802.

Franosch T. (2014) Long-time limit of correlation functions, *J. Phys. A: Math. Theor.* **47**, 325004.

Franosch T., Fuchs M., Götze W., Mayr M.R. and Singh a.P. (1997a) Asymptotic laws and preasymptotic correction formulas for the relaxation near glass-transition singularities, *Physical Review E* **55**, 7153.

Franosch T., Fuchs M., Götze W., Mayr M.R. and Singh A.P. (1997b) Asymptotic laws and preasymptotic correction formulas for the relaxation near glass-transition singularities, *Phys. Rev. E* **55**, 7153.

Frey E. and Kroy K. (2005) Brownian motion: a paradigm of soft matter and biological physics, *Annalen der Physik* **14**, 20.

Fuchs M., Götze W., Hofacker I. and Latz A. (1991) Comments on the α-peak shapes for relaxation in supercooled liquids, *J. Phys.: Condens. Matter* **3**, 5047.

Fuchs M., Götze W. and Mayr M.R. (1998) Asymptotic laws for tagged-particle motion in glassy systems, *Phys. Rev. E* **58**, 3384.

Gelb L.D., Gubbins K.E., Radhakrishnan R. and Sliwinska-Bartkowiak M. (1999) Phase separation in confined systems, *Rep. Prog. Phys.* **62**, 1573.

Götze W. (1978) An elementary approach towards the Anderson transition, *Solid State Commun.* **27**, 1393.

Götze W. (1979) A theory for the conductivity of a fermion gas moving in a strong three-dimensional random potential, *J. Phys. C: Solid State Phys.* **12**, 1279.

Götze W. (1981) The mobility of a quantum particle in a three-dimensional random potential, *Philos. Mag. B* **43**, 219.

Götze W. (1991) *Liquids, freezing and glass transition, Les Houches 1989*, pp. 287–503 (North Holland, Amsterdam).

Götze W. (1999) Recent tests of the mode-coupling theory for glassy dynamics, *J. Phys.: Condens. Matter* **11**, A1.

Götze W. (2009) *Complex Dynamics of Glass-Forming Liquids – A Mode-Coupling Theory* (Oxford University, Oxford).

Götze W., Leutheusser E. and Yip S. (1981a) Correlation functions of the hard-sphere Lorentz model, *Phys. Rev. A* **24**, 1008.

Götze W., Leutheusser E. and Yip S. (1981b) Dynamical theory of diffusion and localization in a random, static field, *Phys. Rev. A* **23**, 2634.

Götze W., Prelovšek P. and Wölfle P. (1979) Localization of particles in a two-dimensional random potential, *Solid State Commun.* **30**, 369.

Götze W. and Sjögren L. (1992) Relaxation processes in supercooled liquids, *Rep. Prog. Phys.* **55**, 241.

Hanes R.D.L., Dalle-Ferrier C., Schmiedeberg M., Jenkins M.C. and Egelhaaf S.U. (2012) Colloids in one dimensional random energy landscapes, *Soft Matter* **8**, 2714.

Hanes R.D.L. and Egelhaaf S.U. (2012) Dynamics of individual colloidal particles in one-dimensional random potentials: a simulation study, *J. Phys.: Condens. Matter* **24**, 464116.

Hanes R.D.L., Schmiedeberg M. and Egelhaaf S.U. (2013) Brownian particles on rough substrates: Relation between intermediate subdiffusion and asymptotic long-time diffusion, *Phys. Rev. E* **88**, 062133.

Havlin S. and Ben-Avraham D. (1987) Diffusion in disordered media, *Advances in Physics* **36**, 695.

Haw M.D. (2002) Colloidal suspensions, brownian motion, molecular reality: a short history, *Journal of Physics: Condensed Matter* **14**, 7769.

Höfling F. and Franosch T. (2013) Anomalous transport in the crowded world of biological cells, *Rep. Prog. Phys.* **76**, 046602.

Hänggi P. and Marchesoni F. (2005) Introduction: 100 years of brownian motion, *Chaos: An Interdisciplinary Journal of Nonlinear Science* **15**, 026101.

Isichenko M.B. (1992) Percolation, statistical topography, and transport in random media, *Rev. Mod. Phys.* **64**, 961.

Kim K., Miyazaki K. and Saito S. (2009) Slow dynamics in random media: Crossover from glass to localization transition, *EPL* **88**, 36002.

Kim K., Miyazaki K. and Saito S. (2010) Molecular dynamics studies of slow dynamics in random media: Type A-B and reentrant transitions, *Eur. Phys. J. Special Topics* **189**, 135.

Kim K., Miyazaki K. and Saito S. (2011) Slow dynamics, dynamic heterogeneities, and fragility of supercooled liquids confined in random media, *J. Phys.: Condens. Matter* **23**, 234123.

Kraichnan R.H. (1976) Diffusion of passive-scalar and magnetic fields by helical turbulence, *J. Fluid Mech.* **77**, 753.

Krakoviack V. (2005a) Liquid-glass transition of a fluid confined in a disordered porous matrix: A mode-coupling theory, *Phys. Rev. Lett.* **94**, 065703.

Krakoviack V. (2005b) Liquid-glass transition of confined fluids: insights from a mode-coupling theory, *J. Phys.: Condens. Matter* **17**, S3565.

Krakoviack V. (2007) Mode-coupling theory for the slow collective dynamics of fluids adsorbed in disordered porous media, *Phys. Rev. E* **75**, 031503.

Krakoviack V. (2009) Tagged-particle dynamics in a fluid adsorbed in a disordered porous solid: Interplay between the diffusion-localization and liquid-glass transitions, *Phys. Rev. E* **79**, 061501.

Krakoviack V. (2011) Mode-coupling theory predictions for the dynamical transitions of partly pinned fluid systems, *Phys. Rev. E* **84**, 050501(R).

Kurzidim J., Coslovich D. and Kahl G. (2009) Single-particle and collective slow dynamics of colloids in porous confinement, *Phys. Rev. Lett.* **103**, 138303.

Kurzidim J., Coslovich D. and Kahl G. (2010) Impact of random obstacles on the dynamics of a dense colloidal fluid, *Phys. Rev. E* **82**, 041505.

Kurzidim J., Coslovich D. and Kahl G. (2011) Dynamic arrest of colloids in porous environments: disentangling crowding and confinement, *J. Phys.: Condens. Matter* **23**, 234122.

Lang S., Boţan V., Oettel M., Hajnal D., Franosch T. and Schilling R. (2010) Glass transition in confined geometry, *Phys. Rev. Lett.* **105**, 125701.

Lebowitz J.L. and Percus J.K. (1966) Mean spherical model for lattice gases with extended hard cores and continuum fluids, *Phys. Rev.* **144**, 251.

Lemons D.S. and Gythiel A. (1997) Paul langevin's 1908 paper "on the theory of brownian motion" ["sur la théorie du mouvement brownien," c. r. acad. sci. (paris) 146, 530–533 (1908)], *American Journal of Physics* **65**, 1079.

Leutheusser E. (1983a) Diffusion blocking in a frozen rigid-sphere fluid, *Phys. Rev. A* **28**, 2510.

Leutheusser E. (1983b) Self-consistent kinetic theory for the Lorentz gas, *Phys. Rev. A* **28**, 1762.

Lifshits I.M., Gredeskul S.A. and Pastur L.A. (1988) *Introduction to the theory of disordered systems* (Wiley, New York).

Ma X., Chen W., Wang Z., Peng Y., Han Y. and Tong P. (2013) Test of the universal scaling law of diffusion in colloidal monolayers, *Phys. Rev. Lett.* **110**, 078302.

Mandal S., Lang S., Gross M., Oettel M., Raabe D., Franosch T. and Varnik F. (2014) Multiple reentrant glass transitions in confined hard-sphere glasses, *Nat. Commun.* **5**, 4435.

Menon G.I. and Dasgupta C. (1994) Effects of pinning disorder on the correlations and freezing of the flux liquid in layered superconductors, *Phys. Rev. Lett.* **73**, 1023.

Meroni A., Levesque D. and Weis J.J. (1996) Correlation functions of hard sphere fluids adsorbed in porous media, *J. Chem. Phys.* **105**, 1101.

Mezard M., Parisi G. and Virasoro M. (1987) *Spin Glass Theory and Beyond*, Lecture Notes in Physics Series (World Scientific).

Molloy J.E. and Padgett M.J. (2002) Lights, action: Optical tweezers, *Contemporary Physics* **43**, 241.

Paoluzzi M., Di Leonardo R., and Angelani L. (2014) Run-and-tumble particles in speckle fields, *J. Phys.: Condens. Matter* **26**, 375101.

Percus J.K. and Yevick G.J. (1958) Analysis of Classical Statistical Mechanics by Means of Collective Coordinates, *Physical Review* **110**, 1.

Pezzé L., de Saint-Vincent M.R., Bourdel T., Brantut J.P., Allard B., Plisson T., Aspect A., Bouyer P. and Sanchez-Palencia L. (2011) Regimes of classical transport of cold gases in a two-dimensional anisotropic disorder, *New J. Phys.* **13**, 095015.

Pham K.N., Egelhaaf S.U., Pusey P.N. and Poon W.C.K. (2004) Glasses in hard spheres with short-range attraction, *Phys. Rev. E* **69**, 011503.

Pinçe E., Velu S.K.P., Callegari A., Elahi P., Gigan S., Volpe G. and Volpe G. (2016) Disorder-mediated crowd control in an active matter system, *Nat. Commun.* **7**, 10907.

Redding B., Schwab M.J. and Pan Y. (2015) Raman spectroscopy of optically trapped single biological micro-particles, *Sensors* **15**, 19021.

Salmon J. (1996) Generation of Correlated and Constrained Gaussian Stochastic Processes for N-Body Simulations, *Astrophysical Journal* **460**, 59.

Schnyder S.K., Höfling F., Franosch T. and Voigtmann T. (2011) Long-wavelength anomalies in the asymptotic behavior of mode-coupling theory, *J. Phys.: Condens. Matter* **23**, 234121.

Schnyder S.K., Skinner T.O.E., Thorneywork A.L., Aarts D.G.A.L., Horbach J. and Dullens R.P.A. (2017) Dynamic heterogeneities and non-Gaussian behavior in two-dimensional randomly con
fined colloidal fluids, *Phys. Rev. E* **95**, 032602, arXiv:1608.04853v1.

Schnyder S.K., Spanner M., Höfling F., Franosch T. and Horbach J. (2015) Rounding of the localization transition in model porous media, *Soft Matter* **11**, 701.

Sciortino F., Tartaglia P. and Zaccarelli E. (2003) Evidence of a higher-order singularity in dense short-ranged attractive colloids, *Phys. Rev. Lett.* **91**, 268301.

Shvedov V., Rode A., Izdebskaya Y., Leykam D., Desyatnikov A.S., Krolikowski W. and Kivshar Y.S. (2010) Laser speckle field as a multiple particle trap, *J. Opt.* **12**, 124003.

Skinner T.O.E., Schnyder S.K., Aarts D.G.A.L., Horbach J. and Dullens R.P.A. (2013) Localization dynamics of fluids in random confinement, *Phys. Rev. Lett.* **12**, 128301.

Spanner M., Schnyder S.K., Höfling F., Voigtmann T. and Franosch T. (2013) Dynamic arrest in model porous media—intermediate scattering functions, *Soft Matter* **9**, 1604.

Szamel G. (2004) Gaussian density fluctuations, mode coupling theory and all that, *Europhys. Lett.* **65**, 498.

Thalmann F., Dasgupta C. and Feinberg D. (2000) Phase diagram of a classical fluid in a quenched random potential, *Europhys. Lett.* **50**, 54.

Touya C. and Dean D.S. (2007) Dynamical transition for a particle in a squared Gaussian potential, *J. Phys. A: Math. Theor.* **40**, 919.

Volpe G., Volpe G. and Gigan S. (2014) Brownian motion in a speckle light field: Tunable anomalous diffusion and selective optical manipulation, *Sci. Rep.* **4**, 3936.

Yang J. and Zhao H. (2010) Anomalous diffusion among two-dimensional scatterers, *J. Stat. Mech.: Theory Exp.* **2010**, L12001.

Zaccarelli E., Foffi G., Dawson K.A., Buldyrev S.V., Sciortino F. and Tartaglia P. (2002) Confirmation of anomalous dynamical arrest in attractive colloids: A molecular dynamics study, *Phys. Rev. E* **66**, 041402.

Zallen R. and Scher H. (1971) Percolation on a continuum and the localization-delocalization transition in amorphous semiconductors, *Phys. Rev. B* **4**, 4471.

Ziman J.M. (1968) The localization of electrons in ordered and disordered systems I. percolation of classical particles, *J. Phys. C: Solid State Phys.* **1**, 1532.

Zwanzig R. (1988) Diffusion in a rough potential, *Proc. Natl. Acad. Sci. U.S.A.* **85**, 2029.

Recent experimental studies of the dynamics oàf colloids beamed by a random light pattern (speckle) whowed the existence of subdiffusion, trapping, or mixture separation phenomena, under the action of that disordered environment. To this end, a verison of the Mode Coupling Theory (MCT), initially developed for fluids in confinement in solid porous matrices has been applied to the case of a fluid plunged in a random Gaussian potential with a Gaussian correlation function. The aim of this PhD work is to further improve the understanding of these phenoma by the addition of a theoretical study. The numerical resultion of the asymptotic equations of this theory leads to the construction of phase diagrams, which reproduce for example the non trivial reentrent behaviour of the diffusivity, observed in related experiments, for which a physical interpretation is proposed. Furthermore, results suggest a strong dependence of the dynamics on the disorder correlation length. A detailed study of the relaxation of the fluid has been made, in order to bring an understanding of the dynamics at all timescales. Simultaneously, it has been showed that a number of common approximations used in the calculation of the structural properties of fluids lead in the present case to non-physical results. Finally, a Monte-Carlo simulation program has been developed, and the first results are compared to theory and experiments.

De récentes études expérimentales de la dynamique de colloïdes illuminés par une figure d'interférence optique aléatoire (tavelures ou speckle) ont montré l'existence de phénomènes de sous-diffusion, de piégeage, ou de ségrégation dans le cas de mélanges, sous l'effet de cet environnement désordonné. L'objet de ce travail de doctorat est d'approfondir la compréhension de ces phénomènes par une étude théorique. Dans ce but, une version de la théorie de couplage de modes (MCT), initialement développée pour les fluides confinés dans des solides poreux désordonnés, a été appliquée au cas d'un fluide plongé dans un potentiel aléatoire gaussien de covariance gaussienne. La résolution numérique des équations asymptotiques de cette théorie a permis la construction de diagrammes d'état, lesquels reproduisent, par exemple, le comportement réentrant non trivial de la diffusivité observé dans les expériences, dont une interprétation physique simple est proposée. Les résultats suggèrent en outre une forte dépendance de la dynamique du système par rapport à la longueur de corrélation du désordre. Une étude détaillée de la relaxation du fluide a été effectuée, dans le but d'apporter une compréhension de la dynamique à toutes les échelles de temps. En parallèle, il a été montré que de nombreuses approximations classiques utilisées dans le calcul des propriétés structurales des fluides conduisent à des résultats non physiques dans le cas présent. Finalement, un programme de simulation Monte Carlo a été développé, et les premiers résultats sont comparés à la théorie et aux expériences.